2021

Investigation of Nitrate Transfer in Karst Basins During Storm Events Using Submersible Underwater Nutrient Analyzers

John Pike
University of Kentucky, jpike456@gmail.com
Digital Object Identifier: https://doi.org/10.13023/etd.2021.249

Recommended Citation

Pike, John, "Investigation of Nitrate Transfer in Karst Basins During Storm Events Using Submersible Underwater Nutrient Analyzers" (2021). *Theses and Dissertations--Civil Engineering*. 109.
https://uknowledge.uky.edu/ce_etds/109

STUDENT AGREEMENT:

I represent that my thesis or dissertation and abstract are my original work. Proper attribution has been given to all outside sources. I understand that I am solely responsible for obtaining any needed copyright permissions. I have obtained needed written permission statement(s) from the owner(s) of each third-party copyrighted matter to be included in my work, allowing electronic distribution (if such use is not permitted by the fair use doctrine) which will be submitted to UKnowledge as Additional File.

I hereby grant to The University of Kentucky and its agents the irrevocable, non-exclusive, and royalty-free license to archive and make accessible my work in whole or in part in all forms of media, now or hereafter known. I agree that the document mentioned above may be made available immediately for worldwide access unless an embargo applies.

I retain all other ownership rights to the copyright of my work. I also retain the right to use in future works (such as articles or books) all or part of my work. I understand that I am free to register the copyright to my work.

REVIEW, APPROVAL AND ACCEPTANCE

The document mentioned above has been reviewed and accepted by the student’s advisor, on behalf of the advisory committee, and by the Director of Graduate Studies (DGS), on behalf of the program; we verify that this is the final, approved version of the student’s thesis including all changes required by the advisory committee. The undersigned agree to abide by the statements above.

John Pike, Student

Dr. James Fox, Major Professor

Dr. Timothy Taylor, Director of Graduate Studies

INVESTIGATION OF NITRATE TRANSFER IN KARST BASINS DURING STORM EVENTS USING SUBMERSIBLE UNDERWATER NUTRIENT ANALYZERS

THESIS

A thesis submitted for the partial fulfillment of the
requirements for the degree of Master of Science
in Civil Engineering in the College of Engineering
at the University of Kentucky

By

John Robert Pike

Lexington, Kentucky

Director: Dr. James Fox, Professor of Civil Engineering

Lexington, Kentucky

2021

ABSTRACT OF THESIS

INVESTIGATION OF NITRATE TRANSFER IN KARST BASINS DURING STORM EVENTS USING SUBMERSIBLE UNDERWATER NUTRIENT ANALYZERS

Knowledge of nitrate sources and pathways in karst basins remains incomplete and hinders management of nutrients that cause algae blooms and degrade municipal water supply. However, the increased availability of optical, ultraviolet nitrate sensors allows advancement of nitrate source and transfer for water managers. A concept model is hypothesized for nitrate transfer during hydrologic events and baseflow that considers the multiple porosity of karst. To test the concept model, 15-minute nitrate sensor data is collected with submersible underwater nutrient analyzers over a multi-year period from two locations in a karst basin in the inner bluegrass region of central Kentucky, USA.

Data results carried through quality assurance and quality control methods suggests fluctuations in nitrate and provides evidence of karst pathways with varying porosity. The inner bluegrass nitrate sensor results are compared with data from other karst basins in the United States, including the carbonate karst and their aquifers in Kentucky, Arkansas, Virginia and Maryland. Meta-analysis results from hydrographs, chemographs and hysteresis show evidence of nitrate transfers in karst including: a piston effect at the onset of an event as water stored in fractures and conduits is displaced by new water; a quick response during or just after storm event peaks that quickly dilutes nitrate levels in water; a concentrating effect after an event as high nitrate levels stored in soil water dominate transport; and a nitrate recession curve as nitrate stored in rock matrix become a larger contributor to nitrate flux.

Mass balance un-mixing simulation was carried out to quantify nitrate sources for the inner bluegrass basin. The amount of water and nitrate load associated with the nitrate sources was quantified for four seasons and revealed the importance of the intermediate flow/fracture network pathway in transporting the majority of nitrate load. The piston flush occurring at the beginning of storm events was also noteworthy generating greater than 10% of the nitrate load.

A reservoir model was formulated to represent the nitrate transfer processes for prediction. The reservoir model showed more insight including the impact of seasonality and sinkhole concentration on the distribution of water while at the same time showed the efficacy of the approach. New information from the reservoir modelling included the volume of water and nitrate stored in the karst aquifer, and these estimates will be useful for concerns of algal bloom proliferation at different times of the year.

KEYWORDS: nutrients, nitrate, nitrate loading, watershed, watershed processes, sensors

John Robert Pike

July 12, 2021

INVESTIGATION OF NITRATE TRANSFER IN KARST BASINS DURING STORM EVENTS USING SUBMERSIBLE UNDERWATER NUTRIENT ANALYZERS

By

John Robert Pike

Dr. James Fox

Director of Thesis

Dr. Timothy Taylor

Director of Graduate Studies

July 12, 2021

ACKNOWLEDGEMENTS

This thesis research was a collaborative effort and was supported in part by a great number of partners. I give the strongest thanks to my Thesis Chair, Dr. James Fox, for his mentorship, direction, and collaboration through my learning process. I would also like to thank the members of my Thesis Committee: Dr. Shakira R. Hobbs and Dr. Lindell E. Ormsbee for reviewing my work. I would like to think all my fellow researchers and colleagues who directly contributed this research: Tyler Mahoney, Leonie Bettel, Noah Smith, Thomas Dunlop, Stephen Day, Brenden Riddle, Morgan Gerlitz, and Ashlee Edmonson. I would like to thank research collaborator Jason Backus his work in the laboratory supporting the research project.

I would like to thank the University of Kentucky and the Department of Civil Engineering for the education and resources I have received in my years as an undergraduate and graduate student. I would like to recognize the Lauderdale Fellowship and thank the fellowships benefactors, Robert A. and Maywin S. Lauderdale for proving the funding which made this research possible.

TABLE OF CONTENTS

LIST OF FIGURES

Chapter 1 Introduction

1.1 Nitrate pollution of our water supply and our motivation to control nitrate:

The research in this thesis helps us to better understand the basic processes by which nitrogen concentrations fluctuate and travel through the karst ecosystem. As a society it is our responsibility and our need to protect the health of our natural water resources. Modern plant and animal farming, lawn keeping practices, and sewage runoff from municipal wastewater systems have increased the amount of nitrogen inputs into the environment (Clean Water Action, 2019). Urbanization has created an abundance of impervious surfaces, reducing the number of natural buffers in our system which would be able to absorb and disperse this nitrogen. This increase in nitrogen poses major risks to water supply. Algae colonies in rivers and lakes can assimilate nitrogen and have the potential to bloom and grow to large scales such as the Ohio River's 700-mile-long hazardous algal bloom in 2015 and reemergence in 2019. Risk is further increased in slow-moving or stagnant water such as the area surrounding the 14 lock and dams on the Kentucky River (Denchak, 2020). Toxic algae can grow and release toxins which can directly pose health risks to humans and animals drinking from the water.

The EPA considers harmful algal blooms (HABs) such as red tides, blue-green algae, and cyanobacteria as a major environmental problem in all 50 states (EPA, 2019). Toxins produced by HABs can contaminate freshwater with cyanotoxins which affect the nervous system, hepatotoxins which affect the liver, dermatoxins which affect the skin, and others which affect stomach and intestines (CDC, 2017). Non-Toxic algae blooms will consume large amounts of oxygen in the water as they die and decompose, this creates a dead zone in the water where no aquatic life can survive. The Gulf of Mexico has grown a 15,125 square kilometer dead zone as of 2013 due to nutrient pollution from the Mississippi River Basin that Kentucky contributes to (EPA 2019).

Nutrient pollution poses a risk to the health and safety of Kentucky water supplies, and this thesis focuses on central Kentucky USA. Sources of pollutants in Kentucky include pasture, agriculture, urban runoff and groundwater. The South Elkhorn Watershed, studied herein, has pathways in and around Fayette, Woodford, and Scott Counties, centering around Lexington, Kentucky. Pollution in this watershed is directly impacted by the mentioned non-point sources and the Town Branch Wastewater Treatment Plant; and in turn HABs have the potential to occur in the slow-moving waters of pool three of the Kentucky River. At this location, a Kentucky American Water Intake exists, which provides drinking water to Lexington and surrounding communities. Water is drained into Town Branch, South Elkhorn, and then Elkhorn Creek through overland, point source, and groundwater pathways. Overland runoff can be impacted by urban nutrient pollution in lawn fertilizers and pet waste, by agricultural and pasture pollution from fertilizers and manure from free roam cattle, and by point source pollutants from sewage services, such as the Town Branch Treatment Plant. Groundwater quality can be impacted by agricultural practices such as nitrate leaching. Water at the watershed outlet feeds into transmission lines which deliver water to meet urban and industrial water demands. The cyclic nature of the system leaves uplands and stream networks vulnerable to downstream water quality outbreaks such as HABs.

The motivation of this research is to control nitrate in our waterways. The more we understand about our systems, the better we can pose regulations and practices to mitigate these issues. We can directly share what concentrations are in our systems and a maximum limit for what concentrations need to be in the system for it to remain healthy. This research may help in the practicality of enforcement of these limits. This research helps to illuminate how nitrogen travels from its source to the water system, and then how the concentrations fluctuate as it travels downstream. We are learning that these concentrations undergo daily, monthly, seasonal, and yearly patterns which must be considered in the practicality and design of our regulations.

Our Kentucky system is classified as a karst basin and shows analogy to karst systems around the world. For this reason, this thesis provides comparison of data results with published karst datasets for other regions so that conclusions taken by this work can be referred upon to potentially help other communities.

1.2 Description of karst and a need for nitrate research:

Karst surface and groundwater basins refer to terrain underlain by limestone, or analogous bedrock, with high potential for developing karstic pathways (White, 2002). Atmospheric rainwater collects carbon dioxide (CO_2). When this water contacts limestone bedrock, the carbon dioxide will dissolve the bedrock material. Over long periods of time, this process will develop a karst landscape with networks of open fractures, karst conduits, and caves below the surface. Husic et al discusses the hydrology of a karst watershed in his 2019 paper. The hydrology of a karst system begins with swallets, small holes on or just below the land surface. Swallets feed into vertical fractures in the bedrock which channel water into a larger horizontal conduit. The conduit feeds into a stream or a spring. In the absence of a swallet, water will percolate down through the soil to the epikarst region. The epikarst region is the outer layer of karst bedrock and has higher permeability due to increased exposure to weathering. Below the epikarst is a limestone rock matrix with crossing horizontal and vertical pores. Pore size and permeability in matrix decrease with depth. Water in the rock matrix will continuously transfer to and from the fractures and conduit, creating a mixing effect.

Review of the water resources literature suggests knowledge of nitrate sources and pathways through karst basins is lacking, especially relative to watersheds with more traditional, slowflow groundwater transfer. A number of recent studies by Husic and others in the inner bluegrass region have aimed to advance research methods and results from karst basins including: an understanding of nitrate removal from phreatic caves in karst (Husic et al., 2020); sets of nitrate sources potentially contributing to karst groundwater (Husic et al., 2021); understanding of karst hydrographs and chemographs including potential quick, intermediate, and slowflow pathways contribution to karst water and nitrate transfer (Husic et al., 2019). This previous research has been important to understand nitrate transfer in karst, but there is currently a lack of a paradigm for nitrate sources and pathways before, during and after storm events as well as during low flows. Such a proposed concept for karst might be comparable to the two-component surface flow and baseflow of more traditional water theory (i.e., non-karst basins). The lack of knowledge calls for a research need for high time resolution data during storm and non-storm conditions in karst basins. A response to this need comes in the form of optical, ultraviolet nitrate sensing.

1.3 Optical, ultraviolet nitrate sensors:

In this research, nitrate data was collected with optical, ultraviolet nitrate sensors known as submersible underwater nutrient analyzers, or SUNA's (Seabird SUNA V2 nitrate sensors). Pellerin at el. comments in his 2016 study, covering the emergence of these high frequency sensors, that high frequency nitrate sensors have a unique ability to be used to map spatial variability in rivers. The SUNA is a real-time nutrient monitoring device that can be placed in a river and collect nitrate data every 15 minutes. The SUNA V2 utilizes nitrate measurement technology by considering the absorption of nitrate in the ultraviolet light spectrum (Figure 1.1). The concentration of nitrogen in a water sample is proportional to the measured absorption of ultraviolet light, which is measured by a photometer in the SUNA V2. This method of assessment offers high resolution, accuracy, and precise chemical-free fast response time. The SUNA V2 used in this study is outfitted with the Hydro-Wiper external fowling system which regularly cleans the UV sampling window to ensure high quality data collection.

Nitrate data is selected as the focus of nutrient study in central Kentucky. Nitrate is most likely the largest type of nitrogen transported from central Kentucky basins (i.e., nitrate concentration is greater than dissolved organic nitrogen or ammonium). Kentucky has an overabundance of phosphorus due to our soil and geology, so nitrogen can potentially become the limiting nutrient for algae growth, if nitrogen levels are reduced.

This nitrate data, analyses and modelling in this thesis is further supported by the following general water quality data provided by the YSI EXO 3 sensor: conductivity, dissolved oxygen, turbidity, pH, and temperature, also collected every 15 minutes. These additional parameters are selected as a form of backup to the nitrogen data. Many of these parameters respond to storm events with similar trends. These other general water quality parameters can also help us have a stronger idea of overall stream health as well as provide further quality assurance and quality control of the nitrate and flowrate data used as the basis of this work.

1.4 Analyses and modelling using nitrate sensor data:

Collecting 15 minute nitrate measurements from karst basins opens up a set of analyses and modelling methods that can be carried out and applied to investigate and predict nitrate transfer. This thesis utilizes hydrograph, chemograph and hysteresis analyses; mass balance un-mixing modelling for hydrograph and chemograph separation; and watershed modelling (Figure 1.2)

The hydrograph is a time-series graph which shows the change in flow rate of water (cfs or cms) over time. This thesis exhibits hydrographs for the South Elkhorn and Ramsey locations, upstream and downstream of South Elkhorn creek. Our flow data for the South Elkhorn site is gathered from the USGS 03289000 South Elkhorn Creek at Fort Spring, KY station. Ramsey flow data is found based off of the USGS readings and a weighted drainage area method, or through a Manning's equation based method. Hydrographs allow us to quickly identify the timing and magnitude of storm events.

The chemograph is a time-series graph which shows the change in nitrate concentration (mg/L as N) over time. This thesis exhibits chemographs for the South Elkhorn and Ramsey locations, upstream and downstream of South Elkhorn creek. Our nitrogen data is measured by the SUNA V2 nitrate sensor. Chemographs allow us to visualize daily, monthly, seasonal, and yearly trends in nitrate concentrations. Plotting a chemograph and a hydrograph on the same chart allows us to understand storm event dynamics. We can identify the piston effect, where nitrogen levels remain constant at the onset of an event. This is followed by the dilution effect where low-concentration rainwater dilutes nitrate concentrations in the stream.

The hysteresis loop plots flow rate on the x – axis directly against nitrogen concentration on the y – axis. Hysteresis loops are made to show direct changes between each variable during storm events. Time can be visualized on a hysteresis loop by drawing arrows or color-coding data to mark the first and second halves of the event. The hysteresis loop further enforces the piston and dilution effects. Nitrogen will remain constant, producing a flat line while flow increases as the loop begins. Following this, nitrogen will bottom out at a minimum value before slowly increasing as flow rate returns to pre-storm values.

Graphical hydrograph separation is used by Miller et al 2016. He relies on streamflow data alone to separate runoff and baseflow components. This method can be combined with mass balance un-mixing modelling to utilizes our understanding of the changing influence of flow paths throughout an event. By assuming only two flow paths are active at a time, we can calculate the magnitude of influence of each flow path at each time step. This is done by comparing the flow path source nitrogen concentration to the current concentration. Graphing these magnitudes allow us to visualize how each of the following flow paths: piston flow, quick flow, intermediate flow, and slow flow rise and fall throughout an event. We can also compare events from different season to see how changes in environmental conditions affect the behavior of flow paths.

Watershed modeling on a long-term scale is studied in Husic et al 2019. Husic develops a reservoir model which uses rainfall data as an input and evapotranspiration and flow through each reservoir and into the stream as an output. Nitrate concentrations are modeled based on calibration parameters for each pathway and season and compared against nitrate data to help verify the pathways controlling nitrate transport. In this thesis, these methods will be adapted to create a reservoir model for the South Elkhorn Watershed on the single event scale. This will all me to better examine flow pathways and nitrate transport as they occur during a single rainfall event. Nitrate data will be used as a calibration parameter which controls the nitrate concentrations in each pathway.

1.5 Objectives:

The overall objective is to combine nitrate data with hysteresis analyses, mass balance modelling to help understand the nature of water and nitrate arriving at the stream, and then watershed modelling to understand the changes this water undergoes as it flows. To do so, water quality and nutrient data at upstream and downstream locations in the South Elkhorn Watershed is collected as well as acquire data published in the scientific literature.

My specific objectives are to:

1. Propose a concept model for nitrate transfer during hydrologic events and baseflow that considers the multiple porosity of karst.
2. Collect, carry out quality assurance and quality control, and present 15-minute nitrate sensor data over a four-year period from a karst basin in the inner bluegrass region of central Kentucky, USA.
3. Test the concept model using a meta-analysis with data from Kentucky as well as other nitrate sensor datasets from karst regions in the United States.
4. Carry out a mass balance un-mixing simulation was carried out to quantify sources for the Kentucky basin.
5. Formulate and carry out simulation of a reservoir model was formulated to represent the nitrate transfer processes for prediction.

It is the intent of this thesis that we can study these mentioned processes with concern for human impact to better understand what we can do to preserve the quality of our local water supply.

Figure 1.1 Diagram of The SUNA V2 Absorption Measurement Principle From H20 Engineering

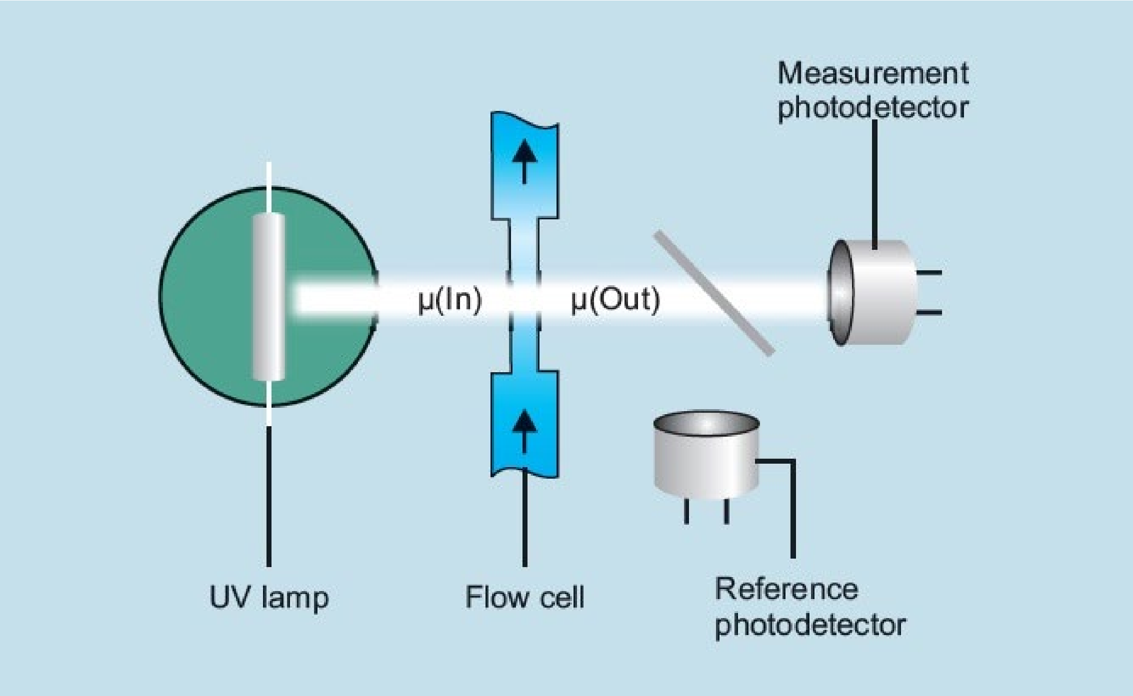

Figure 1.2 Sample of Hydrograph, Chemograph, Separation of Hydrograph Flow Components

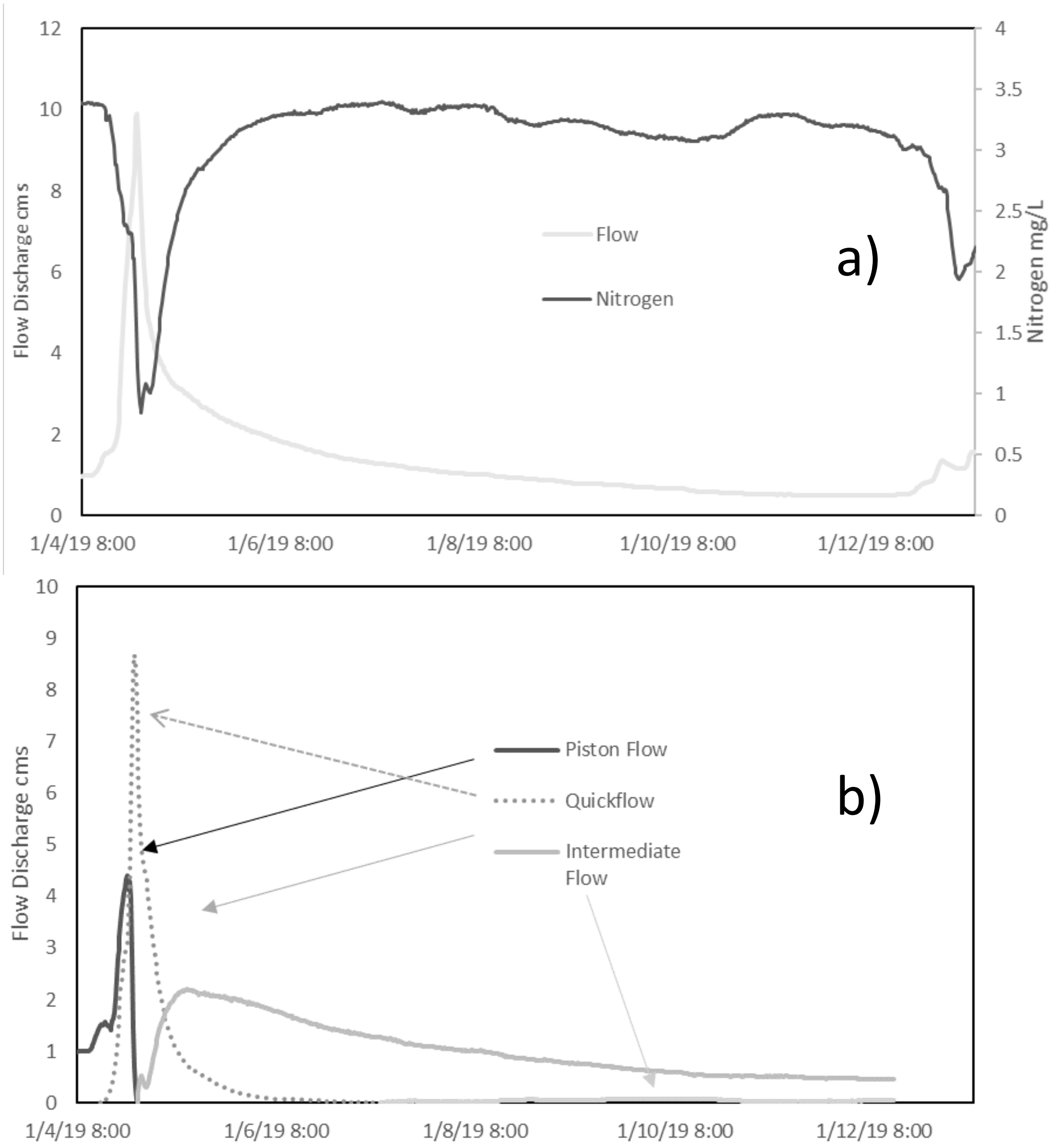

Chapter 2 Theoretical background and concept model

2.1 Nitrate transfer processes in karst:

Nitrate transfer in karst basins relies on nitrate sources across the basin that can be transported through hydrologic pathways at the surface or in groundwater. Sources include point and non-point sources such as: urban nutrient pollution in lawn fertilizers and pet waste; agricultural and pasture pollution from fertilizers and manure from free roam cattle; and by point source pollutants from sewage services.

There are many hydrologic pathways in karst. The pathways are presented here in Figure 2.1 after Figure 1 from Al Aamery et al. (2021). The hydrology of karst systems begins with swallets, small holes on or just below the land surface. Swallets feed into vertical fractures in the bedrock which channel water into a larger horizontal conduit. The conduit feeds into a stream or a spring. In the absence of a swallet, water will percolate down through the soil to the epikarst region. The epikarst region is the outer layer of karst bedrock and has higher permeability due to increased exposure to weathering. Below the epikarst is a limestone rock matrix with crossing horizontal and vertical pores. Pore size and permeability in matrix decrease with depth. Water in the rock matrix will continuously transfer to and from the fractures and conduit, creating a mixing effect.

2.2 Concept model of nitrate in karst:

The concept model for nitrate in karst aims to describe the time distribution of nitrate as measured at the outlet of a karst coupled groundwater-surfacewater basin, such as measured at the surface water outlet of a basin that has substantial karst influence or at a karst spring. To create the concept model, we assume several processes consistent with the figure by Al Aamery et al. (2021) and nitrate leaching discussion by Husic et al. (2020). We assume the potential for surface flows and runoff that carries nitrate, the presence of soil and the potential for nitrate leaching through soils to the karst subsurface, multiple levels of porosity in the karst subsurface including fractures and conduits as well as rock matrix. For sake of illustration, we assume nitrate concentration in soil water and groundwater is greater than nitrate concentration in runoff, although we discuss in the discussion section how shifting of the nitrate levels would impact results.

An earlier cartoon of the nitrate concept model for karst was presented in Husic et al. (in review at *Water Resources Research*). Our concept presented here agrees with often cited interpretations for dual-transfer (i.e., quick- and slow-flow) or triunal-transfer (i.e., quick-, intermediate-, and slow-flow) in karst studies (e.g., Pinault et al., 2001; Worthington, 2007; Long, 2009). Our concepts also agree with the often cited pressure response of karst basins, and the condition of a pressure response for karst groundwater and the emergence of surface water such as identified with electrical conductivity measurements (e.g., Fournier et al., 2006).

<u>Baseflow:</u> The time distribution, or chemograph, of nitrate as measured at the outlet of a karst coupled groundwater-surfacewater basin is shown together with the hydrograph in Figure 2.2. Prior to the storm event, such as at time zero in Figure 2.2, water and nitrate leaving a karst basin is dominated by subsurface drainage pathways, and this portion of the hydrograph and chemograph are traditionally termed baseflow. In karst basins, this baseflow nitrate is likely associated with more than one porosity. We define intermediate flow to be water and nitrate draining from the soil to fractures and conduits and then to the basin outlet. We define slow flow to be water draining from the saturated rock matrix and microfractures.

Piston effect: When a storm event occurs, rainfall can turn to runoff and transport water and nitrate to sinkholes or depressions in karst terrain. Runoff can travel quickly through sinkhole openings, fractures and conduits and is sometimes referred to as underground runoff. In some cases, the underground runoff can add a pressure response to karst systems because the aquifer and its fracture-conduit network is phreatic. This instance causes the piston effect where water and nitrate distal from the karst springhead can create an immediate response and push pre-event water and nitrate to the karst spring. This piston effect can cause the more distal water and nitrate to reach the karst basin outlet before more proximal runoff. This idea is shown in Figure 2.2 because the hydrograph at the basin outlet increases but only intermediate and slowflow arrive at the basin outlet, and therefore the nitrate level is constant.

Quickflow dominance: The next change in the hydrograph and nitrate chemograph behavior occurs when quick flow from surface runoff or underground runoff entering via swallets and sinkholes reaches the basin outlet or karst spring. The result is abrupt NO_3 dilution leading to a NO_3 minimum as quick-flow dominates the water source at the karst spring, which is an artifact of our assumption that nitrate concentration in soil water and groundwater is greater than nitrate concentration in runoff. NO_3 concentration will occur if the runoff NO_3 level is greater than soil and groundwater. The NO_3 minimum and quick-flow dominance is shown to occur in Figure 2.2 just after the peak discharge, although this occur at the peak discharge or before it, depending on the specific distribution of pathways in the basin.

Intermediate flow breakthrough: The next change of the karst hydrograph and chemograph behavior occurs as intermediate flow from soil water draining via the epikarst, fractures and conduit reaches the spring. Soil water percolation is responsible for nitrate leaching and has been shown to concentrate nitrate in numerous studies (see review by Husic et al., 2019, WRR paper). This intermediate flow has fast transit relative to traditional groundwater flow, and little time is available for nitrate to undergo denitrification. For this reason, the intermediate flow NO_3 concentration resembles that of the soil water origin. The NO_3 maximum coincides with the emergence of soil water at the basin outlet or spring because nitrate leaching from soils often represents the highest concentrated nitrate in water for agriculturally impacted basins (Di and Cameron, 2002).

Nitrate recession: The next change in the hydrograph and nitrate chemograph occur as baseflow is re-established. During this period, the hydrograph decreases or reaches a constant while NO_3 shows a pronounced recession. The NO_3 recession slope is much greater than that which would represent denitrification (i.e., review of the literature suggests a first order rate constant for denitrification in karst equal to 0.001 to 0.015 d^{-1}, Husic et al., 2019). Rather, the NO_3 recession reflects the changing contributions over time of intermediate flow, originating from the soil percolation, and slowflow, originating as previously stored groundwater. This reflects the multiple-porosity associated with karst 'baseflow'. As the proportion of slowflow increases, and intermediate flow decreases, the NO_3 level drops. The NO_3 recession ceases when a new storm event causes another piston effect.

We define several variables to describe the storm event and low flow scenarios described in the concept model for hydrograph and nitrate chemograph behavior in karst. T_{E0} is the start of the event when event water reaches the aquifer causing the and piston effect at the basin outlet and spring. T_{Q0} is the start of quickflow reaching the basin outlet or spring. T_{QP} is the time when the peak contribution of quick-flow reaches the basin outlet or spring. T_{IP} is the time when the peak contribution of intermediate-flow reaches the basin outlet or spring. T_{S0} is the time when the start of slow-flow contribution reaches the basin outlet or spring.

Figure 2.1 Pathways in fluviokarst basins.

Precipitation (Pr) at the land surface either infiltrates to the soil (Q_{INF}) or runs off to sinkholes or the stream network (Q_{sur}). Soil water moves laterally to sinkholes or the stream network (Q_{lat}), percolates vertically through the soil profile to the epikarst ($Q_{perc.}$), or re-enters the atmosphere through evapotranspiration (ET). Stream water moves down gradient in the stream network (Q_{str}) or moves vertically to the subsurface *via* swallets ($Q_{swall\text{-}in}$). Swallet flow reverses direction during upwelling of groundwater flow to the stream. Water stored in the epikarst percolates vertically to the vadose zone ($Q_{ep\text{-}v}$) or moves to the fracture network ($Q_{ep\text{-}f}$), where it is generally considered the latter is activated during hydrologic events and wet times of the year. Sinkhole water also moves to the fracture network (Q_{sink} water stored in the vadose zone percolates as unsaturated flow (Q_{vadose}) until it reaches the water table. Water in perched aquifers or phreatic matrix exchanges with fractures ($Q_{pa\text{-}f}$) or higher porosity conduits ($Q_{f\text{-}c}$). Depending on human population density and land uses, water leaves the aquifer via well pumping (Q_{pump}). Water conveys through conduits to springs (Q_c). During very wet conditions such as an extreme hydrologic event, fracture networks and epikarst reaches their capacity, and overflow occurs to the stream network (Q_{over}), which leaves the basin via surface water outlets. (from Al Aamery et al., 2021)

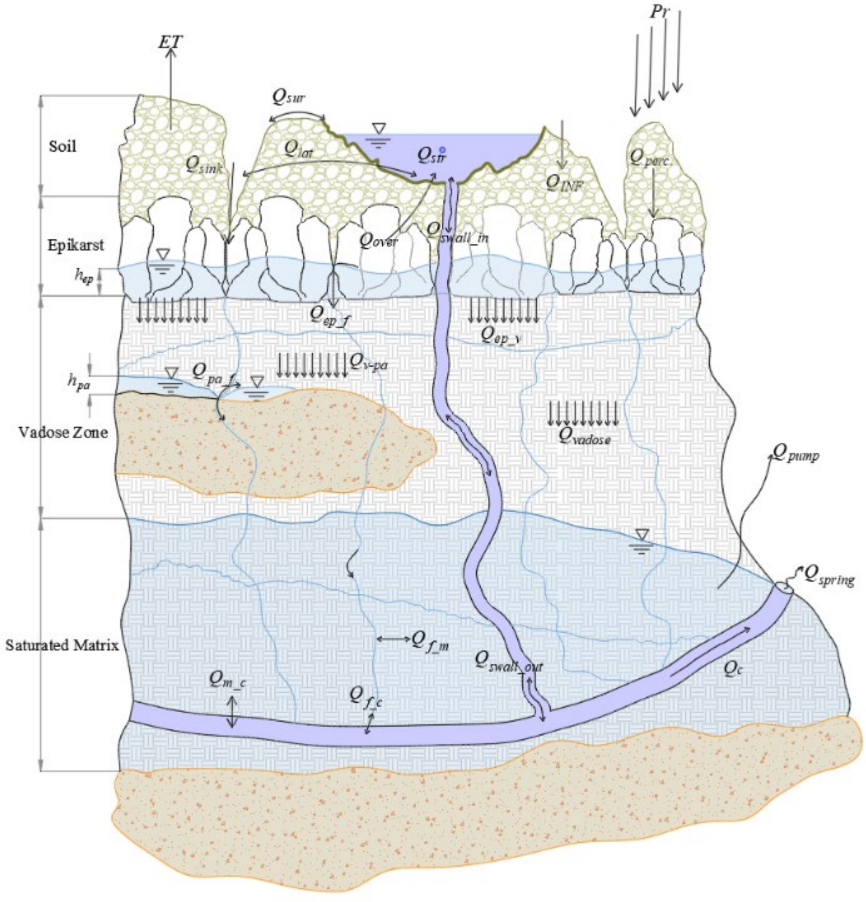

Figure 2.2 Concept model for hydrograph and nitrate chemograph in karst basins. This concept and earlier version of the figure was included in Husic et al. (2021, under review). This newer version includes the timing of different components.

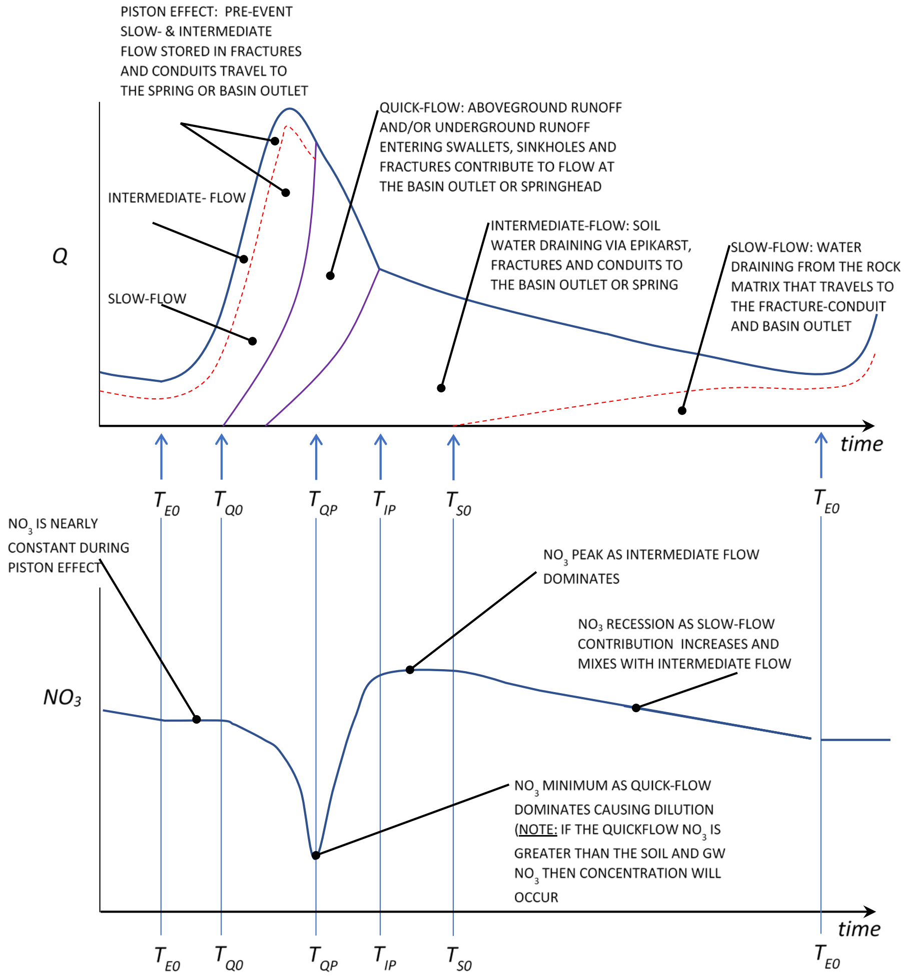

T_{E0}: Start of the event: event water reaches the aquifer causing the and piston effect at the spring

T_{Q0}: Start of quickflow reaching the spring

T_{QP}: Peak contribution of quick-flow at the spring

T_{IP}: Peak contribution of intermediate-flow at the spring

T_{S0}: Start of slow-flow contribution reaching the spring

Chapter 3 Study sites

3.1 Central Kentucky study site:

The primary study site in this thesis is the Upper South Elkhorn Watershed, which is in Fayette, Jessamine and Woodford counties in Kentucky, USA (Figure 3.1). This study karst basin drains approximately 62 km^2 consisting of agricultural (57%) and urban (43%) land uses. The main stem of the watershed is third order and is approximately 10 km long.

The watershed is characterized by low stream gradients, gently rolling upland hillslopes. Urban development by the City of Lexington within the watershed and heavy agricultural usage. The presence of pastureland and suburban areas with limestone bedrock promotes high background concentrations of bioavailable phosphorus. Bluegrass-Murray silt loams primarily make up the South Elkhorn watershed's soil matrix. Bluegrass-Murray silt loams are categorized under the hydrologic soil group "B", are very deep, well drained, and have moderate permeability (NRCS, 2011). The large amounts of underlying Lexington Limestone that heavily compromise the bedrock in the Upper South Elkhorn watershed attribute to a moderate karst potential (Currens, 1998).

The monitoring locations for nitrate in this thesis were located at the watershed outlet near the USGS Gauging station (named South Elkhorn site) and upstream (named Ramsey site). The Ramsey sensors are located at the bridge where Old Harrodsburg Road crosses South Elkhorn Creek. The sensors are housed in a metal box which is chained to a concrete bridge abutment in the center of the stream. The sensors are connected to a mobile sensor station with cables which feed along the bridge to the south west bank. The Ramsey site has a drainage area of 32.89 square kilometers. This area includes suburbs in the south of Lexington, and row crop farmland between Lexington and Nicholasville.

The South Elkhorn sensors are located north east at the bridge where Old Versailles Road crosses South Elkhorn creek. The sensors are zip tied to a metal structure which has been attached to the base of a concrete bridge abutment. The cables are fastened to the abutment and then along the bridge side to the north bank. On the bank is a USGS gage station, which houses our data collection station. The South Elkhorn creek site has a drainage area of 61.6 square kilometers, including the 32.9 square kilometers which drains to the Ramsey site. The additional are includes agricultural land, pastures, and a small portion of the Lexington Airport.

The watershed contains the mentioned USGS Gauging station (USGS 03289000) at the watershed outlet and a NOAA weather station (Lexington Bluegrass Airport) in the geographic center of the watershed.

3.2 Karst study sites published previously in the karst literature:

The South Elkhorn nitrate results from Ramsey site and Gage site and the concept model developed are also compared with results from a number of karst basins and karst springs with nitrate sensor data reported in previously published science journal papers. As shown in Figure 3.2, these sites were available from four karst regions in the United States including the carbonate karst and their aquifers in Kentucky, Arkansas, Virginia and Maryland, USA. In total, six sites across five drainage basins with karst bedrock had available nitrate sensor data available for analyses. Table 3.1 gives information for the six sites.

Husic et al. (2021) collected one year of Suna V2 nitrate data from the perennial Royal Spring site. Royal Spring is the largest spring (by annual water flowrate) in the inner bluegrass region of central Kentucky and drains a mixed surface water and groundwater basin. Karst hydrology in this basin is characterized by dolines across the landscape as well as over 60 identified in-stream swallets within the corridor of Cane Run creek (Husic et al., 2017). These swallets as well as the rest of the basin drain to a phreatic conduit, approximately 6 m^2 in cross sectional area, that daylights at Royal Spring. The nitrate sensor data was coupled with water flowrate data at a USGS gauge station located at Royal Spring.

Miller et al. (2016) collected one year of SUNA nitrogen concentration data in the Potomac watershed, which is influence by carbonate karst bedrock. The Upper Potomac River basin in Maryland, Pennsylvania, Virginia, and West Virginia contains 60% forested land and 35% agricultural land. The agricultural land was found to source 64% of N load. Two sites studied herein, in Maryland and Virginia, are as follows: Smith Creek an agricultural watershed, and Difficult Run an urban watershed. The nitrogen sensor data was paired with water flowrate data at USGS gauge stations located at each site.

Jarvie et al. (2018) collected three years of Suna V2 nitrate data from the Big Creek tributary station of the Buffalo National Scenic River located in the karst terrain of the Ozark Plateau in Arkansas, USA. The watershed was dominated by forest with agriculture that was particularly impacted by a permitted swine concentrated animal feeding operation. Herein, we analyze data collected downstream of the animal operation at 'Carver' which also had an established USGS gauge station (07055814).

Figure 3.1 South Elkhorn watershed located in central Kentucky, USA (Mahoney 2019)

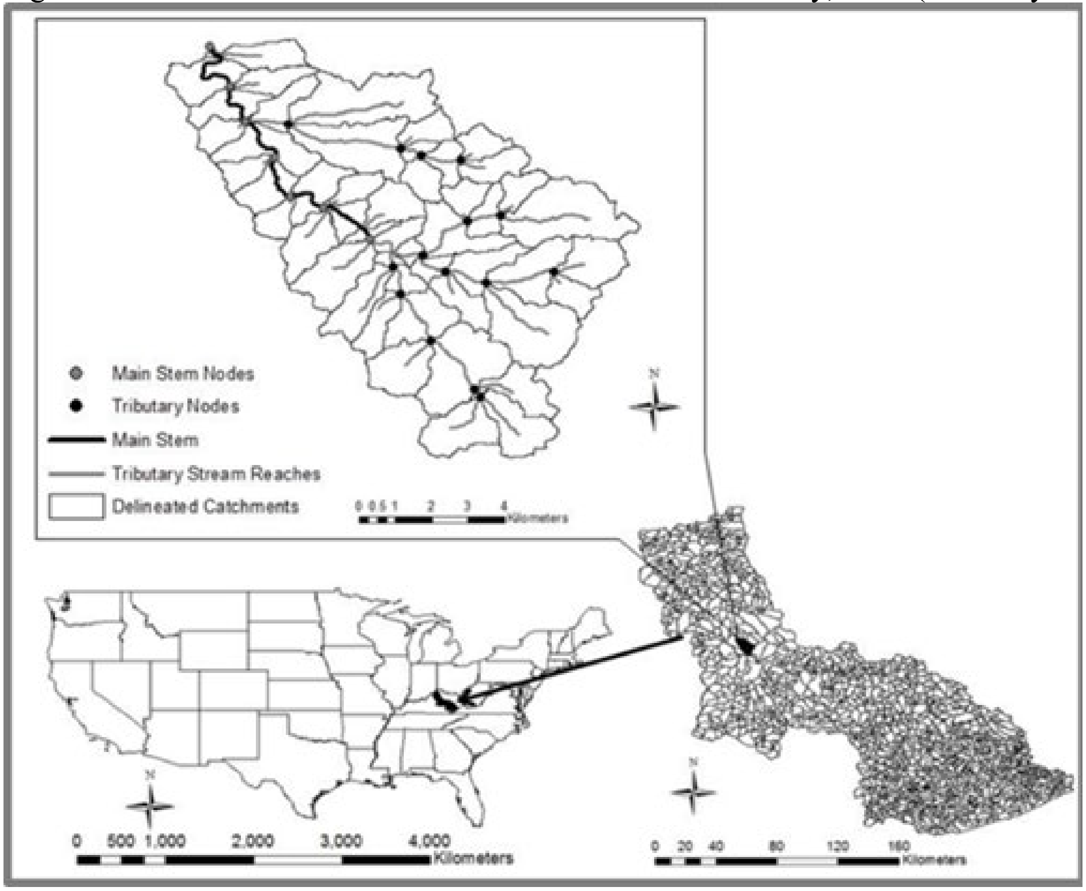

Figure 3.2 Kentucky Water Loop a), with focus on Kentucky River Lock and Damn 4 and 5 b) (Mahoney 2019)

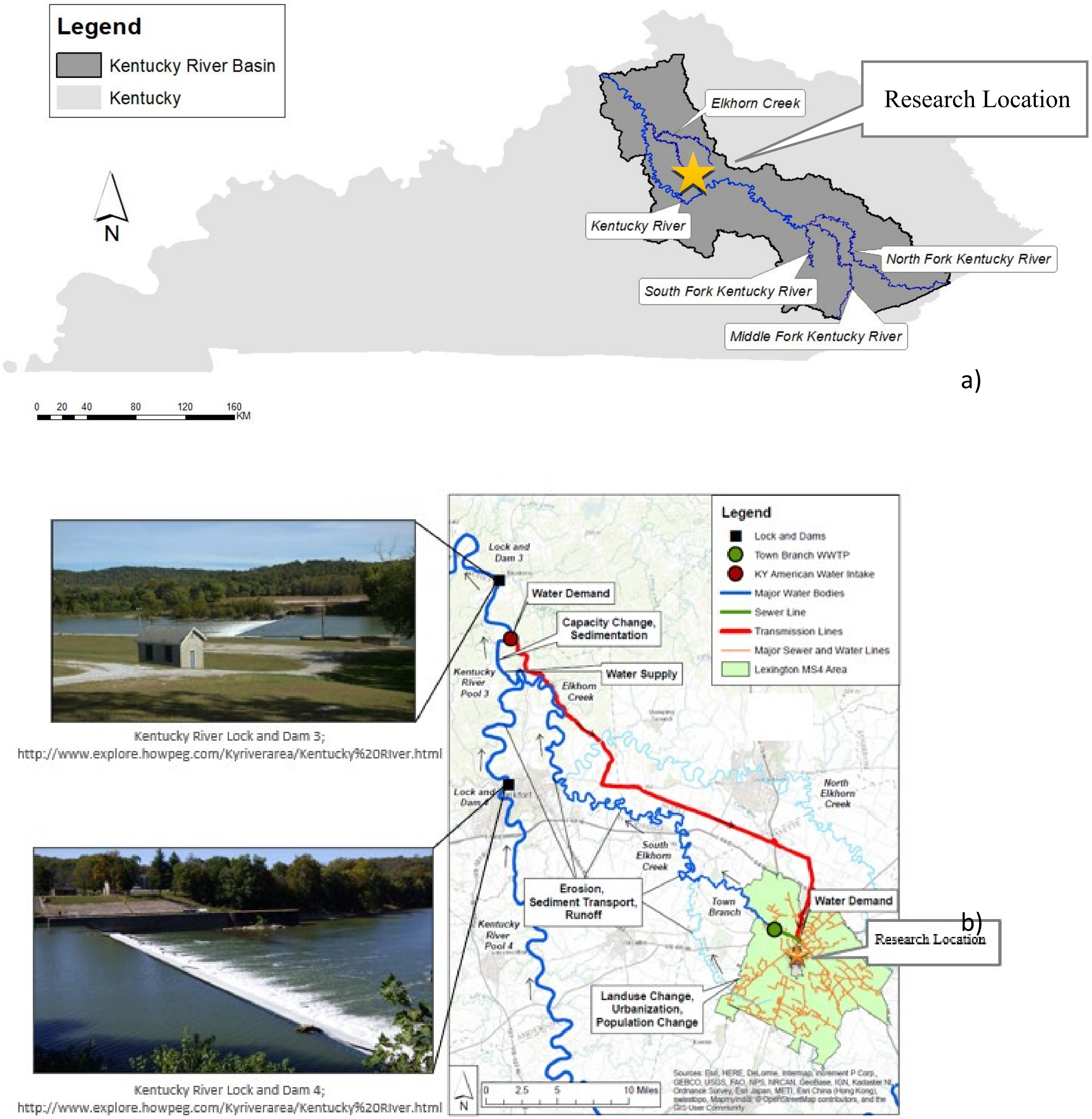

Kentucky River Lock and Dam 3;
http://www.explore.howpeg.com/Kyriverarea/Kentucky%20River.html

Kentucky River Lock and Dam 4;
http://www.explore.howpeg.com/Kyriverarea/Kentucky%20River.html

Figure 3.3 Location and Images of Study Sites SE Gage a) and Ramsey b) in the South Elkhorn Watershed (Mahoney 2019)

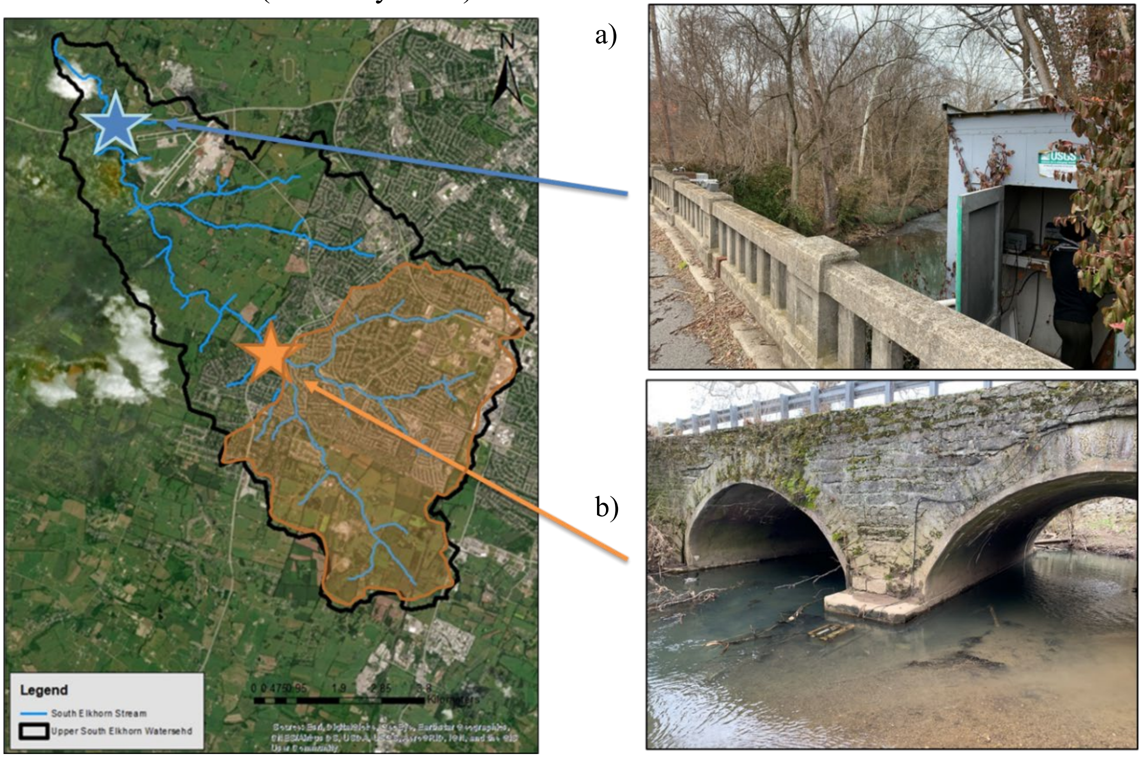

Figure 3.4 Land Use Map For South Elkhorn Watershed showing primarily urban development (red) and pasture (yellow), with zoomed in satellite images for the SE Gage a) and Ramsey b) sites (Mahoney 2019)

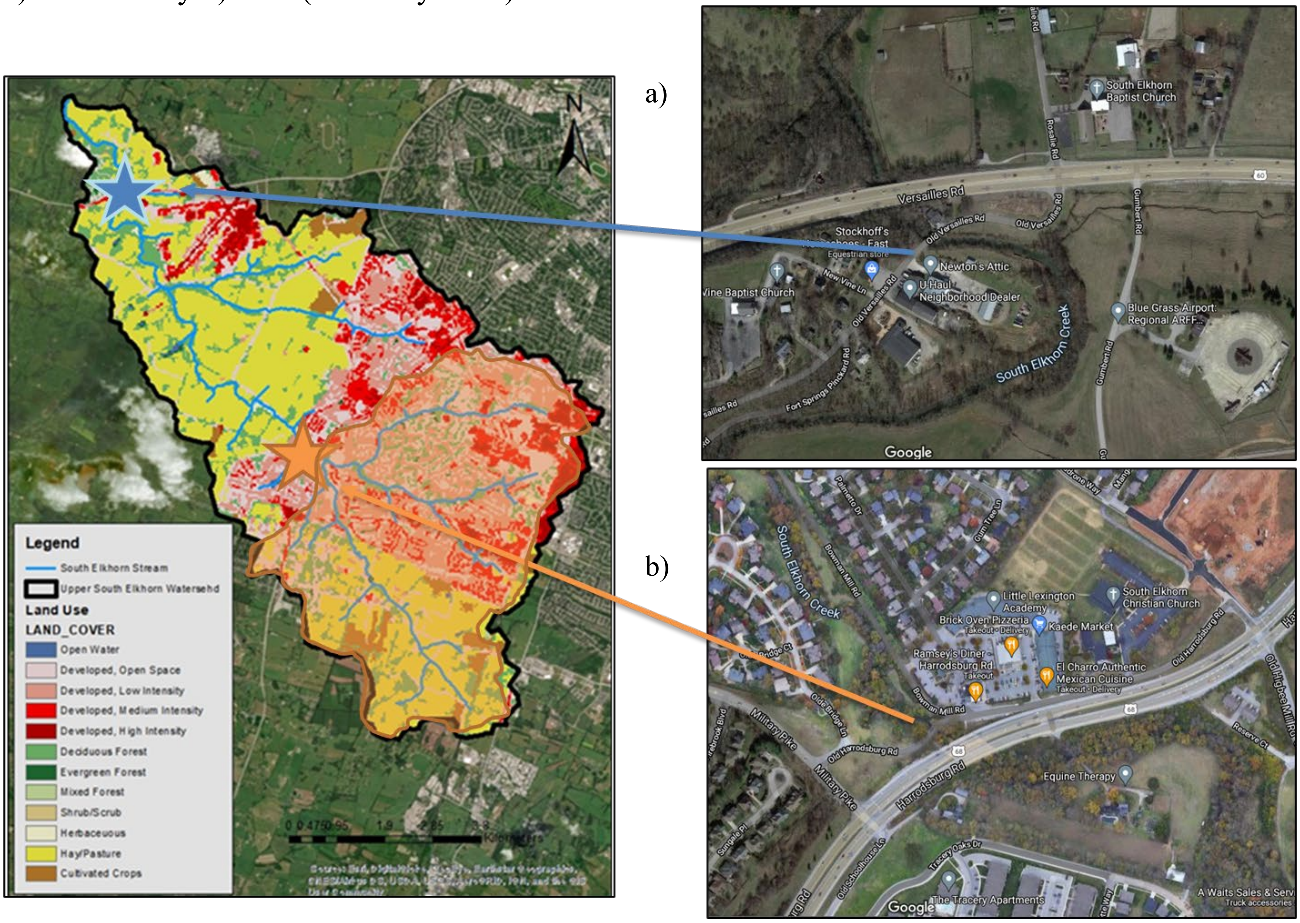

Figure 3.5 Karst map for the United States and location of the four regions studied (from the Karst Waters Institute, and compiled from the USGS karst map and database and the USGS Groundwater Atlas of the United States)

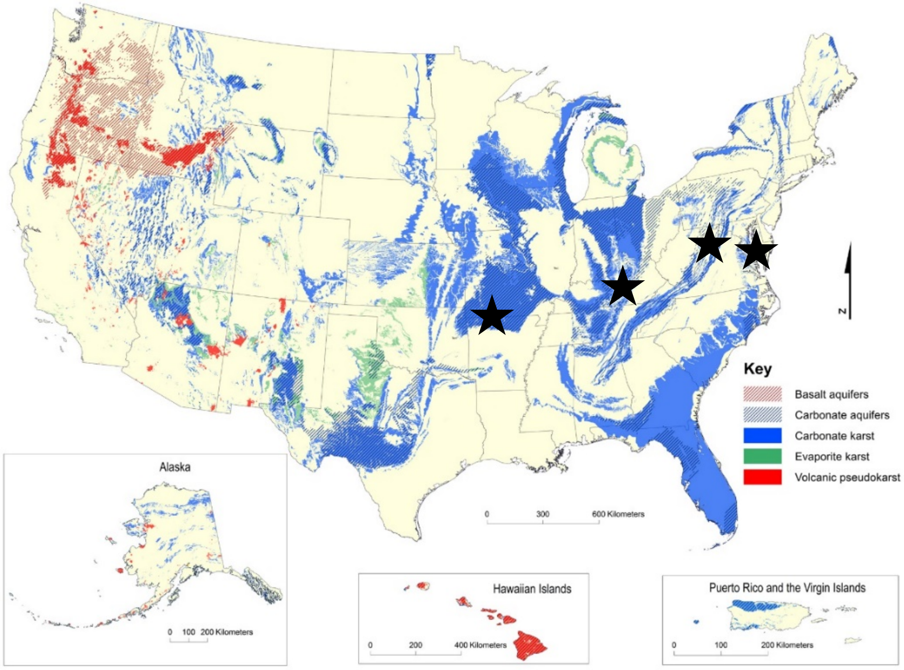

Figure 3.6 Kentucky Karst Map (Kentucky Geological Survey)

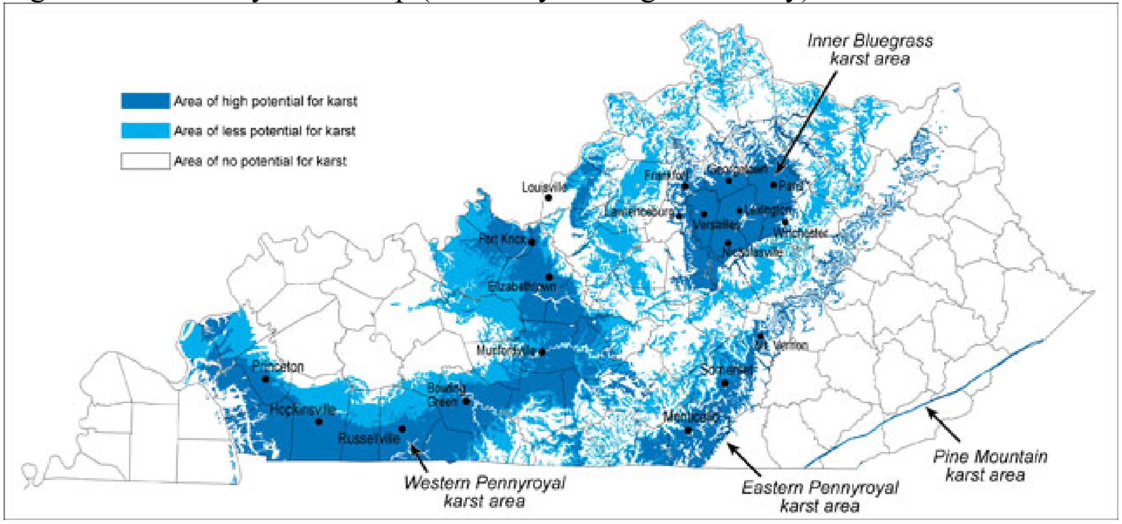

Figure 3.7 South Elkhorn Watershed Sinkhole Map (Mahoney et al 2018)

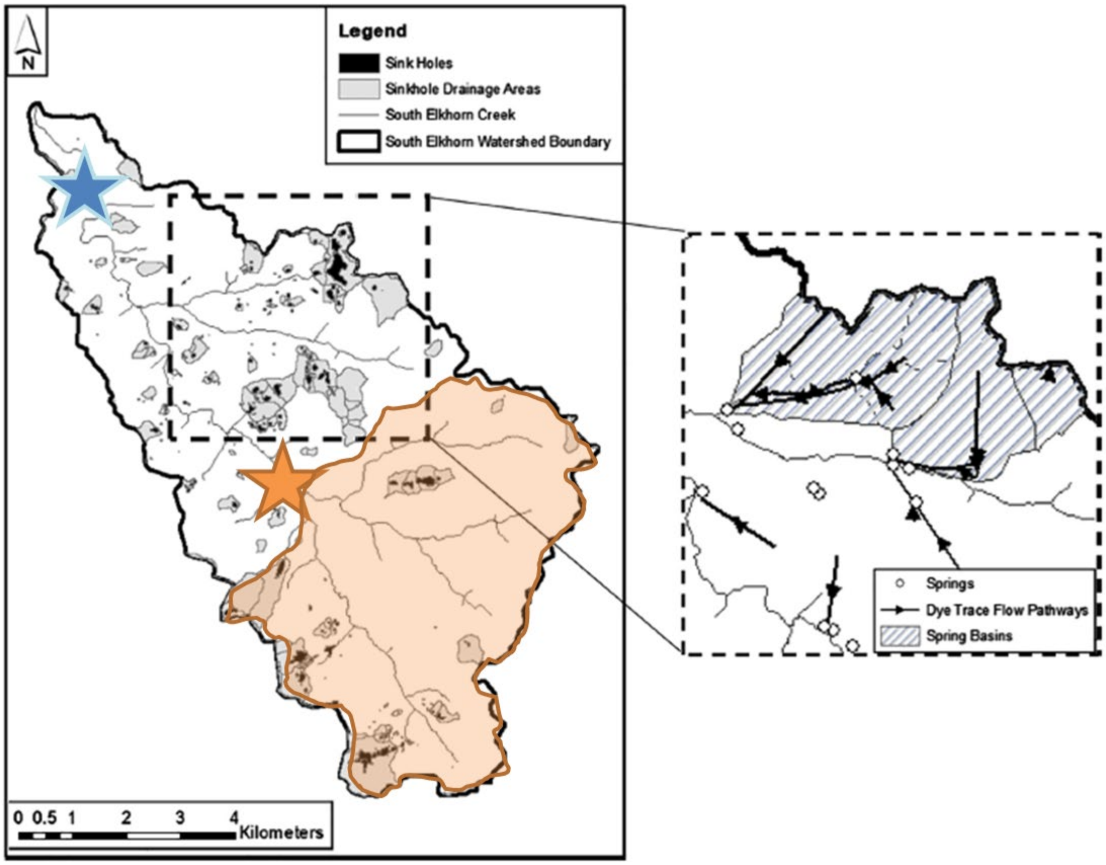

Table 3.1. Study sites with nitrate sensor data analyzed in this study.

Site name	**Basin name**	**Basin location**	**Karst bedrock**	**Drainage area at sensor**	**Land use draining to the sensor**	**Journal paper**
South Elkhorn Gage	South Elkhorn watershed	Kentucky, USA	Carbonate karst	62 km^2	Agricultural pasture, horse farms, cattle farms, urban/suburban	This study
South Elkhorn Ramsey	South Elkhorn watershed	Kentucky, USA	Carbonate karst	30 km^2	Agricultural pasture, horse farms, cattle farms, urban/suburban	This study
Royal Spring	Cane Run Royal Spring basin	Kentucky, USA	Carbonate karst	58 km^2	Agricultural pasture, horse farms, cattle farms, urban/suburban	Husic et al. (2021)
Smith Creek	Potomac River watershed	Maryland, USA	Carbonate karst	250 km^2	Agricultural land use	Miller et al. (2016)
Difficult Run	Potomac River watershed	Virginia, USA	Carbonate karst	150 km^2	Urban land use	Miller et al. (2016)
Big Creek	Buffalo River Watershed	Arkansas, USA	Carbonate karst	236 km^2	Agricultural with swine animal feeding operation, forest	Jarvie et al. (2018)

Chapter 4 Methods

4.1 Nitrate and water flowrate data collection and quality assurance quality control:

4.1.1 Sensor stations:

Fifteen minute nitrate sensor data was collected over a four year period with two SUNA V2 ultraviolet nitrate analyzers at both SE Ramsey and SE Gage stations, and the nitrate data was complimented with water flowrate measurements via stage recorders, and pH, conductivity, dissolved oxygen, turbidity and temperature measurements using YSI EXO 3 sondes. Over one year (or 14 months) of data was collected at SE Ramsey, and over two years (or 29 months) of data was collected at SE Gage.

The SUNA V2 measures light absorption at varying wavelengths with an on-board spectrometer to estimate nitrate concentration (Figure 4.1). SUNA V2 sensors measure both nitrate (NO_3^-) and nitrite (NO_2^-), and we assume nitrate dominates the measurements consistent with other, similar studies (Terrio et al., 2015). Measurement range for the SUNA V2 is 0.035 to 56 mg-N l^{-1}, and accuracy is ±30% at the highest extent of this range (Figure 4.1).

Other water quantity and quality parameters were also measured at SE Ramsey and SE Gage sites. Water temperature, dissolved oxygen, pH, conductivity, and turbidity were measured with YSI EXO 3 sondes. Some parameters were recorded by individual sensors connected to the sonde. Turbidity and dissolved oxygen probes utilized optical sensor technology. pH and conductivity probes utilized sensor electrode technology. All four of these probes were cleaned regularly with an attached wiper. Temperature was measured from within the sonde with an on-board thermistor.

Sensor wires ran from the frame to a Campbell Scientific CR-1000 Dataloggers (Figure 4.2) located on the stream banks. The datalogger was set up to use SDI-12 connection to run an operation script which read and stored sensor data locally at 15-minute intervals. Sensors and the data logger were powered by a 12-volt battery which is replaced every one to two weeks. The sensor platform at South Elkhorn Gage site was installed on the downstream side of the mid-stream bridge pier of Old Versailles Road (Figure 4.3). Wires ran from the pier to a USGS gage station where the data logger was placed. The sensor platform at the Ramsey site was a cage which is chained to the mid-stream bridge pier over Old Harrodsburg Road. Wires ran from the cage along the bridge to a waterproof box on the stream bank.

4.1.2 Sensor Maintenance and Calibration Procedures:

The sensors used in this study were calibrated and cleaned every three months for the duration of the project. Our calibration procedures for the SUNA V2 nitrate sensor and YSI Multiparameter sondes followed the steps outlined in each respective sensor manual (Sea-Bird Coastal, 2016 , YSI, 2012). Each sensor came with a partner software which helped mediate the calibration process. This is SUNACOM for the SUNA V2 and KOR exo for the Exo3. Detailed maintenance and calibration procedures are in Appendix A-1 and A-2.

4.1.3 Sensor Troubleshooting Framework:

We often experienced unexpected issues in the data collection process. Often this would manifest as an inability to connect to the sensors through the data logger. We found out the steps to solve this problem through trial-and-error and communication with Sea-Bird Coastal and Campbell Scientific technicians. We would call the technicians and discuss problems with the sensors and data loggers. The Campbell Scientific technicians were especially helpful, even sometimes writing code to help us solve problems. The troubleshooting steps were as follows:

First, you must check that power is being supplied throughout the whole circuit. You can check this with a voltmeter, using the positive and negative ends at various spots along the entire system circuit, including the female end of the sensor cable. This will reveal possible hardware issues in the wires, fuse box, data logger, or sensor cables. Once a power supply item was found, these may need to be repaired or replaced.

Second, the next step is to attempt to communicate with the sensors using the data logger software. You can give a specific command in the terminal emulator window which will return if the data logger is able to communicate with the sensor. If the sensor can communicate with the data logger, but no readings are given you can try to revert the code to a previous version. If this works you can try to identify the differences between the old and new codes. Often, the computer codes need to be updated, and therefore some computer programing must be performed.

Third, if problems still persist after following these steps, it was most helpful to call Campbell Scientific if both sensors are not working or YSI or Sea Bird if you have isolated the problem to only one sensor.

4.1.4 Sensor QAQC Procedures:

The South Elkhorn Gage and Ramsey sensor sites operated continuously and were scripted to record measurements every 15 minutes. This data was saved and tabulated by the Campbell Scientific Data Logger at both sites. This raw data was downloaded manually every one to two weeks and then uploaded to a shared cloud folder. Duplicate files were kept to protect against data loss.

Secondary data parameters such as stream flow, stream stage, precipitation, and air temperature were collected for both sites. A United States Geological Survey (USGS) stream gaging station was located at the South Elkhorn Gage site which provided stream discharge and stage measurements. These measurements were converted to Ramsey measurements using a weighted drainage area method corrected for travel time. The method for estimating SE Ramsey streamflow was verified with a pressure transducer at the Ramsey site, and the event peaks and critical points from the travel time correction method agreed well with the pressure transducer results. A National Oceanic and Atmospheric Administration climatological gaging station located at the Lexington Bluegrass Airport near the Upper South Elkhorn watershed outlet was available for precipitation and air temperature measurements collected daily.

It was vital for us to ensure high quality data for the duration of our temporal sensor water quality data collection process. Accurate time-series data for all parameters was vital for reliable data analysis, particularly when comparing data parameters against each other. Three quality assurance goals were developed to help bolster the correctness of data collected by the sensor platforms. First, precise calibrations and cleanings of all sensors was performed every 3 months. Second, a numerically based quality assurance flagging script developed by University of Georgia was adapted for our sensor network. This script, run through MatLab R2021a, called the GCE Data Toolbox would sift through raw data files and identify abnormalities based on our input parameters. This process is described more thoroughly in the following paragraph. The third quality assurance method was to collect discrete nitrate samples for each platform site on a monthly basis. Three samples were collected each sampling session. Two samples, one from each site was labeled with location and time. A third sample, chosen randomly between each site, was delivered unmarked as a control against laboratory bias. All samples were analyzed by Jason Backus in the Kentucky Geological Survey Water Quality Laboratory on the University of Kentucky campus. Nitrate was measured by the KGS 9056 *Ion Chromatography of Water* method adapted from the Environmental Protection Agency Method 300.0: *Determination of Inorganic Anions by Ion Chromatography*. This method involves injecting a small volume of water into an ion chromatograph. The sample is pumped through three different ion exchange columns and into a conductivity dispenser. In these columns, lined with strongly basic anion exchanger, ions are separated into discrete bands based on their affinity for the exchange sites of the resin. The final column removes background conductivity and converts the anions in the sample to their corresponding acids. Conductivity of these acids can be measured with an electrical conductivity cell and compared with known standards to determine nutrient concentration. Results of discrete sample analysis were compared directly with SUNA V2 readings. If needed, miscellaneous water quality data including temperature, dissolved oxygen, conductivity, and pH recorded by the EXO 3 were compared with readings gathered from USGS gaging station at the Upper South Elkhorn watershed outlet.

Potentially erroneous data was identified using the automated GCE Data Toolbox simulated in Matlab R2021a and the toolbox was adapted from the work of Georgia Costal Ecosystems LTER Project. The QAQC software scanned and flagged based on an invalid range, questionable range, percentage change, missing value, and data falling outside three data standard deviations. For each parameter, a range of "impossible readings" have been programmed, for example temperature range goes from -5 °C to 50 °C. Questionable ranges have been established as well, the temperature questionable range goes -0.1 °C to 30 °C. Percentage change flags when a point is 20% greater or less than the proceeding value. Missing value flags when there is no data given. Standard deviation flags when a value is not within three standard deviations. The software outputs the dataset with a column of flags including I - Invalid, Q - Questionable, P - Percentage, M - Missing, and S – Standard Deviation. To continue with the QAQC process, the flags were reviewed and determined if the data point needed to be removed. Once this was completed, a monthly screening report is written which records the total number of flags, the total number of removed data points, and an explanation for each removed data point.

4.2 Meta-analyses of karst hydrographs, nitrate chemographs and hysteresis:

Nitrate datasets were investigated from karst basins in Kentucky, Arkansas, Maryland and Virginia to provide qualitative support of the concept model in Figure 2.2. To do so, hydrographs and chemographs for the six sites (Table 3.1) were analyzed to show potential efficacy of the model. Water flow rate (Q) and nitrate concentration measurements (NO_3) were extracted from our mentioned sensors South Elkhorn sensors, USGS gages, or from previously published datasets. Next, storm events followed by low flow periods were extracted from the datasets to allow comparison with the concept model. Karst hydrographs and nitrate chemographs analyses followed by hysteresis analyses were carried out for each storm event followed by low flow sequence extracted from each site.

The hydrographs and nitrate chemographs were used to identify the existence, or lack thereof, of the main features of the concept model including: the piston effect, quickflow dominance, intermediate flow breakthrough, and nitrate recession with a two porosity model for karst baseflow. The piston effect was identified when nitrate showed a constant value or slightly changing value as the water flowrate increased during the rising limb of the hydrograph. Quickflow dominance was identified when nitrate decreased or increased substantially, indicating dilution or concentration, respectively, from above ground runoff or underground runoff. Intermediate flow breakthrough was identified when nitrate reached a maximum, or minimum, a few days after the hydrograph peak, which indicates the breakthrough of soil water percolation reaching the sensor station. Nitrate recession was identified when the hydrograph decreases or reaches a constant while NO_3 shows a pronounced recession. Hysteresis analyses was carried out for each storm events followed by low flow sequence extracted from each site. Hysteresis involved classifying the events as clockwise or anti-clockwise and helped to identify the piston effect.

4.3 Mass balance un-mixing modelling to quantify sources of water and nitrate:

Mass balance and un-mixing modeling was completed for the SE Gage and SE Ramsey sites for one event in four months, including January, April, July, and October. These months were chosen due to a high concentration of events in the month and an event separation throughout the year represented by each season. The event chosen for each month was the largest flow event, apart from in October. The October event was chosen due to the unique circumstances of following a drought period where nitrogen and flow reached minimum levels.

The mass balance process un-mixed the following four flow paths: piston flow, quick flow, intermediate flow, and slow flow. We used the times defined in Figure 2.2 to identify the critical points of separation between flow paths. T_{E0} is the start of the event when event water reached the aquifer causing the piston effect at the basin outlet and spring. This point was identified as when flow begins to rapidly increase at the start of the event. T_{Q0} is the start of quick flow reaching the basin outlet or spring. At this point, nitrogen will begin decreasing from pre-event levels for this basin, because dilution occurs during events. This point was identified as the moment when nitrogen levels begin to fall. T_{QP} is the time when the peak contribution of quick flow reaches the basin outlet or spring. This point was identified as the point of local minimum nitrogen concentration during the event. T_{IP} is the time when the peak contribution of intermediate flow reaches the basin outlet or spring. This point was identified as the local maximum point of nitrogen concentration during the event. T_{S0} is the time when the start of slow-flow contribution reaches the basin outlet or spring. This point was interpreted as following immediately after T_{IP} when the nitrogen decreases below the local maximum point.

The general nitrate mass balance un-mixing problem was solved using chemograph separation methods. The nitrate mass balance is

$N_T Q_T = \sum N_i Q_i$, and (Equation 4.3.1)

$Q_T = \sum Q_i$, (Equation 4.3.2)

where each term is a nitrate mass flux, and N and Q indicate nitrate concentration (mg-N l^{-1}) and volumetric flowrate of water ($m^3 s^{-1}$), respectively. The subscript T indicates the location of the sensor station where chemograph separation is carried out, and the analyses is carried out independently at each time step for i contributing sources (e.g., quickflow, intermediate flow, and so forth). To complete the un-mixing model, T_{E0}, T_{Q0}, T_{QP}, T_{IP}, and T_{S0} were identified for each event separately at both SE Gage and SE Ramsey's sites. Several assumptions were implemented to solve Equations 4.3.1 and

4.3.2 across the entire event using the sensor data as follows. The nitrogen concentration value at T_{E0} was used to represent piston flow; the nitrogen concentration at T_{QP} was used to represent quick flow; and the nitrogen concentration at T_{IP} was used to represent intermediate flow. The nitrogen concentrations of slow flow were estimated to be 0.5 mg-N l^{-1} based on the minimum total nitrogen values at South Elkhorn Gage and Ramsey site which occurred in September and early October 2019 during an extended dry period. During the analyses, it was assumed that two flow paths dominated hydrologic activity at any one time as: the piston flow path was active between T_{E0} and T_{QP}; the quick flow path was active between T_{Q0} and T_{IP}; the intermediate flow path was active between T_{QP} and the end of the event; and the slow flow path was active between T_{S0} and the end of the event. Equations 4.3.1 and 4.3.2 were solved for unknowns, Q_i's, given nitrate sensor and volumetric water flowrate estimated at the sensors and the mentioned assumptions for nitrate concentration values of sources.

$$Q_{Ratio(source\ 2)} = \frac{N_{(i)} - N_{(source\ 1)}}{N_{(source\ 2)} - N_{(source\ 1)}}$$

$$Q_{Ratio(source\ 1)} = 1 - Q_{Ratio(source\ 2)}$$

4.4 Reservoir modelling for nitrate transfer in the karst basins:

A reservoir model was formulated to test the potential for predicting key features of the hydrograph and chemograph concept model, including, the piston effect, quickflow dominance, intermediate flow breakthrough, and nitrate recession, as well as provide a tool for estimating water and nitrate storage and fluxes and prediction. The reservoir model represented the karst basin using several lumped geographic features (i.e., reservoirs) corresponding to the soil-epikarst, primary porosity rock-matrix, secondary porosity fracture network, and tertiary porosity conduit network. In this way, the reservoir modelling approach reflects the triple porosity concept cited for karst aquifers (White, 2002). Runoff was treated and routed separately following the hydrologic travel time modelling method of Mahoney et al. (2020).

The reservoir model formulated for this study (Figure 4.4) simulates storage and flux for the mentioned reservoirs. Total rainwater is modeled to precipitate onto the soil reservoir. Rainfall addition directly onto the stream is assumed to be negligible. A small layer of epikarst - wider karst fractures in the ground – lies below the soil reservoir, but travel time through this is so short that it will be considered together as one reservoir with the soil. Once on the soil-epikarst reservoir, water can runoff latterly towards the stream, fall into the karst system through sinkholes causing the piston effect, or seep down into the fracture and conduit reservoir. The piston effect water will come out into the riverbed through springs via the conduit network. Water in the fracture network can flow to the stream through intermediate flow or transfer back and forth with the rock matrix and micropore reservoir. Water in the micropore reservoir will transfer to the fracture network as mentioned or flow to the stream through slowflow.

Following from the conservation of mass for a control volume approach, the volume of water in a reservoir was calculated as the volume from the previous time step minus the volume leaving and plus the volume entering the system during the current time step. We estimate the volume of water in the soil reservoir before the event using data from the NOAA National Climatic Data Center. This data gives us the soil moisture percentages at 5, 10, 20, 50 and 100 cm depths. We will assume the soil volume at time step -1 is equal to a percentage of the total volume as the ratio of the current soil moisture to the maximum soil moisture over the year. The drainage area of the watershed is found separately at the Ramsey site and the SE Gage site using the USGS streamstats program. All area is assumed be karst, as seen in Figure 3.6, with the same concentration of underground karst features aside from sinkholes. Sinkholes are similar to expended fractures which will deliver water directly to the conduit. The initial sinkhole drainage area is estimated to be 13% (Mahoney et al 2018). This value will be adjusted as a calibration parameter. The height of the soil reservoir is estimated to be 1 meter based on soil survey information. The height of bedrock is estimated as the difference of the average height of the watershed, gathered from the streamstats program, and the height of the outlet, gathered from USGS topographic maps. This bedrock height is used in the calculation of volumes for the fracture network and rock matrix reservoirs which both exist side by side in the Lexington limestone. Porosity of Lexington limestone is initially estimated to be 0.5% (MacQuown 1967). This porosity is multiplied by the volume of limestone to estimate the rock matrix water storage potential. Volume of the fracture network begins by estimating a 10 mm fracture diameter, the fracture is assumed to be a circular pipe. The fractures are estimated to be 4 m apart in the vertical and horizontal direction. This 4m grid is used to estimate the total volume of fractures. The volume of water storage of the fracture network is the product of fracture area and fracture volume. The volume of the conduit is estimated to always be full. This volume was estimated using the average volume from the results of cumulative piston effect flow in the 4 events studied in chapters 4.3 and 5.3.

Precipitation data is gathered from the National Centers for Environment Information hosted by NOAA. This data is converted into a runoff hydrograph using the method introduced by Mahoney (2018). This method, developed by Mahoney, is an adjusted unit hydrograph method which has been set up for use in the South Elkhorn watershed. The method maps out 181 sub-basins in the South Elkhorn watershed which were identified through field investigations in 2017. High-resolution LiDAR and Manning's equation was used to identify land use and estimate overland flow velocity in each sub basin. Flow length was determined by the flow length algorithm in ArcGis. Flow length was divided by velocity for each flow cell in each sub-basin to determine the period (in hours) for which overland flow would propagate from that cell. Precipitation data at each hour was multiplied by the ratio of active flow cells to total flow cells to determine the flow contribution for that hour. The Green Ampt model (1911) is used to estimate the depth of infiltration of precipitation into the soil. This method considers the maximum soil infiltration and the pre-event soil infiltration. To use this model, the user inputs soil porosity, and rate of flow through the soil. Event precipitation is entered as mm/h as well has the total number of hours in the event. Initial soil moisture is inputted from USGS 5 feet soil moisture data in Versailles Kentucky. This initial soil moisture will be different for each event. Once all soil and event parameters are inputted, the user guesses a value for total soil infiltration. The model calculates time of the event based on the soil infiltration. Soil infiltration is then increased or decreased so that the modeled time of the event matches reality. Finally, total infiltration depth is subtracted from total rainfall to estimate the runoff depth. Each totaled result from Mahoney's runoff hydrograph model was multiplied by the ratio of total runoff to total precipitation to estimate the runoff for that hour. Of the runoff flow, initial estimates are that 80% will flow into the stream and 20% will flow into the conduit via the fracture network, causing the piston effect.

The following formulas for modeling the flow between reservoirs were adapted from Husic et al 2019.

Soil reservoir volume at each time step is calculated with the following formula.

$$V_{Soil(i)} = V_{Soil(i-1)} + \left(R_{(i)} - Q_{SoilOverflow} - Q_{Soil} \right) * \Delta t$$

(Equation 4.4.1)

Where $V_{Soil(i-1)}$ is the soil volume from the previous timestep. $R_{(i)}$ is the recharge to the soil reservoir which is equivalent to precipitation minus runoff. $Q_{SoilOverflow}$ and Q_{Soil} are the flows out of the soil reservoir. Δt is the timestep of 1 hour in units of days.

$Q_{SoilOverflow}$ represents soil overflow in which the soil reservoir fills up and the remaining water converts to overland runoff. K_{stream} is the discharge coefficient for runoff and lateral flow to the surface stream. This is calculated with the following formula.

$Q_{SoilOverflow} = MAX\ (\ 0, K_{tream} * \left(\ V_{Soil(i)} - \ V_{Soil(max)}\right) * \Delta t)$ (Equation 4.4.2)

Q_{Soil} represents the water which flows out of the soil reservoir, including the epikarst system, and to the fracture network in the limestone bedrock. This is calculated with the following formula. K_{soil} is the soil percolation coefficient.

$Q_{Soil} = MAX\ (\ 0, K_{soil} * \left(\ {V_{Soil(i)}}^{\beta 1}\right) * \Delta t)$

(Equation 4.4.3)

$V_{fractureNetwork(i)}$ represents the volume of water in the fracture network at the current time step and it calculated by the formula below. Where $Q_{fractureNetwork}$ is the flow from the fracture network to the conduit. Q_{fNtoRm} is the flow from the fracture network to the rock matrix.

$$V_{fractureNetwork(i)} = \ V_{fractureNetwork(i-1)} + \left(\ Q_{Soil} - \ Q_{fractureNetwork} - \ Q_{fNtoRm}\right) * \Delta t$$

(Equation 4.4.4)

$Q_{fractureNetwork}$ is calculated using the following formula. $\alpha 2$ is the recession coefficient for intermediate flow.

$$Q_{fractureNetwork} = MAX\ (\ 0, \alpha 2 * \left(\ {V_{fractureNetwork(i)}}^{\beta 2}\right) * \Delta t)$$

(Equation 4.4.5)

Q_{fNtoRm} is calculated using the following formula which contains an if statement which outputs zero if DV is negative. DV is the difference between the rock matrix and the fracture network. negative. These two reservoirs will constantly exchange water to reach equilibrium. $\alpha 4$ is the recession coefficient for the exchange of water between the fracture network and the rock matrix.

$$Q_{fNtoRm}\ = IF(DV > 0, \alpha 4 * V_{fractureNetwork(i-1)} * \Delta t, 0)$$

(Equation 4.4.6)

The volume of water in the rock matrix, $V_{rockMatrix(i)}$ is calculated with the following formula. Q_{RmtofN} is the exchange of water from the rock matrix to the fracture network, and is calculated by the same method as Q_{fNtoRm} but with DV < 0 in the if statement. $Q_{rockMatrix}$ is the flow from the rock matrix to the conduit, this is also known as slow flow.

$$V_{rockMatrix(i)} =\ V_{rockMatrix(i-1)} + \left(\ Q_{fNtoRm} -\ Q_{RmtofN} -\ Q_{rockMatrix}\right) * \Delta t$$

(Equation 4.4.7)

$Q_{rockMatrix}$ is calculated with the following formula. $\alpha 3$ is the recession coefficient for slowflow.

$Q_{rockMatrix} = MAX\ (\ 0, \alpha 3 * \left(V_{rockMatrix(i)}{}^{\beta 3} \right) * \Delta t)$

(Equation 4.4.8)

Recall that $V_{conduit}$ is assumed to be always full. $Q_{conduit}$ is calculated as the sum of $Q_{fractureNetwork}$, $Q_{rockMatrix}$ and $Q_{sinkholeRunoff}$. $Q_{sinkholeRunoff}$ is a percentage of the Q_{Runoff} that represents the assumption that some overland runoff will fall into sinkholes in the south elkhorn watershed which lead to a conduit.

Nitrogen concentrations for each of the following flow paths: piston flow (sinkhole runoff) , quickflow (stream runoff) , intermediate flow (fracture network) , and slowflow (rock matrix) are gathered on an event basis from the study of event dynamics in chapters 4.3 and 5.3. The mass of nitrogen in the conduit is then represented by the following formula.

$N_{conduit} = N_{fractureNetwork} Q_{fractureNetwork} + N_{rockMatrix} Q_{rockMatrix} +$
$N_{sinkholeRunoff} Q_{sinkholeRunoff}$

(Equation 4.4.9)

The mass of nitrogen in the stream is calculated by the following formula.

$N_{stream} = N_{conduit} + N_{streamRunoff} Q_{streamRunoff}$ (Equation 4.4.10)

4.4.1 Model Calibration Procedures

Calibration of the model begins by matching the quick flow and piston effect runoff

(QstreamRunoff and QsinkholeRunoff) with the quickflow and piston effect runoff totals which were determined in sections 4.3 and 5.3. Parameters which impact the value of the model runoffs are runoff percentage from the Green Ampt model. and sinkhole percentage. The input runoff data, which was determined by the method from Mahoney (2019) was also adjusted so that the total volume of runoff is distributed in a shape which is accurate to the 4.3 and 5.3 results. This involved adjusting the values for the number of cells contributing to the watershed outlet at the time step. These numbers will have a short high slope to reach the maximum runoff then a longer, more gradual slope before reducing to zero once there is no more runoff contribution. The distribution of these numbers was adjusted to best match the runoff conditions. The time of the beginning of each flow contribution in the model was adjusted to reflect how water will reach the Ramsey site earlier than it will reach the South Elkhorn site. Water may also take more or less time to reach each site under differing seasonal conditions. The proceeding parameters were adjusted until the flow magnitudes and shape were aligned.

Once runoff is matched, flows out of the fracture network and rock matrix (QfractureNetwork and QrockMatrix) which represent intermediate flow and slowflow were matched with the intermediate flow and slowflow results from sections 4.3 and 5.3. Flow out of the fracture network is impacted by the height of bedrock, fracture diameter, distance between fractures, drainage area, α2, β2, initial soil moisture percentage, and the volume in the fracture network. Flow out of the rock matrix is impacted by the height of bedrock, porosity of bedrock, drainage area, α3, β3, initial soil moisture percentage, and the volume in the rock matrix. The proceeding parameters were adjusted until the flow magnitudes and shape was aligned. The timing of intermediate flow from the fracture network and slow flow from the rock matrix needed to be delayed to reflect the timings determined in sections 4.3 and 5.3.

4.4.2 Implementation of Calibration Procedures for Each Event

To calibrate for the January 2019 event at SE Gage quick flow magnitudes are matched by finding the runoff % from the Green ampt model to be 66.3%. From this point, the modeled quick flow curve was wider and flatter than the actual storm event. To fix this, the values from the Mahony 2019 method are adjusted. To match the timing, the runoff is adjusted to begin at 1/4/2019 23:00, 12 hours after the rainfall begins. The piston effect timing was determined to last from 1/4/2019 13:00 to 1/5/2019 2:00. A triangular distribution of runoff is formed with 12 hours of upwards slope and 2 hours of downwards slope. These slope values were determined by dividing the total magnitude of piston effect runoff (sinkhole runoff) by the timing of the piston effect. The total piston effect runoff is a percentage of the total runoff. Finally, the sinkhole percentage was adjusted to 20% so that streamflow and piston flow best matched the data results. The fracture network flow (intermediate flow) was adjusted by setting α2 at 0.23 and β2 at 1.11. The fracture network flow is lagged by 15 hours to reflect our concept of when intermediate flow contribution begins. The rock matrix flow (slow flow) was adjusted by setting α3 at 0.005, β3 at 1 and rock matrix porosity at 0.005. The rock matrix flow was lagged by 70 hours to reflect our concept of when slow flow contribution begins.

To calibrate for the January 2019 event at Ramsey site the same calibration parameters were used as a start and drainage area was changed to 32.89 km^2. The model fit well with these parameters, but small changes were made to maximize the model precision. Sinkhole percentage was increased to 30% which slightly increases piston flow and decreases runoff. The timing of the piston effect was pushed back by 3 hours and the timing of runoff was reduced by 5 hours. This reflects the difference in water travel times with different drainage areas. Fracture network flow and rock matrix flow parameters remained the same.

To calibrate for the April 2019 event at the South Elkhorn Gage site, calibration parameters from the SE Gage site January event were initially used. This event had less total rainfall than the January event and the runoff lasted for a longer amount of time. The timings from the Mahoney 2019 method were adjusted to flatten the curve. In this event, the piston flow had a much higher contribution than quick flow. To account for this the sinkhole percentage was adjusted to 48%. Runoff percentage from the Green ampt model was 62.5%. This makes conceptual sense because springtime will have more vegetation and less frozen ground which will decrease the amount of runoff flow. Piston flow in this event reached its maximum in only 3 hours and then recessed for 8 hours. The piston flow timing and slopes were adjusted to reflect this change. The fracture network flow (intermediate flow) was adjusted by setting $\alpha 2$ at 0.62 and $\beta 2$ at 1.046. The fracture network flow was lagged by 15 hours to reflect our concept of when intermediate flow contribution begins. The rock matrix flow (slow flow) was adjusted by setting $\alpha 3$ at 0.0085, $\beta 3$ at 1 and rock matrix porosity at 0.005. The rock matrix flow is lagged by 70 hours to reflect our concept of when slow flow contribution begins.

To calibrate for the April 2019 event at Ramsey site the same calibration parameters were used as a start and drainage area was changed to 32.89 km^2. The model fit well with these parameters, but small changes were made to maximize the model precision. Piston effect and runoff timing and calibration values were unchanged. The fracture network flow (intermediate flow) was adjusted by increasing α2 to 0.63. The rock matrix flow (slowflow) was adjusted by decreasing β3 to 0.99.

The July and October events were more difficult to model due to the unique nature of the low flow in the July event and the October event following an extended drought period. To model the July event at SE Gage, the piston effect timing needed to be shrunk to only 3 hours. The rainfall runoff curve needed to be flattened to produce more runoff for a longer amount of time. Runoff percentage for this event is the lowest at 51.9%. This may reflect the further increasing vegetative cover which will reduce runoff percolation in the summertime. It was impossible to model the flow recession in the intermediate flow due to the low magnitude of total flow, about half of that in the previous events. As was done before with rock matrix flow, fracture network flow and rock matrix flow were modeled to be straight lines with equal area above and below the line.

To model the July event at Ramsey, sinkhole percentage was increased to 29% so that there is less total flow but more flow contribution to the piston effect. Intermediate flow was relatively steeper in this event and slow flow was relatively flatter, but model parameters for fracture network and rock matrix flow from the South Elkhorn Gage calibration remained effective.

To model the October event at South Elkhorn Gage, piston flow timing needed to be reduced to one hour. Runoff timing needed to be adjusted to account for a short spike of rainfall after the initial peak. Runoff percentage for this event was highest at 69.8%. Sinkhole percentage was reduced to only 3% with piston flow being 10x smaller in magnitude than runoff. Intermediate flow, fracture network again experienced the same issue as occurred in July where the total flow was so much less than in January, it was impossible to model the flow recession with the same geologic parameters. To model fracture network flow as a gradually decreasing straight line which was of a small enough magnitude $\alpha2$ was set to 0.1 and $\beta2$ at 1.098. Rock matrix, slow flow was modeled as a straight line and $\alpha3$ was reduced to 0.008.

To model the October event at Ramsey site, piston flow and runoff timing stayed the same. Sinkhole percentage was increased back to 20%.

Figure 4.1 SUNA V2 Ultraviolet Spectroscopy Nitrate Analyzer (From Satlantic, 2011, and published in Clare, 2019)

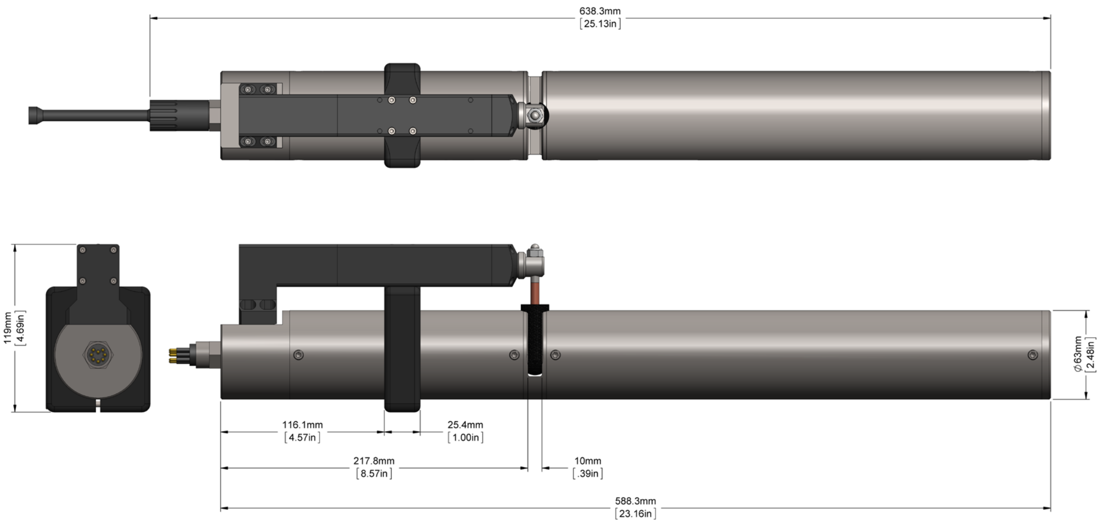

Concentration Range	**Seawater and Freshwater Calibrations (10 mm Pathlength)**	
	Sensor Specific	**Class-Based**
Best Accuracy	2 µM (0.028 mgN/L)	2.5 µM (0.035 mgN/L)
Up to 1000µM (14 mgN/L)	10 %	20 %
Up to 2000µM (28 mgN/L)	15 %	25 %
Up to 3000µM (42 mgN/L)	20 %	30 %

Figure 4.2 SE Gage sensor network diagram. Figure from Clare, 2019.

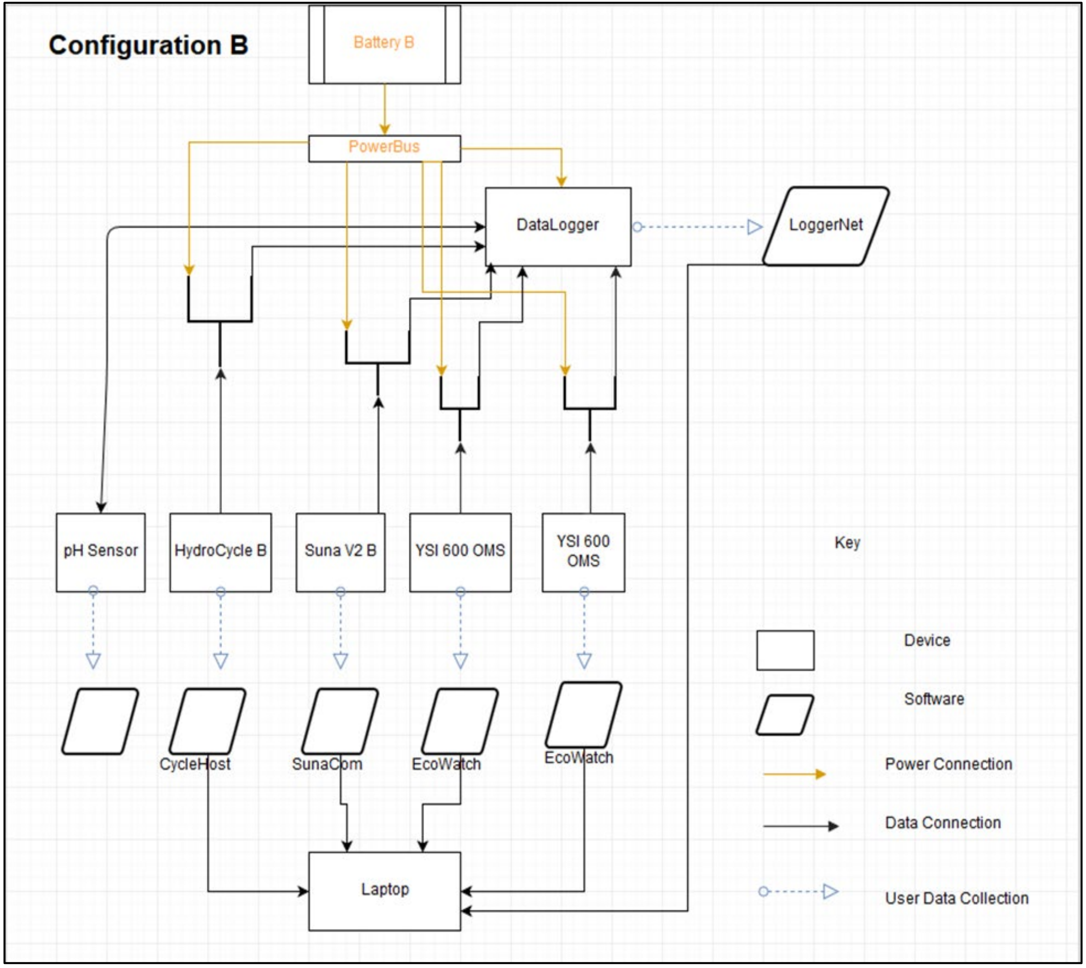

Figure 4.3 SE Gage sensor site. Figure and photographs from Clare, 2019.

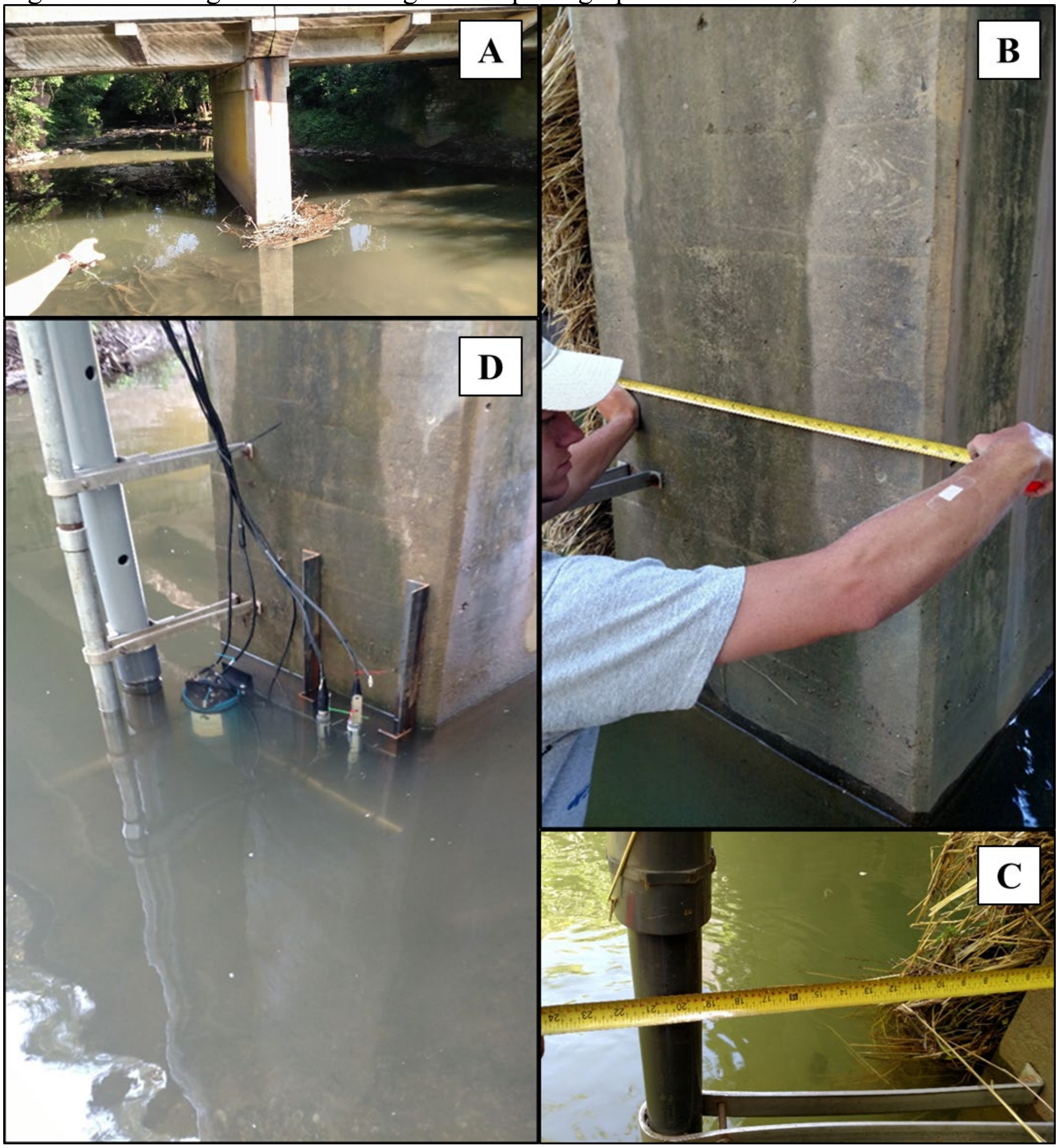

Figure 4.4 Reservoir modelling framework for water and nitrate pathways.

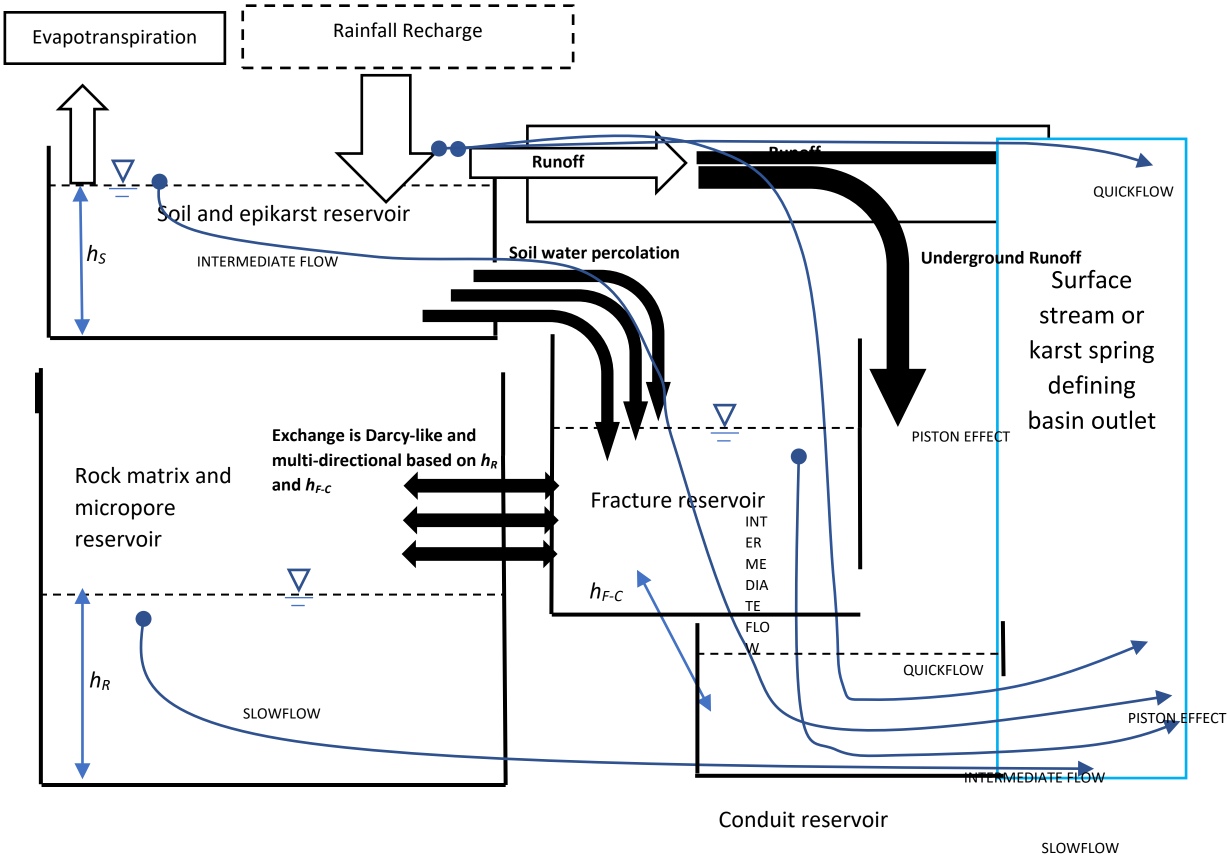

Figure 4.5 Model Inputs

Model Inputs

Symbol	Name of Variable	Value	Units
$V_{soil(i-1)}$	Volume in the soil resevoir in the prior time step	1.28×10^{15}	mm^3
R_i	Recharge of water into the soil resevoir from precipitation	n/a	mm^3
Δt	Temporal Step	0.04	day
$V_{soil(max)}$	Soil resevoir volume to activate lateral flow	3.00×10^{15}	mm^3
K_{soil}	Soil percolation coefficient	0.11	1/day
$V_{fractureNetwork(i-1)}$	Volume in the fracture network resevoir in the prior time step	1.29×10^{13}	mm^3
$V_{rockMatrix(i-1)}$	Volume in the rock matrix resevoir in the prior time step	2.58×10^{14}	mm^3
$N_{conduit}$	Nitrogen concentration in the conduit	n/a	mg/L
$N_{fractureNetwork}$	Nitrogen concentration in the fracture network (intermediate flow)	3.7	mg/L
$N_{rockMatrix}$	Nitrogen concentration in the rock matrix (slow flow)	0.5	mg/L
$N_{sinkholeRunoff}$	Nitrogen concentration of water flowing into sinkholes to the conduit (piston effect)	3.4	mg/L
$N_{streamRunoff}$	Nitrogen concentration of lateral runoff towards the stream	1	mg/L
	Mean basin Elevation	295046	mm
	Elevation at Ramsey	270662	mm
	Elevation at SE Gage	254401	mm
	Estimated height of bedrock to Ramsey (rock matrix and fracture network)	24384	mm
	Estimated height of bedrock to SE (rock matrix and fracture network)	40645	mm
	SE Drainage Area	61.64	km^3

Figure 4.6 Model Outputs

Symbol	Name of Variable	Units
$V_{soil(i)}$	Volume in the soil resevoir in the current time step	mm^3
$Q_{soilOverflow}$	Flow overtopping the soil resevoir which converts to Qrunoff	mm^3
Q_{soil}	Flow out of the soil resevoir and to the fracture network	mm^3
$V_{fractureNetwork(i)}$	Volume in the fracture network resevoir in the current time step	mm^3
$Q_{fractureNetwork}$	Flow out of the fracture network resevoir and into the conduit (intermediate flow)	mm^3
Q_{fNtoRm}	Flow from the fracture network to the rock matrix	mm^3
DV	Different between VfractureNetwork(i) and VrockMatrix(i)	n/a
$V_{rockMatrix(i)}$	Volume in the fracture network resevoir in the current time step	mm^3
Q_{RmtofN}	Flow from the rock matrix to the fracture network	mm^3
$Q_{rockMatrix}$	Flow out of the rock matrix and to the conduit (slowflow)	mm^3
$Q_{conduit}$	Flow out of the conduit resevoir and into the stream	mm^3
$Q_{sinkholeRunoff}$	Flow from runoff which is falling into the conduit resevoir through sinkholes	mm^3
Q_{runoff}	Runoff flow estimated from precipitation and runoff %	mm^3

Figure 4.7 SE Gage and Ramsey Model Calibration Parameters

Symbol	Description of Variable	Value	Units
	Silt Loam Porosity	0.486	Percentage
	Soil Height	1000	mm
	Fracture Diameter	10	mm
	Fracture Spacing	4000	mm
	Rock Matrix (Lexington limestone) porosity	0.005	Percentage
K_{stream}	Soil lateral flow coefficient	1.07	1/day
K_{soil}	Soil percolation coefficient	0.11	1/day
$\alpha 1$	Recession coefficient - quick flow	1	1/day
$\alpha 2$	Recession coefficient - intermediate flow	0.1 - 0.62	1/day
$\alpha 3$	Recession coefficient - slow flow	0.05 - 0.016	1/day
$\alpha 4$	Recession coefficient - fracture network and rock matrix exchange	0.01	1/day
$\beta 1$		0.9	
$\beta 2$		1.046-1.12	
$\beta 3$		0.99-1.1	
Runoff %	Percent of precipitation runoff based on infiltration from the Green Ampt model	34-70	
	1 - Sinkhole Percentage	0.52 - 0.97	Percentage
	Initial Soil Moisture Percentage	0.14 - 0.43	Percentage

Figure 4.8 Monthly SE Gage and Ramsey Model Calibration Parameter Adjustments

	Jan SE Gage	Jan RS	Apr SE Gage	Apr RS	July SE Gage	July RS	Oct SE Gage	Oct RS
Runoff %	66.337	66.337	62.487	62.487	51.932	51.932	69.766	69.766
1 - Sinkhole %	0.8	0.7	0.52	0.52	0.8	0.71	0.97	0.8
α2 intermediate flow	0.23	0.23	0.62	0.62	0.1	0.11	0.25	0.25
α3 slowflow	0.005	0.005	0.0085	0.0085	0.0085	0.0085	0.014	0.016
β2 intermediate flow	1.11	1.11	1.046	1.046	1.095	1.103	1.11	1.12
β3 slowflow	1	1	1	0.99	0.97	0.98	1	1.01
Piston Flow Lag (Hours)	4	0	0	0	4	0	5	0
Piston Flow Duration (Hours)	13	13	14	14	5	5	3	6
Quickflow Lag (Hours)	13	8	13	13	6	3	7	5
Quickflow Duration (Hours)	133	52	50	50	48	48	123	123

Chapter 5 Results

5.1 Nitrate and water flowrate data collection and quality assurance quality control:

The quality assurance and quality control of water quality measurements involved a number of results. First, we did a comparison of all data at a given site to see if long term trends and variability was reasonable. Second, we did site to site comparison to analyze if behavior was consistent with land use and watershed characteristics trends. Third, we analyzed data flagged by the GCE Toolbox QAQC method. Forth, we compared sensor measurements of nitrate against grab samples collected and analyzed via EPA methods.

5.1.1 All sensor data collected at the two sites:

Corrected water quality sensor measurements collected at South Elkhorn Ramsey site and South Elkhorn Gage site allowed a measure of water quality variation, seasonality, and means for the two sites (Figures 5.1 and 5.2). We present the parameters for the duration of sensor data collection.

pH varied between 7 and 9 and tended to fall between 7.5 and 8 (Fig 5.1a, 5.2a). Theoretically pH would have a loosely inverse relationship with temperature due to the equilibrium of the always occurring reaction between water and hydrogen ions plus hydroxide. At the Ramsey site, pH was relatively stable throughout 2019. At the South Elkhorn site, pH did increase over time, but it did not decrease with temperature, we believe this is a result of natural sensor drift. Once the EXO 3 begun collecting pH data the data shifted down to more reasonable levels.

Conductivity varied between 20 and 1090 μS cm^{-1} and tended to fall between 300 and 700 μS cm^{-1} (Fig 5.1b, 5.2b). Conductivity showed a correlation with temperature as well, following the same sine-like wave with peaks in August and valleys in January. This relationship is due to temperature's effect on viscosity of water. Higher temperatures result in lower viscosity, which allows for higher ionic mobility and higher conductivity.

Temperature varied between 0 °C and 26 °C and tended to fall between 8 °C and 24 °C (Fig 5.1c, 5.2c). Water temperature follows the expected seasonal trend. Temperatures fluctuate following a sine-like curve signal with minimum temperatures occurring in January and maximum temperatures occurring in August.

Dissolved oxygen varied between 0.5 and 17 mg L^{-1} and tended to fall between 6 and 14 mg L^{-1} (Fig 5.1d, 5.2d). Dissolved Oxygen mirrors the temperature signal, with maximum DO concentrations occurring in January and minimum DO concentrations occurring in August. This occurs because temperature has an inverse effect on oxygen solubility in water. Warmer water will reach 100% air saturation with less concentration of water and the opposite occurs with colder water.

Turbidity varied between 0 and 1507 ntu and tended to fall between 0 and 10 ntu (Fig 5.1e, 5.2e). Turbidity increases directly with flow rate. During storm events, water discharge into the stream disrupts in-stream sediment and brings in new eroded sediment.

This disruption leads to muddied water with high turbidity which lasts until after the storm event has ended.

Nitrate varied between 0.19 and 3.8 mg-N l^{-1} and tended to fall between 1.6 and 3.2 mg-N l^{-1} (Fig 5.1f, 5.2f). Nitrogen concentration decreases with flow rate. During storm events, water discharged into the stream from direct rainfall and overland runoff has lower nitrogen concentration than other sources. These other sources, including piston effect flow and intermediate flow will maintain or increase the nitrogen concentration right before and after the event. During non-event periods, nitrogen concentration will gradually recess due to in stream processes which take in dissolved NO_3 and output N_2 gas to the atmosphere.

Water discharge varied between 0 and 50 cms and tended to fall between 0.5 and 1 cms (Fig 5.9a, 5.9b). This signal closely mirrors the turbidity signal as higher flow is the primary influence on soil disruption in the stream. Flow changes on an event basis and does not have any outstanding seasonal trends, however in 2019 there is a concentration of events near the end of the year in winter.

5.1.2 Comparison of sensor data from the two sites:

We also compared sensor data from the two sites, to see if anomalies exist in datasets and qualitatively assess trends. We report comparison of each water quality sensor measurement at the upstream Ramsey site compared to the downstream Gage site (Figures 5.3 to 5.9).

pH at Ramsey and Gage sites for an approximately one-year period show both sites experienced similar pH values (Fig 5.3a and 5.3b). Discrepancies are likely due to differences in pH probe drift. Both pH probes experienced calibration issues throughout the collection period. Data was erratic during April and May 2019. At the Ramsey site, this resulted in anomalous low readings. At the South Elkhorn site, the average remained within expectations. Following calibration in June, both signals returned to expected levels.

Temperature at Ramsey and Gage sites for an approximately one year period showed both sites experienced similar temperature values (Fig 5.4a and 5.4b), and temperature tends to follow seasonal temperature trends for the region including winter lows and summer highs. There are no anomalies in the temperature signal.

Conductivity at Ramsey and Gage sites for an approximately one-year period show some slight differences (Fig 5.5a and 5.5b). Ramsey site conductivity was often slightly higher than at South Elkhorn. Ramsey conductivity also had a wider spread having a larger maximum and lower minimum value than at South Elkhorn. During events, Ramsey conductivity would decrease by more than South Elkhorn conductivity. South Elkhorn conductivity is lower overall and is more resistant to changes during storm events. Conductivity tends to be lowest when dominated by surface water. The Ramsey site reflects a more urban environment with more runoff and less soil and karst water. Conductivity is higher when the source is dominated by soil and karst water. The South Elkhorn Gage site represents a higher proportion of soil and karst water. This explains the differences in conductivity signal.

Turbidity at Ramsey and Gage sites for an approximately one-year period shows both sites with similar results during non-event periods (Fig 5.6a and 5.6b). During many of the storm events turbidity increases to about the same level at each site. During three events in winter 2018 and one event in winter 2019 Ramsey turbidity was three times higher than at South Elkhorn. The opposite happened during spring and summer 2019 where South Elkhorn had 2 events which produced far greater turbidity than Ramsey. One explanation for this difference is the seasonal variation in vegetation. Vegetation is dense in summertime which may reduce the potential for upland sediment runoff to the stream at Ramsey site. In the wintertime, less vegetation density will lead to more potential for sediment runoff to the stream at Ramsey site. This sediment will then deposit out of the low energy flow before reaching the South Elkhorn Gage site.

Dissolved oxygen at Ramsey and Gage sites for an approximately one-year period show both sites were similar throughout the year (Fig 5.7a and 5.7b). There was a period in March to May where both sensors produced more erratic data than usual, but the values remained around the prior average. After calibration both signals became more precise. Both signals reached a minimum in early October after the longest period without a storm event. Levels returned to and stayed at higher levels after the next event.

Nitrate concentration at Ramsey and Gage sites for an approximately one-year period remained similar at both sites (Fig 5.8a and 5.8b). During storm events, when the nitrogen concentration was diluted, Ramsey values often dipped to lower minimums than at South Elkhorn. Both signals reached a minimum value in early October after the longest period without a storm event. Levels returned to and stayed at higher levels after the next event.

Fig 5.9a and 5.9b show flow rate at Ramsey and Gage sites for an approximately one year period. Flow at the Ramsey site was calculated using a time lagged weighted drainage area method. As a result, South Elkhorn Gage flow is always higher than Ramsey.

5.1.3 Erroneous data flagged and removed during the QAQC process:

There were several sensor data points deemed as erroneous that were removed during the quality assurance quality control, or QAQC, process. Reasons for data removal and illustrations of the anomalies are included here (Figures 5.10 to 5.15).

Samples of pH data removed during the QAQC process from the Ramsey site show pH readings sometimes experienced a few short instances of abnormally high or abnormally low readings (Figure 5.10). Both instances of abnormally high readings (see Fig 5.10a,b) occurred when the sensor was first placed into the water, and pH readings quickly returned to normal. The instance of abnormally low readings (see Fig 5.10c) is unexplained but was solved once the sensor was re-calibrated. It is likely the sensor was out of calibration. At the South Elkhorn Gage site (not shown), when the YSI 6600 sensor was deployed, pH readings output as a larger number which needed to be converted to the 1-14 pH scale. Beyond this, pH at the South Elkhorn site rarely experienced any errant points.

Samples of conductivity data removed during the QAQC process showed that conductivity readings at the South Elkhorn site rarely had any issues (Figure 5.11). Conductivity readings at the Ramsey site would occasionally drift significantly away from the signal, these points were removed, and the signal quickly returned to normal. There was also an extended period of zero readings which resolved itself. One possible cause of this period of zero readings is that the sensor may have been buried or covered in dirt. This would result in the sensor being unable to take readings. At the South Elkhorn site this was a possibility, as stream sediment would pile up near the bridge bank. At Ramsey it was less likely for the sensors to be buried, but possible for the sensor to be covered with dirt.

At both the South Elkhorn, and Ramsey sites temperature and DO rarely experienced any unexpected readings, so errant data is not shown in these figures. In the case that an errant point appeared, it would be well above or below the trend and easy to see, this is not shown in the figures.

Samples of turbidity data removed and adjusted during the QAQC process show that turbidity at both sites often had very high readings (Figures 5.12 and 5.13) Turbidity also occasionally drifts below 0. Since we know this is impossible, a linear correction is applied which fixes the lowest point at 0 and raises every other point in the set by that difference. Results of this process are shown in figure 5.13.

Samples of nitrate data removed during the QAQC process show that nitrogen readings at both sites often have 0 readings (Figures 5.14 and 5.15). These readings occur immediately after the sensor has been turned back on after a battery replacement.

5.1.4 Comparison of sensor data and grab samples:

Throughout our deployment of the SUNA V2 for nitrogen readings, we collected grab samples of water that were analyzed using EPA Method 300.0. One sample was taken at each site paired with a single duplicate to help ensure data security. These samples were taken through a filtered syringe and then processed by Jason Backus in the Kentucky Geological Survey lab at the University of Kentucky. These grab samples were charted against the nitrogen readings from the SUNA V2. At both sites, there is a strong correlation between the two data sources which reinforces our confident in the sensor readings (Figures 5.16 and 5.17).

5.2 Meta-analyses of karst hydrographs, nitrate chemographs and hysteresis:

The meta-analysis section was carried out to provide further evidence that the concept model for nitrate in karst may be a reasonable approximation of karst nitrate sources and pathways beyond the study site herein. For each basin, chemograph, hydrograph and hysteresis analyses were qualitatively carried out.

The nitrate chemograph, hydrograph and hysteresis for an event at Royal Spring, Kentucky show the rising limb of the hydrograph includes the impact of a piston effect, followed nitrate dilution, then a nitrate maxima reached two days after the water discharge peak (Figure 5.18). The nitrate peak likely reflects the emergence of soil water and nitrate, or intermediate flow, at the Royal Spring sampling station. The nitrate peak is followed by nitrate recession. The hysteresis plot shows the piston effect and reflects a figure eight pattern including: clockwise hysteresis as the nitrate minima occurs after the water discharge peak is reached; then anti-clockwise hysteresis because the nitrate maxima is reached on the falling limb of the hydrograph, and the nitrate maxima exceeds the initial nitrate concentration.

The nitrate chemograph, hydrograph and hysteresis for an event at Royal Spring, Kentucky shows that as flow increases in the first moments of the event, nitrate recession stays at pre-event levels (Figure 5.18). Low concentration quick flow then dilutes stream nitrogen concentration which leads to local minimum nitrogen levels. Once the overground runoff quick flow recedes as the event dies down, high nitrogen concentration intermediate flow becomes the dominant source of water in the stream. This leads to a local maximum nitrogen concentration before the recession slope returns to pre event levels.

The nitrate chemograph, hydrograph and hysteresis for an event at South Elkhorn Ramsey, Kentucky shows that as flow increases in the first moments of the event, nitrate recession slightly increases from pre-event levels (Figure 5.19). Low concentration quick flow then dilutes stream nitrogen concentration which leads to local minimum nitrogen levels. Once the overground runoff quick flow recedes as the event dies down, high nitrogen concentration intermediate flow becomes the dominant source of water in the stream. This leads to a local maximum nitrogen concentration before the recession slope returns to pre event levels. The hydrograph and chemograph contrast with figure 5.18 in that it shows a slight daily cycle with nitrogen increasing during the evening and decreasing during the morning.

The nitrate chemograph, hydrograph and hysteresis for an event at South Elkhorn Gage, Kentucky shows that as flow increases in the first moments of the event, nitrate recession stops and levels remain constant (Figure 5.20). Low concentration quick flow then dilutes stream nitrogen concentration which leads to local minimum nitrogen levels. Once the overground runoff quick flow recedes as the event dies down, high nitrogen concentration intermediate flow becomes the dominant source of water in the stream. This leads to a local maximum nitrogen concentration before the recession slope returns to the same rate as a day before the start of the event.

The nitrate chemograph, hydrograph and hysteresis for an event at Smith Creek, Virginia show that this event does not experience a piston effect (Figure 5.21). Nitrogen levels increase rapidly at the beginning of the event due to high concentrated runoff. Runoff nitrogen concentration then reduces to levels matching other events. This flow dilutes stream nitrogen concentration which leads to local minimum nitrogen levels. Once the overground runoff quick flow recedes as the event dies down, high nitrogen concentration intermediate flow becomes the dominant source of water in the stream. This leads to a local maximum nitrogen concentration. Lower concentration slow flow, representing the ground water table, then dominates and nitrogen levels slowly recede before the next event. This stream has the highest drainage area of the six figures. This may be one explanation for the differing response of quick flow and slow flow when compared to other events.

The nitrate chemograph, hydrograph and hysteresis for an event at Difficult Run, Maryland shows that as flow increases in the first moments of the event, nitrate remains constant (Figure 5.22). Low concentration quick flow then dilutes stream nitrogen concentration which leads to local minimum nitrogen levels. Nitrate levels then rapidly increase before the end of the event. Once the overground runoff quick flow recedes as the event dies down, high nitrogen concentration intermediate flow becomes the dominant source of water in the stream and nitrogen slowly begins to increase. Finally, slow flow water becomes dominant which increases nitrogen back to pre-event levels. Levels remain constant until the next event. This system differs from other figures in that slow flow has the highest nitrogen concentration. This leads to a continued increase in levels after intermediate flow has lost its dominance.

The nitrate chemograph, hydrograph and hysteresis for an event at Big Creek, Arkansas, USA shows that this event differs from all other figures in that quick flow has the highest nitrogen levels due to nitrate runoff from a nearby concentrated animal feeding operation (Figure 5.23). As flow increases in the first moments of the event piston flow and quick flow combine as nitrogen levels reach a local maximum. Once the overground runoff quick flow recedes as the event dies down, lower nitrogen concentration intermediate flow becomes the dominant source of water in the stream. This leads to a recession slope where nitrogen levels are returning towards pre event levels. Once slow flow becomes the dominant flow path, nitrogen levels remain at a constant minimum similar to pre-event levels.

Some similarities are illustrated across the nitrate and water discharge results of the different karst basins. The similarities lead to qualitatively support the multi-porosity chemograph concept for nitrate shown in Figure 2.2.

Five out of six studies showed a near constant or slightly changing nitrate concentration throughout the initial stages of the hydrograph, which reflects the potential for the piston effect. This occurrence suggests subterranean karst conduits or caves could transport water to the basin outlet with faster transit or along with runoff due to the pressure response of the karst aquifer.

Five out of six study sites showed at least some pronounced decrease in nitrate concentration during the initial stages of the hydrograph, suggesting dilution by rainfall and a quickflow source. Nitrate concentration in rainwater tends to be less than 0.5 mgN l^{-1} and can cause dilution.

Smith Creek nitrate results showed an initial, short-lived concentrated nitrate in water followed by dilution, and Miller et al. (2017) suggests an initial concentrated quickflow occurs in some basins when easily soluble nitrate accumulates at the landscape surface and is mobilized at the beginning of an event. The Smith Creek study did not show the presence of a piston effect, which further suggests the possibility of surface sourced quickflow and thus potential for concentrated nitrate in water.

Big Creek shows an increase in nitrate concentration as opposed to dilution throughout the rising limb, peak, and initial falling limb. The nitrate increase is attributed to the swine animal feed lots in the basin, which were reported to impact nitrate transport. In this manner, the surface associated quickflow of their basin carried greater nitrate loads than the baseflow.

Five out of six studies show a nitrate concentration maximum occurring after the hydrograph peak, followed by a the nitrate chemograph recession towards a nitrate minimum. This nitrate recession likely reflects the shifting contributions of intermediate flow from soil water with water from the micropores of the rock matrix. Difficult Run shows a nitrate concentration growth, rather than recession, until a constant nitrate concentration is reached 10 days after the start of the event. The nitrate growth is suggested to occur because the groundwater-slowflow nitrate concentration in water is greater than that of the intermediate flow. Difficult Run is an urban dominated basin, which could potentially impact the distribution of nitrate sources in that basin.

Four out of six events showed a figure eight pattern; one event showed clockwise behavior; and the final event showed anti-clockwise behavior. More noticeable in the hysteresis analyses is the piston effect, which as mentioned occurs for five out of six studies.

5.3 Mass balance un-mixing modelling to quantify sources of water and nitrate:

Water and nitrate data were extracted from SE Ramsey and SE Gage datasets for January 2019, April 2019, July 2019 and October 2019 (Figure 5.24). These months of data were selected because both SE Ramsey and SE Gage had the availability of nitrate data during this time, all data fell within calendar year 2019, and each month was deemed representative of winter, spring, summer and fall seasons.

The results of the pathway separation of the unmixing model for the largest event in January 2019 at the Ramsey (a, c, e, g) and South Elkhorn Gage (b, d, f, h) show this event has the highest magnitude of the four charted events (Figure 5.25). The peak quick flow and intermediate flow values are doubled from Ramsey to South Elkhorn. Piston flow peak is 5 cms contributed per 15 minutes at both sites. SE quick flow peak is 18 cms while Ramsey quick flow peak is 9 cms. SE intermediate flow peak is 4.5 cms while Ramsey intermediate flow peak is 2 cms. This trend continued with the peak quick flow and intermediate flow nitrogen concentration where intermediate flow peaked at 6000 mg per 15 minutes at Ramsey and 12000 mg at SE. The peak piston flow and intermediate flow nitrogen concentration was 9000 mg at both sites. In this event intermediate flow quickly reaches a maximum and then gradually decreases following a negative log curve.

The results of our unmixing model for the largest event in April 2019 at the Ramsey (a, c, e, g) and South Elkhorn Gage (b, d, f, h) shows this event piston flow and piston flow nitrogen concentration had the highest overall values, and had the about the same cumulative values (Figure 5.26). This occurred at both sites. In this event, peak piston flow values at South Elkhorn Gage are doubled that of Ramsey, 10 cms and 5 cms respectively. In this event piston flow is active for the longest amount of time. This can be seen in the time series as well with the nitrate valley occurring furthest after the start of the event. Similar to the January event, peak quick flow and intermediate flow values are doubled from Ramsey to South Elkhorn SE quick flow peak is 4 cms while Ramsey quick flow peak is 2 cms. SE intermediate flow peak is 2 cms while Ramsey intermediate flow peak is 1 cms. The peak magnitude at both sites is cut in half through the progression of flow pathways as well. In this event the intermediate flow quickly increases and then decreases slowly at a linear rate.

Concerning the April nitrate mass graphs, this is the one event where the quick flow nitrogen concentration at both sites is less than intermediate flow and piston flow nitrogen concentration. In this event the intermediate flow nitrogen concentration remains constant for half of its influence before decreasing at a linear rate. Piston flow nitrogen concentration peaks at 8000 mg at Ramsey and 15000 mg at SE. Quick flow nitrogen only reaches 1000 mg at Ramsey and 3000 mg at SE. Intermediate flow nitrogen concentration gets up to at 2000 at Ramsey and 3000 at SE gage

The results of our unmixing model for the largest event in July 2019 at the Ramsey (a, c, e, g) and South Elkhorn Gage (b, d, f, h) show that this event had much less rainfall than the other three events that were un-mixed (Figure 5.27). In this event, piston flow was only slightly higher than quick flow. Ramsey piston flow peaks at 3 cms, SE Gage piston flow peaks at 5 cms. Ramsey quick flow peaks at 1 cms, Se Gage quick flow peaks at 3.5 cms, SE quick flow is a higher proportion of the piston flow levels. Ramsey intermediate flow starts at 0.25 cms and only goes down, SE intermediate flow reaches 0.35 cms and stays constant before going down. When compared to the magnitude of piston and quick flow, intermediate flow is much less significant in this event. This is likely due to the low total volume of water, most of which went to cause piston flow or overland runoff.

Concerning the July nitrate mass graphs, Ramsey piston flow nitrogen peaks at 4500 mg, SE Gage piston flow nitrogen peaks at 7500 mg. Ramsey quick flow nitrogen peaks at 1000 mg, SE Gage piston flow nitrogen peaks at 3000 mg. Intermediate flow nitrogen concentration again has low levels that remain low.

The results of our unmixing model for the largest event in October 2019 at the Ramsey (a, c, e, g) and South Elkhorn Gage (b, d, f, h) show that the October event is the most unique of the four (Figure 5.28). This event follows and extended period of low flow. Nitrogen levels before this event were the lowest of all 2019. This resulted in a positive linear relationship between nitrogen and flow. This event did not have a nitrate valley for us to determine the timing of quick flow and intermediate flow influence. Two events later in October were examined with similar flow magnitudes to estimate the quick flow nitrogen concentration. When each site reached this concentration, it is considered for this to be the turning point where quick flow influence would begin to decrease and intermediate flow influence would begin to increase. This event has the second highest magnitude of all events, almost reaching the same totals as the January event. This event also has a short increase in rainfall in the middle of the event. Ramsey piston flow reaches 7cms at max, SE has a small gap in data which would be where the max piston flow occurs, the maximum seen is 6 cms. Ramsey intermediate flow peaks at 1.4 cms, SE gage intermediate flow peaks at 2.5 cms, Ramsey intermediate flow is in line with quick flow while SE intermediate flow is less than quick flow.

Some similarities are illustrated across the nitrate and water discharge results of the different sites during the same event. In all seasons, flow at the South Elkhorn Gage site is double that at the Ramsey site. This makes sense conceptually because the SE Gage drainage area is double that of Ramsey. Figure 5.29 compares the percentage contribution from each flow path at each site during each event. In each season, the Ramsey piston contribution is much higher than at South Elkhorn. This suggests that Ramsey has a higher concentration of sinkholes, which act as the pathway for the piston effect. In January and April, the quickflow contributions are about the same at each event. In July, SE Gage has a much higher quickflow contribution. In October, Ramsey has a much higher quickflow contribution. In each case, it seems that the intermediate flow contribution is heavily reduced when the quick flow contribution is higher because less water is draining to the fractures. In January and April, the intermediate flow contributions are the same. In July and October, the intermediate flow contributions are opposite that of quickflow. In the January, April, and July events both sites have a similar slowflow contribution which suggests the slowflow pathway is resistant to seasonal changes. In October, Ramsey slowflow is double the contribution, 5% vs 10% at South Elkhorn. This may be a result of the drought conditions before the event.

Looking again at Figure 5.30 but now comparing the percentage contributions just between seasons, we can see that the piston flow contribution percentages are much higher in April and July than in January and October. January and October were the events with much more rainfall which may be causing a higher percentage of the flow to be coming from the quickflow pathway and intermediate flow pathways relative to the piston effect. Quickflow percentage contributions in January and April are almost identical. In January, the intermediate flow contribution is higher by 10% than those in April. In July and October, the quickflow contribution average is about the same, but the site with a greater contribution is flipped. In both seasons, the intermediate flow contribution is much less to account for that higher quickflow contribution, and the flipped influence at each site again is shown.

In all seasons, intermediate flow is the dominant contributor of nitrogen. This is due in part by our assumption that the intermediate flow path has the highest concentration of nitrogen. Quickflow is the second most dominant contributor even though we believe it has the second lowest nitrogen concentration, at about half of intermediate flow in most events. This is due to the high total flow. Piston flow has the most variable change in total contribution but is generally higher than slowflow. Slowflow is the lowest contributing path in all events except for October.

5.4 Reservoir modelling for nitrate transfer in the karst basins:

The reservoir model was able to effectively model all four events at each site. Figure 5.47 shows a table of root mean squared R^2 values. These numbers are a representation of, from 0 to 1, how well the model results fit to the data results from section 4.3 and 5.3. Piston flow and quick flow, which represent the stream runoff and sinkhole runoff portions of the model are consistently able to reach high R^2 values. This portion of the model has the greatest ability for calibration and the most calibration statistics. Runoff %

is directly modeled from the Green Ampt method, but sinkhole percentage could be adjusted to match the ratio of piston flow to quick flow, timing needed to be adjusted so that the shape of the runoff hydrograph matched in each case. The only low R^2 for piston or quickflow occurred in April at the SE Gage site where there was an error in data collection which resulted in 6 data points in 12 hours. The piston flow model visually matches the data piston flow.

Intermediate flow R^2 values were high in most cases. In January and in October, geologic model parameters of the fracture network allowed for a smooth curve which matched the decrease of intermediate flow over time. In July and April, a lower flow total forced the model to use lower alpha and beta values. Within this range of alpha and beta values, it was impossible to model the smooth curve. In this case, a straight line with a negative linear slope is modeled to match with the slope which begins after the intermediate flow peak. In most cases, the intermediate flow data then reduces to a steeper slope after half of the total active time. It was impossible to model this change with the current model. One possible explanation for the restriction of our ability to model a smooth curve in lower flow conditions is that the fracture network volume has properties of a cone. When there is less total volume, the surface area of the fracture network may decrease as well. In the model, changing fracture geologic parameters is the only way to reduce the flow magnitude so that alpha and beta can be chosen to create a curved line.

Slow flow, rock matrix R^2 values are high but not as much so as other flow paths. The slow flow contribution is always considerably low compared to other flow paths and often undergo sporadic changes. These small changes are ignored, since they had little effect on the overall flow and nitrogen contributions and fit a line with a tiny negative slope representing the average slowflow contribution.

In all cases the flow totals R^2 values are high. This is a result of the high correlation from piston, quickflow, and flow totals. Nitrogen totals also have high R^2 values but slightly less so than flow totals. This is due to the complexity of the transition period where piston flow, quick flow, and intermediate flow are all interacting near the same time. There were also differences when intermediate flow modeled was not adjusted to reflect the steeper slope in the second half of the event.

The model has also proven effective in mapping between sites during the same event. Calibration parameters at one site can be used to give strong results at the other site. In many cases, all six of the flow calibration parameters were identical between sites. The greatest component which needs to be changed within an event is the shape of the runoff hydrograph – the flow duration. This is done by adjusting the number of sub catchments contributing. Piston flow lag and quick flow lag also needs to be adjusted to reflect that the flow will always occur at Ramsey site a few hours before it occurs at the South Elkhorn gage site. For piston flow at the 4 events, this was a difference 4 or 5 hours for 3 events at 0 hours for the April. event. Quick flow lag was different for each event at 5, 0, 3, and 2 hours. In all four events, sinkhole percentage needed to be higher at Ramsey. We believe this reflects a higher concentration of sinkholes in the Ramsey drainage area than in the South Elkhorn drainage area. Due to this trend in piston flow changes between sites, I propose the use of 20% sinkhole land for the South Elkhorn Gage portion of the catchment and 30% sinkhole hand for the Ramsey portion of the catchment.

Alpha and beta values which control fracture network and rock matrix flows only need small adjustments between sites to maintain high correlation during the same event. These values could be left the same and the model would still return accurate results. An analysis was preformed to determine the range of acceptable values for alpha and beta. To complete this analysis, the sum of r^2 values for each event was kept above a minimum threshold of 6 (average of .75 for each event) and the correctness of each graph was visually inspected. Parameters were lowered to their minimum and raised to their maximum before the r^2 value dropped below 6 and lines were visually unreasonably far away from the calibration data. This range of alpha and beta values which give strong results at each site is shown in Figure 5.53. Following identification of an acceptable range, a single value for each parameter which best fits the validation data on average for each site is proposed for use across the model and for prediction of future events.

Using these proposed values, flow was predicted at the outlet for four new events during December, April, July, and October. These are the validation results for the calibration parameters identified. Events for each month were chosen based on similarity to the modeled event and simplicity in the rainfall distribution. For January, all the events were much smaller in magnitude or had two rainfall peaks within one event, so an event was found in December of the previous year which would have similar conditions. For each event, the Green Ampt model was run to determine the runoff percentage for each event.

SE Gage and Ramsey sinkhole percentages were set as 20% and 30% respectively. All alpha and beta parameters were used as proposed by the analysis of acceptable ranges. In December and April, the model was able to achieve a strong correlation with the USGS flow data. In July and October, the model overestimates the flow response. This is likely due to the drought conditions which occurred around that time period. The results of this new prediction are shown in Figure 5.55. R^2 analysis is preformed for each of these new events. During October and April, R^2 value is high at each site. In December of 2018, there was a secondary storm event shortly after the initial event, this caused there to be a relatively smaller number of data points compared to other events. This disparity lead to smaller R^2 values. In July, Ramsey site data is missing a majority or the data points in the rising limb of the hydrograph which is causing a smaller R^2 value, but the value is as good as the other events for the South Elkhorn Site. Overall, visually on the graph, and by examining the R^2 values, the proposed parameters and the green ampt method worked well to predict events.

I performed a sensitivity analysis on the effect of alpha 2, beta 2, alpha 3, and beta 3 on the results of flow in the fracture network and rock matrix pathways. This was done for the model results of the January event at South Elkhorn Gage and is shown in figure 5.48. Alpha 2 had a multiplicative effect on flow which is reflected in a). At higher values of alpha, the rise and fall at the beginning of the event is much more pronounced. Flow is not overly sensitive to alpha 2. Beta 2 has an exponential effect on flow. This is clearly reflected on graph c), the highest represented value of beta 2, 1.2, is so much higher than the other samples that they all appear flat on the graph. Fracture network flow is highly sensitive to beta 2. Alpha 3 has a multiplicative effect on rock matrix flow as shown in graph b). All shown options are within one magnitude. Rock matrix flow is not overly sensitive to alpha 3. Beta 3 has an exponential effect on rock matrix flow as shown in graph d). In the range of numbers around the modeled number of 1, beta 3 has less of an effect on rock matrix flow than alpha three. Rock matrix flow is not sensitive to alpha 3.

Changes in total reservoir volumes are shown in Figures 5.49, 5.50, and 5.51. The soil reservoir volumes for January + April, and July + October are graphed on different y-axes due to large differences in total volume. These differences are due to the initial reservoir moisture conditions. In January and April, the reservoirs are assumed to be 43% full before the event. In July and October, the reservoirs are assumed to be 14% full.

This choice of percentage for how full the reservoir is made by referencing soil moisture data at 5 in depth collected by the US National Climate Data Center, a sector of the National Oceanic and Atmospheric Administration at the Bluegrass airport, which is in the South Elkhorn watershed. This data shows that soil moisture increases to a maximum percentage during storm events. This percentage changes seasonally. In January soil moisture changes from 0.37 to 0.44. In April, moisture changes from 0.33 to 0.44. In July and October there are fewer total events to gauge the percentage range. In July soil moisture reaches a minimum at 0.18 then increases to 0.26. In October, due to the drought conditions soil moisture decreases to 0.1 before the event then jumps to 0.4 after the event. The reservoir fullness is assumed to be represented as the ratio of the difference between the current soil moisture percentage and the seasonal minimum percentage, and the difference of the maximum soil moisture percentage and the minimum soil moisture percentage. In January and April, the soil moisture percentage is 43% of the range before the event, while in July and October soil moisture percentage is only 14% of the range before the event.

In January and April, soil volume increases greatly at the start of the event and then slowly begins trending downwards to pre-event levels. In January, volume did return to pre event levels before the next event. In April soil volume only reduced to about 80% of the maximum before the next event. April soil volume reached double the volume of January even though January had a slightly higher total rainfall amount because much more of the water was assumed to go into the soil reservoir in that event. The recession slopes are the same because the same calibration parameters, gathered in part from Husic 2019, are used. The October and July soil reservoir volumes experience rises in volume at the start of the event as well. October volume increases greatly because there was a large amount of rainfall and the soil was devoid of water before the event. July volume only increases slightly because there was a small amount of rainfall. Both October and July have minimal recession. This is because the initial soil volumes are so low that the model calculates flow out to be minimal.

Changes in fracture network reservoir volume are shown in figure 5.50. All lines in this graph are shown the same y-axis. In January, volume increases to about 115% of the starting magnitude, and then decreases to only 15% in 8 days. In January volume decreases with the steepest slope. In April, volume increases to 120% of pre event levels, and then decreases to about 80% of the pre event levels in 5 days, before the start of the next event. The recession slope is slightly flatter than in January. In July fracture network volume barely increases due to the low rainfall amount, and then slowly decreases to about 90% of pre event levels in 4 days. In, October volume increased to 150% of pre event levels. It rose so significantly because storage was so low before the event. The volume lowered to 10% of pre-event levels in 8 days with a slope similar to that in April.

Rock Matrix reservoir storage volumes are represented in Figure 5.51. As with soil reservoir volume rock matrix reservoir volumes for January + April, and July + October are graphed on different y-axes due to large differences in total volume. All lines decrease at a negative slope at first and then begin decreasing at a stronger negative slope. At first, flow is only transferring from the rock matrix to the fracture network, but later in the event the slowflow pathway activates which increases flow out to the conduit. In all cases, the percentage change is negligible, and the recession slope is of the same magnitude.

Figure 5.1 Water quality sensor measurements at the South Elkhorn Ramsey site from 2018 to 2020. Sensor measurements included (a) pH, (b) conductivity, (c) temperature, (d) dissolved oxygen, (e) turbidity, (f) nitrate, and (g) water discharge.

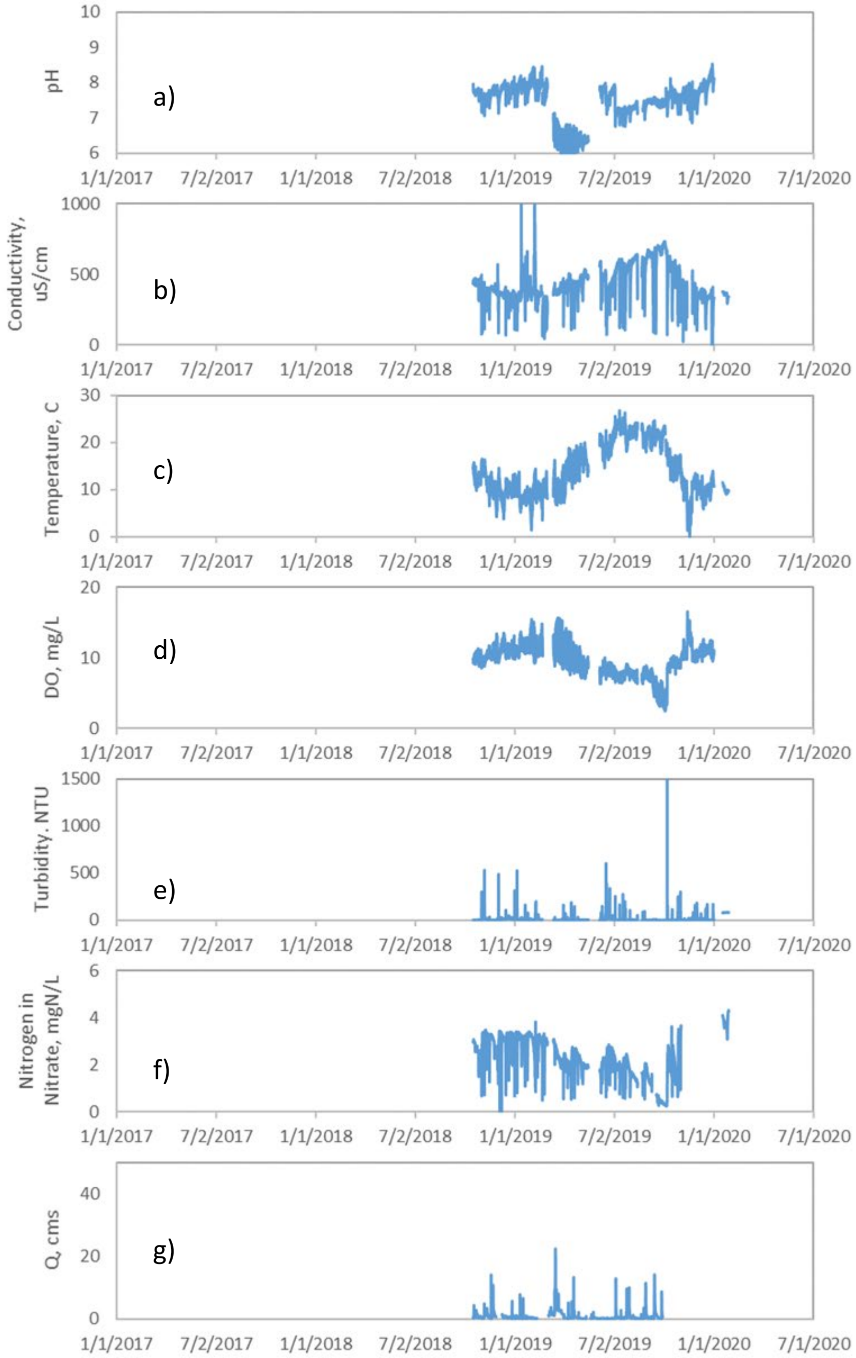

Figure 5.2 Water quality sensor measurements at the South Elkhorn Gage site from 2017 to 2020. Sensor measurements included (a) pH, (b) conductivity, (c) temperature, (d) dissolved oxygen, (e) turbidity, (f) nitrate, and (g) water discharge. In multicolored charts, the blue line reflects data collected by the YSI 6600 sonde while the orange line reflects data collected by the YSI exo3 sonde.

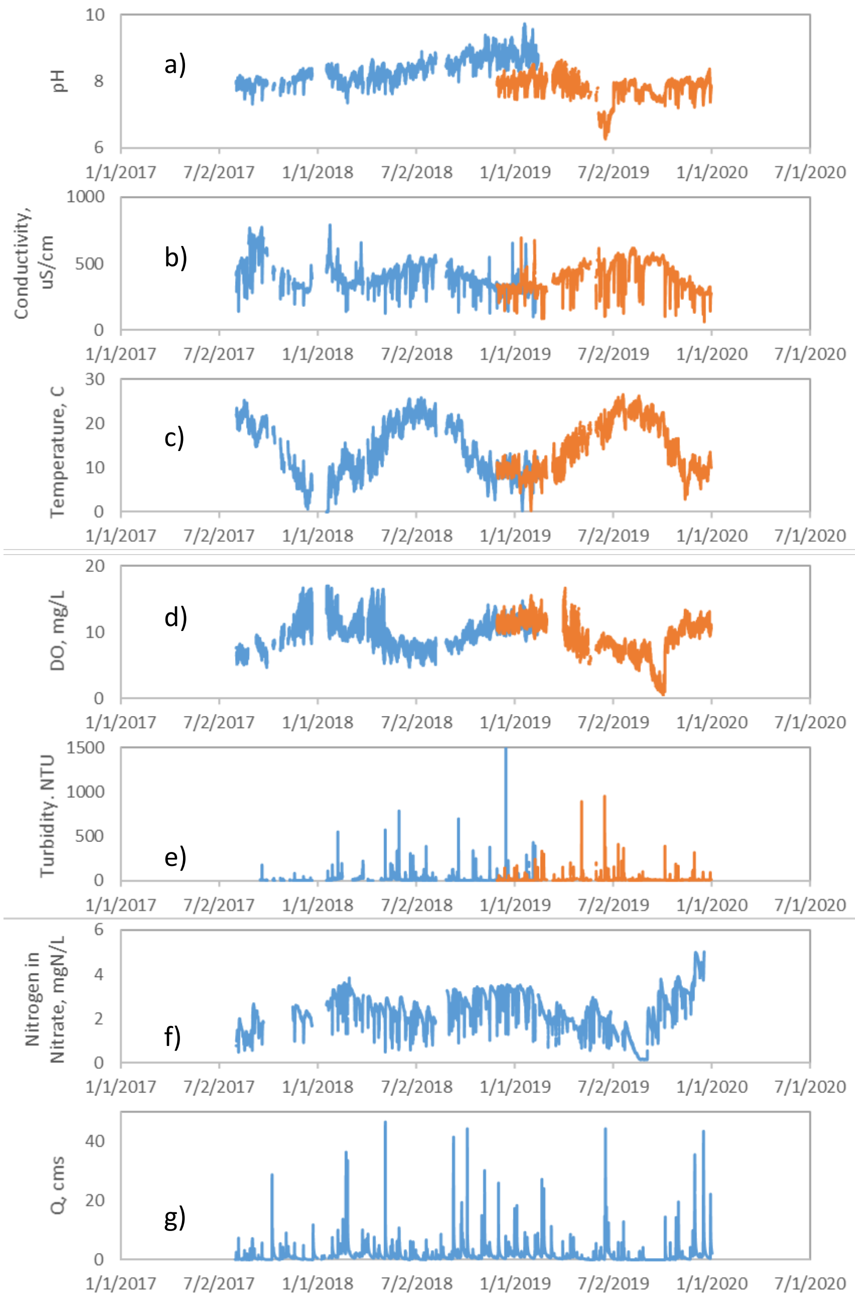

Figure 5.3 pH sensor measurements at (a) the South Elkhorn Ramsey site (blue) and the (b) South Elkhorn Gage site (orange) from October 2018 to 2019.

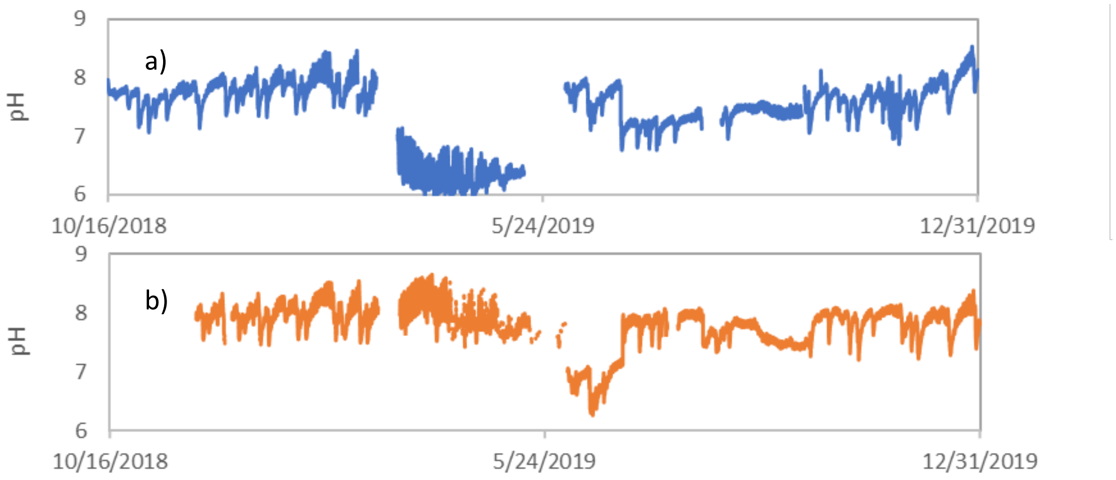

Figure 5.4 Temperature sensor measurements at (a) the South Elkhorn Ramsey site (blue) and the (b) South Elkhorn Gage site (orange) from October 2018 to December 2019

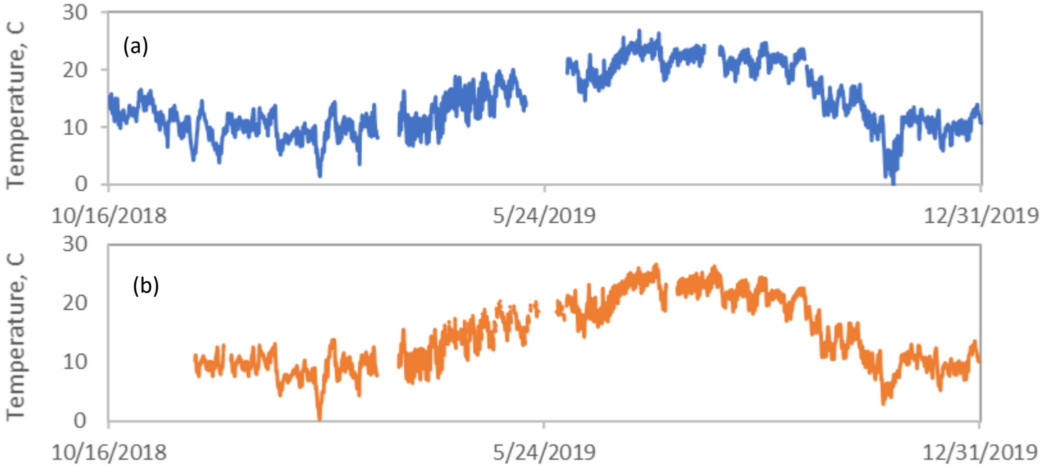

Figure 5.5 Conductivity sensor measurements at (a) the South Elkhorn Ramsey site (blue) and the (b) South Elkhorn Gage site (orange) from October 2018 to December 2019 .

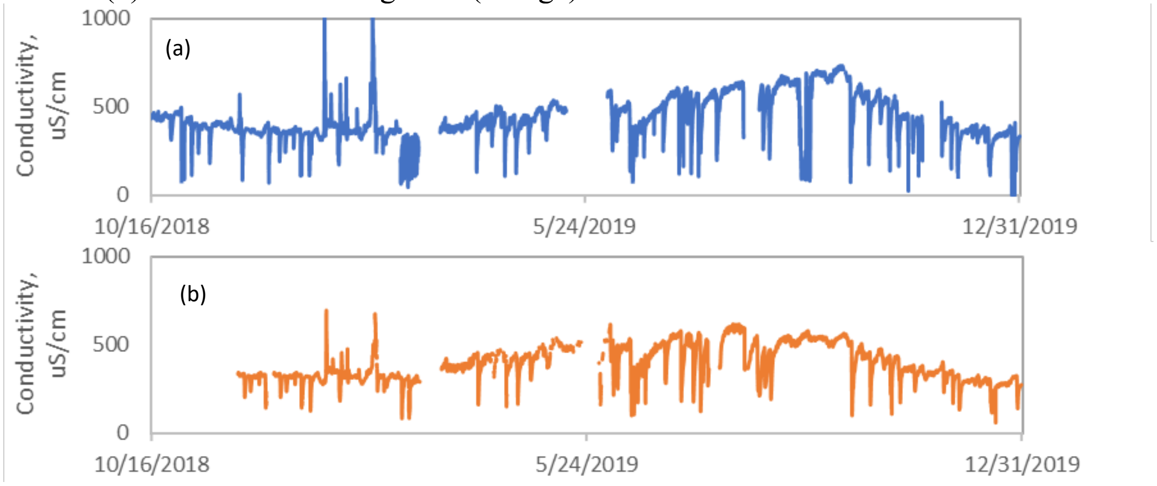

Figure 5.6 Turbidity sensor measurements at (a) the South Elkhorn Ramsey site (blue) and the (b) South Elkhorn Gage site (orange) from October 2018 to December 2019.

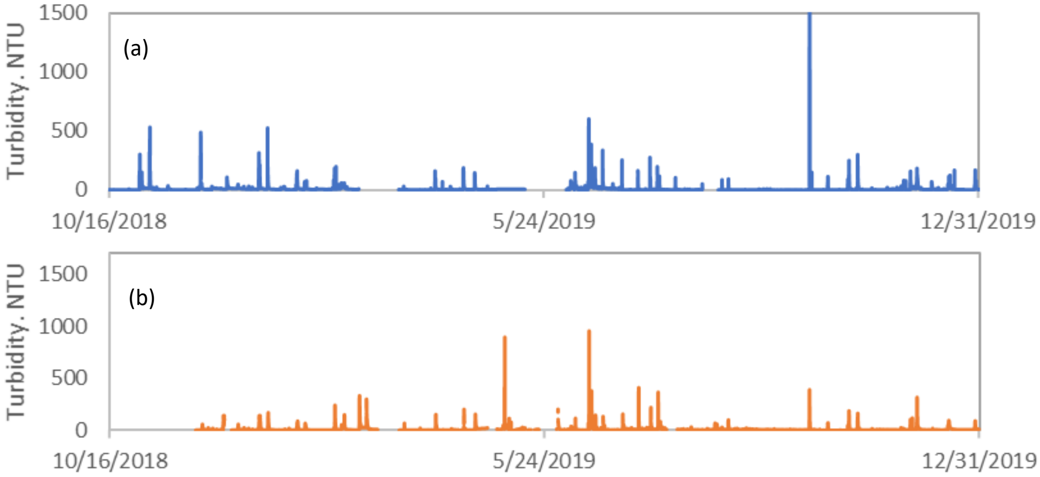

Figure 5.7 Dissolved oxygen sensor measurements at (a) the South Elkhorn Ramsey site (blue) and the (b) South Elkhorn Gage site (orange) from October 2018 to December 2019.

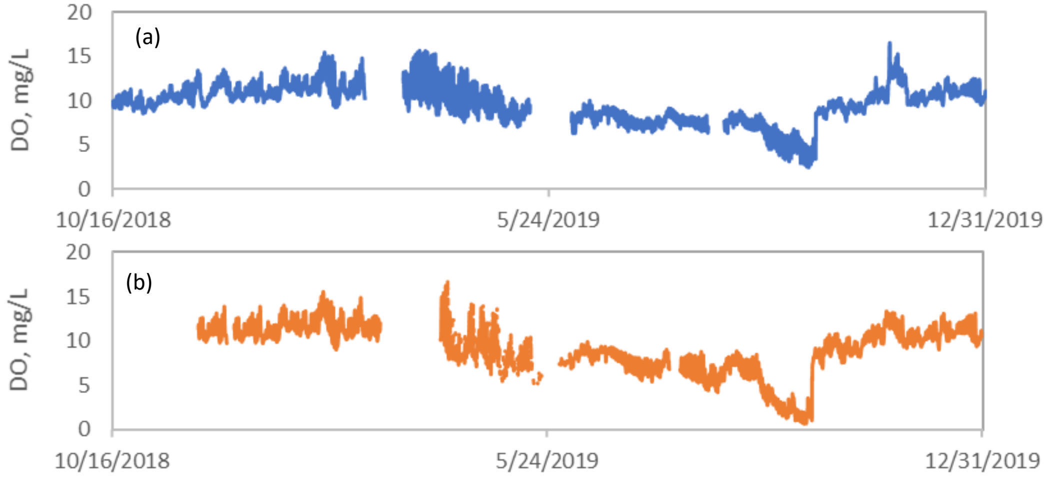

Figure 5.8 Nitrate sensor measurements at (a) the South Elkhorn Ramsey site (blue) and the (b) South Elkhorn Gage site (orange) from October 2018 to December 2019.

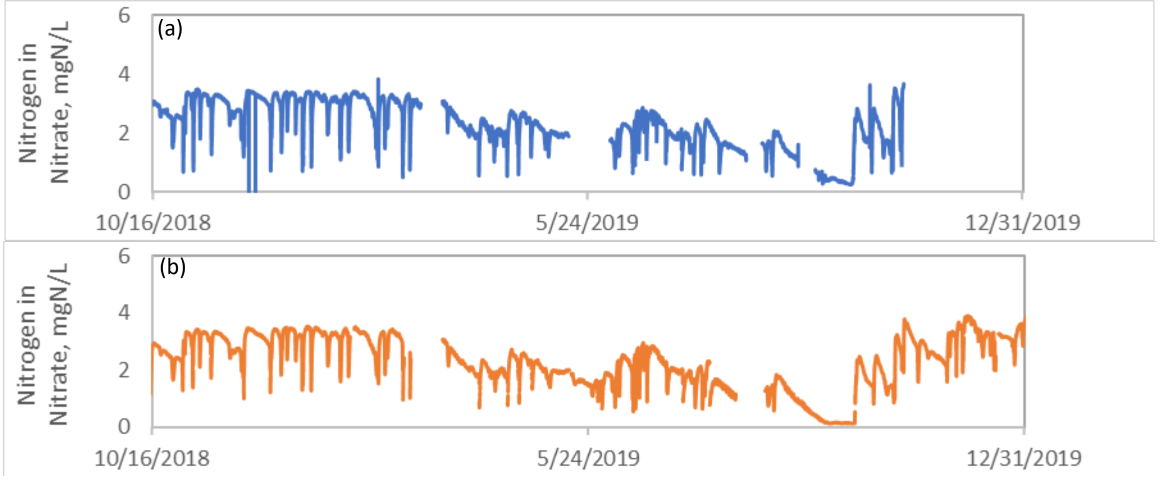

Figure 5.9 Water discharge measured at the USGS Gage station 03289000 South Elkhorn Creek at Fort Springs Kentucky then converted by time lagged weighted drainage area method at (a) the South Elkhorn Ramsey site (blue) and the (b) South Elkhorn Gage site (orange)

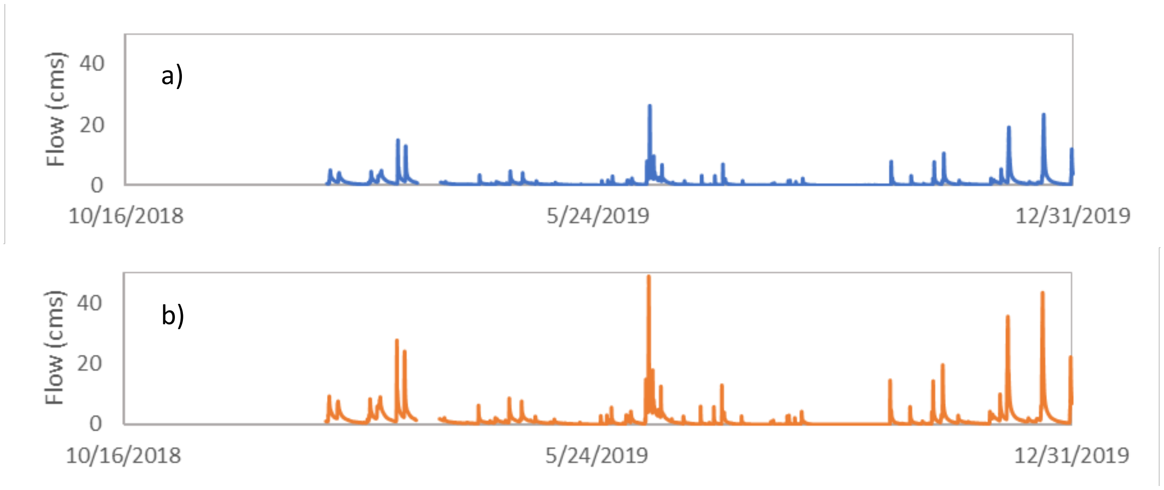

Figure 5.10 Samples of pH data removal of pH at the Ramsey site.

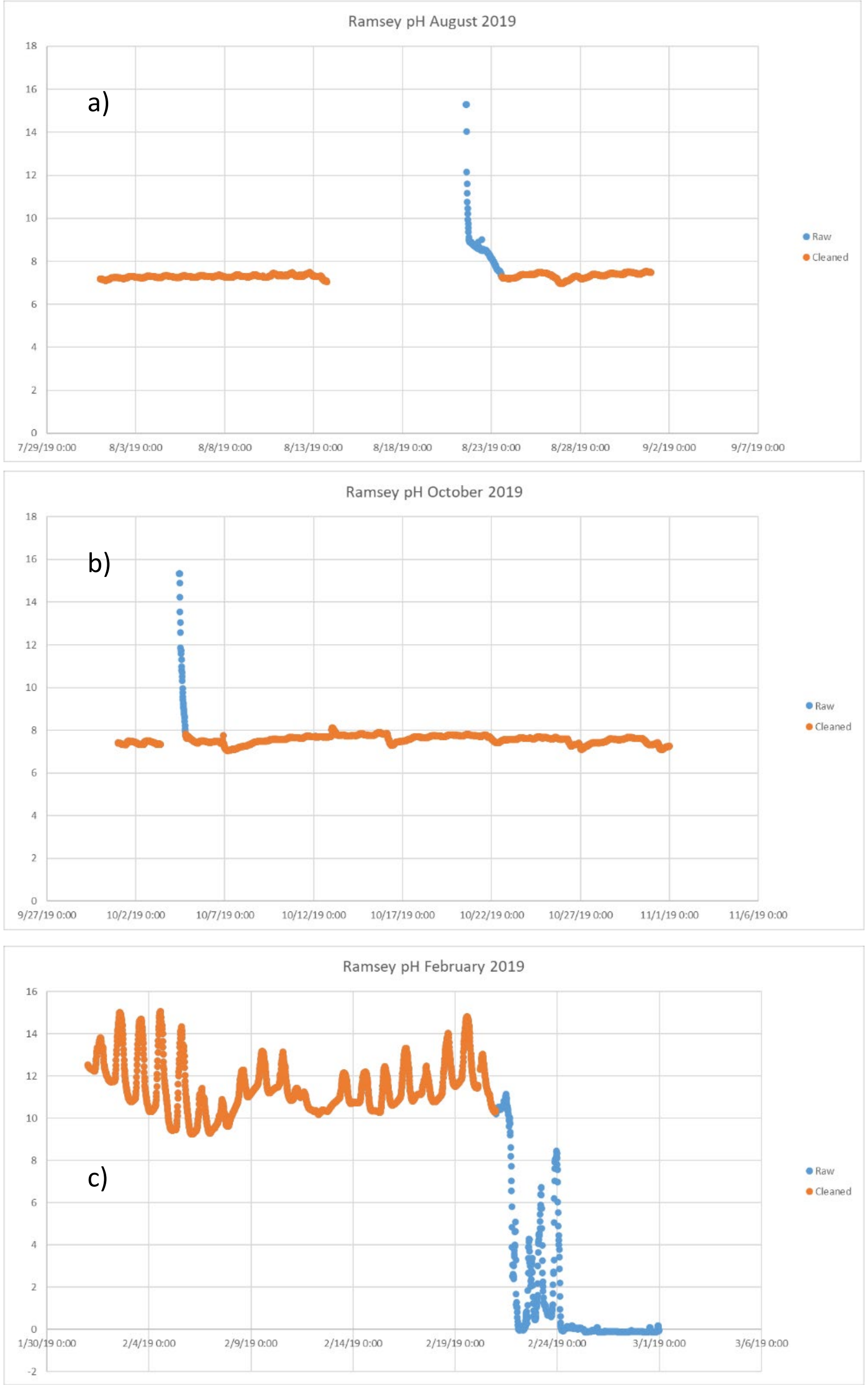

Figure 5.11 Samples of conductivity data removal at the Ramsey site.

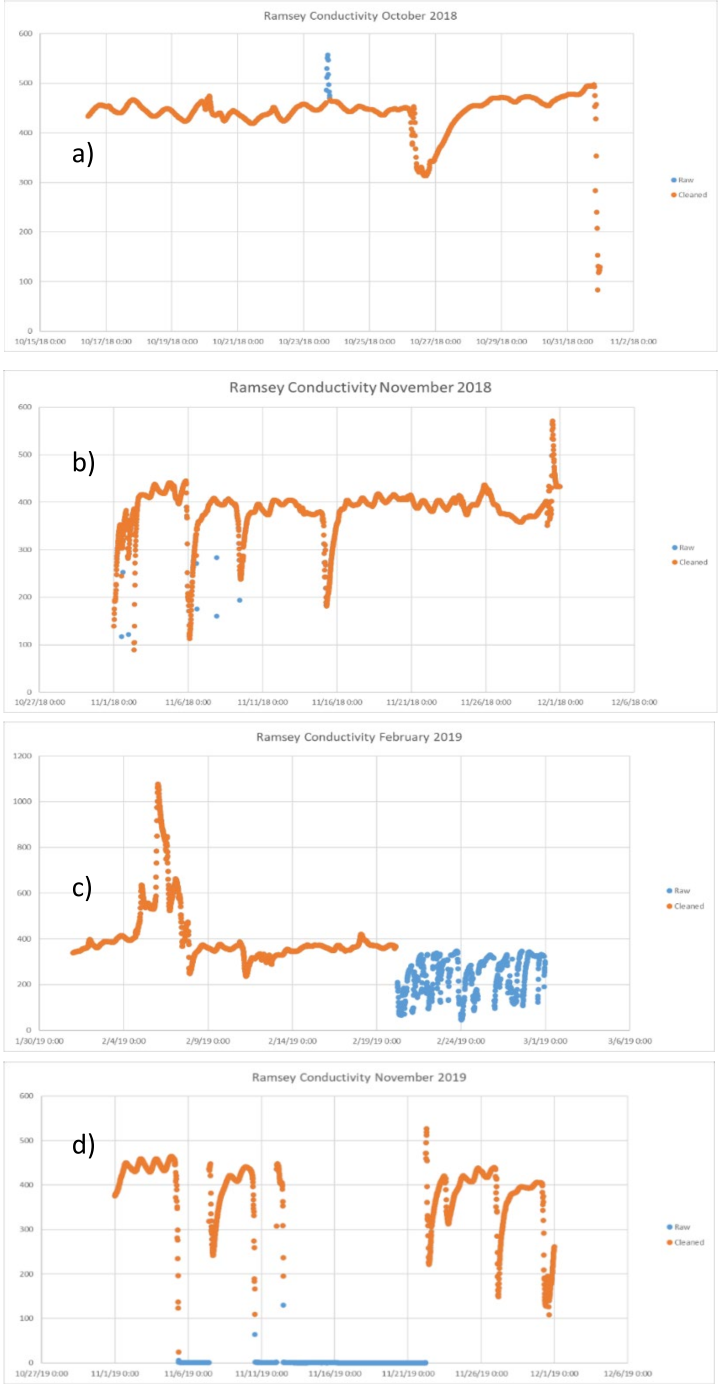

Figure 5.12 Samples of turbidity data removal at the South Elkhorn Gage and Ramsey sites.

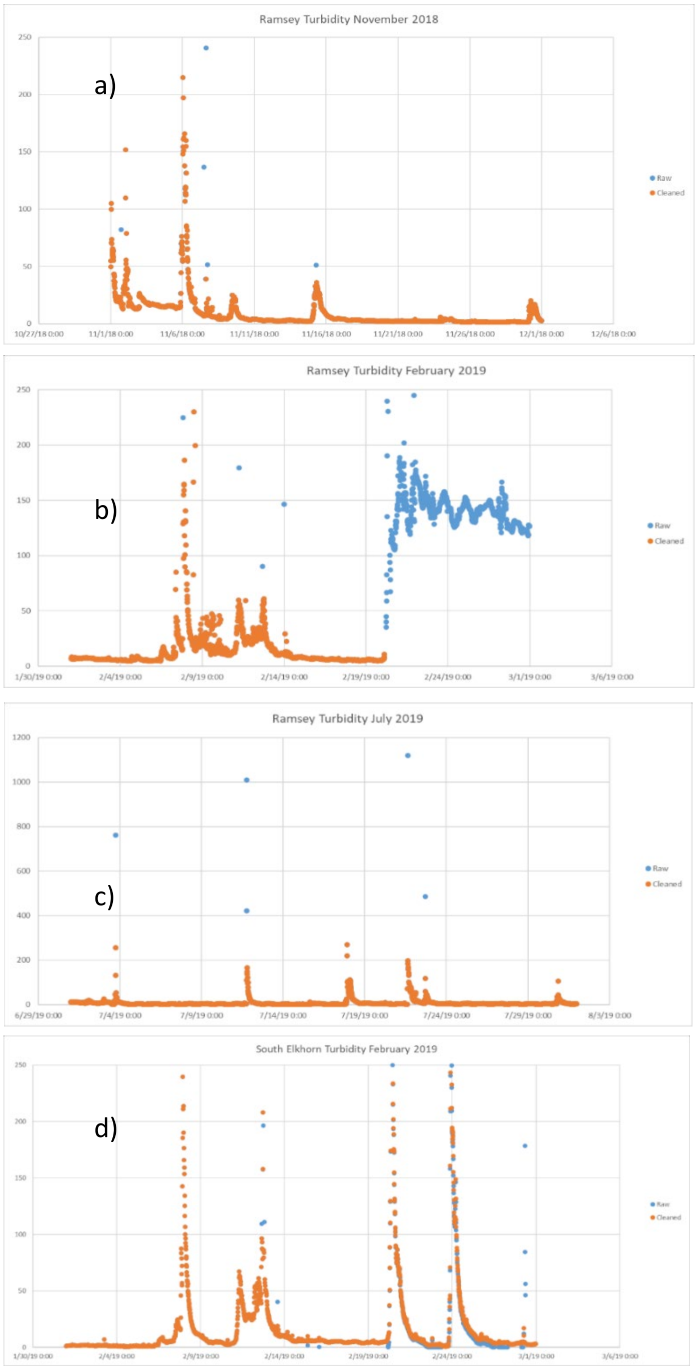

Figure 5.13 Samples of linearly adjusted turbidity data at the South Elkhorn Gage and Ramsey sites.

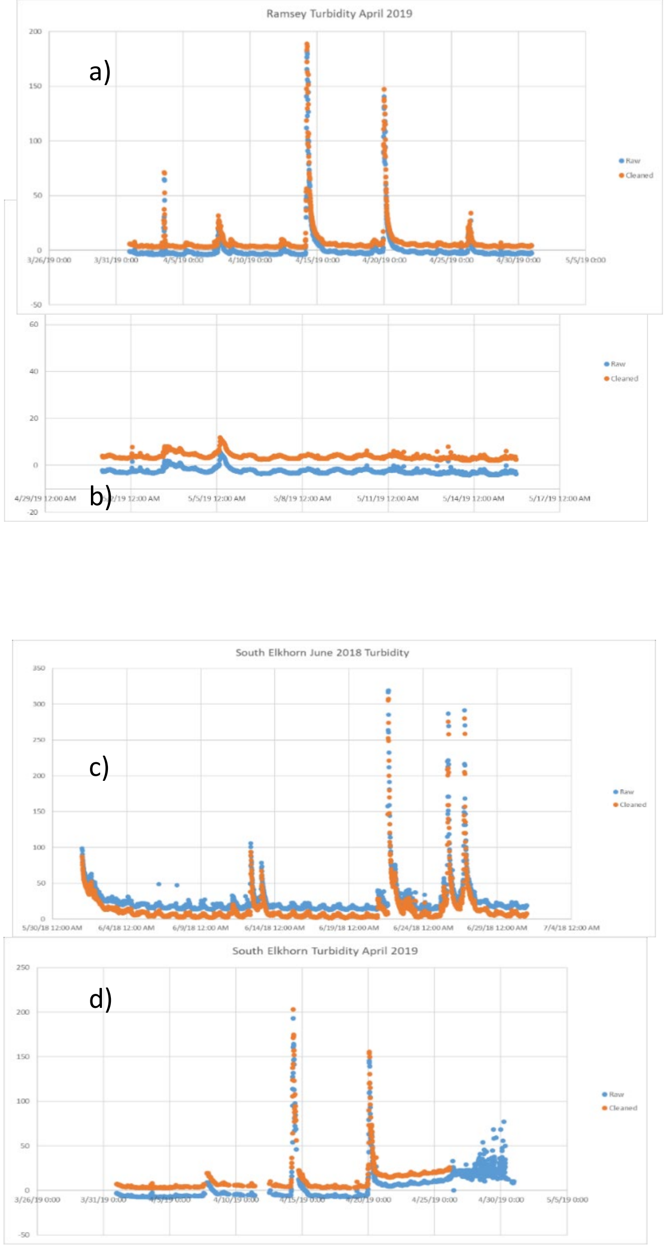

Figure 5.14 Samples of nitrate data removal at the Ramsey site.

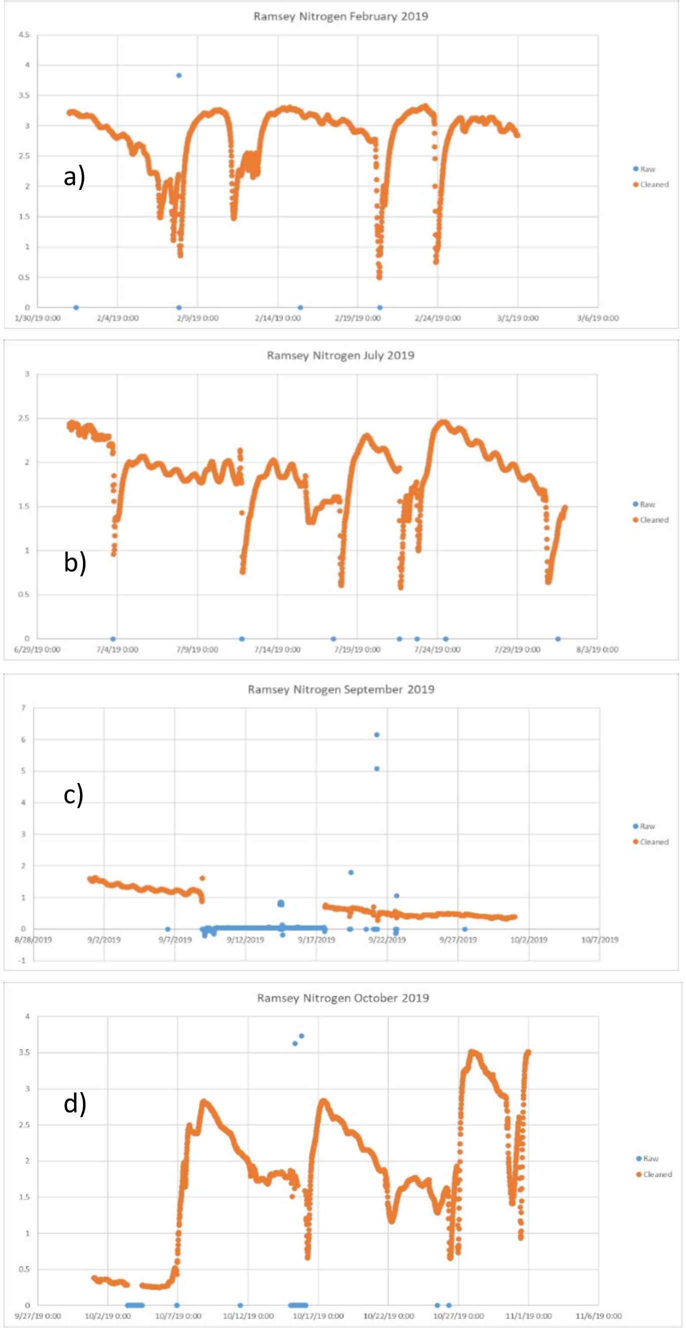

Figure 5.15 Samples of nitrate data removal at the South Elkhorn Gage site.

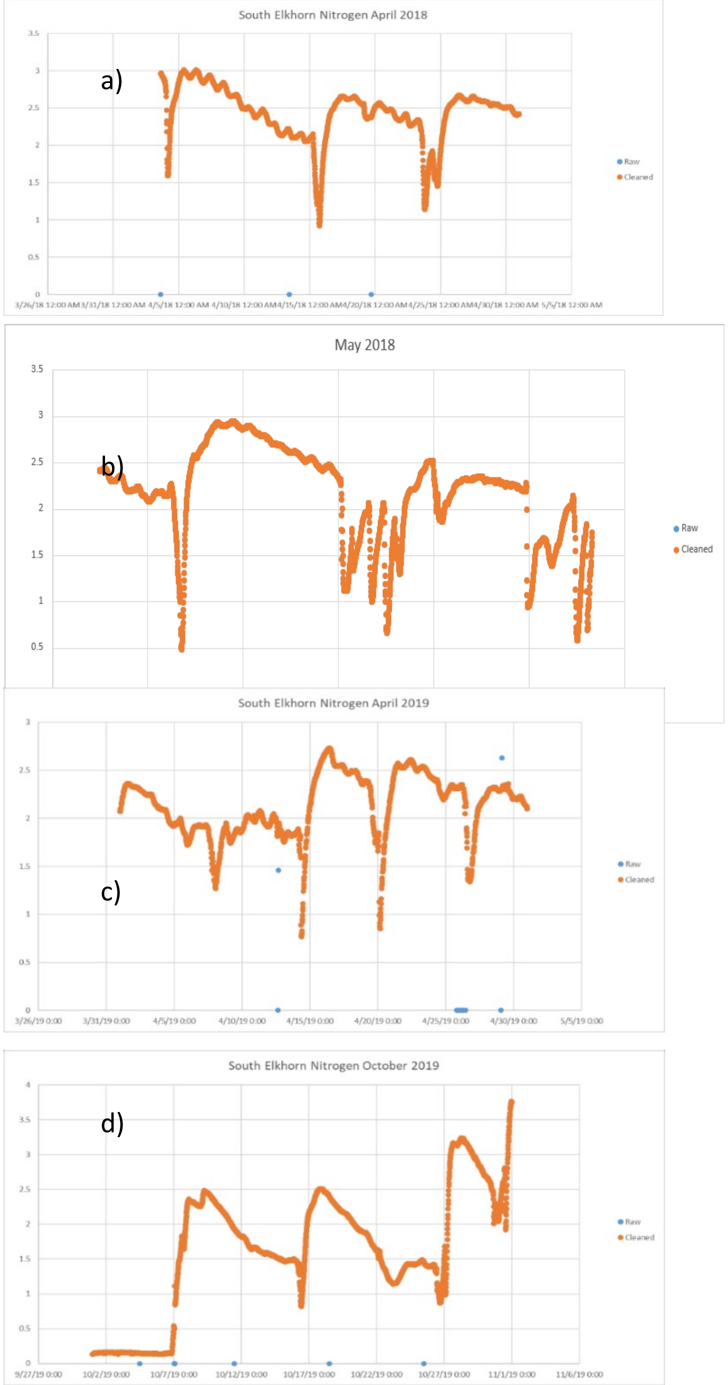

Figure 5.16 Comparison of grab samples and sensor measurements at (a) South Elkhorn Ramsey site and (b) South Elkhorn Gage site.

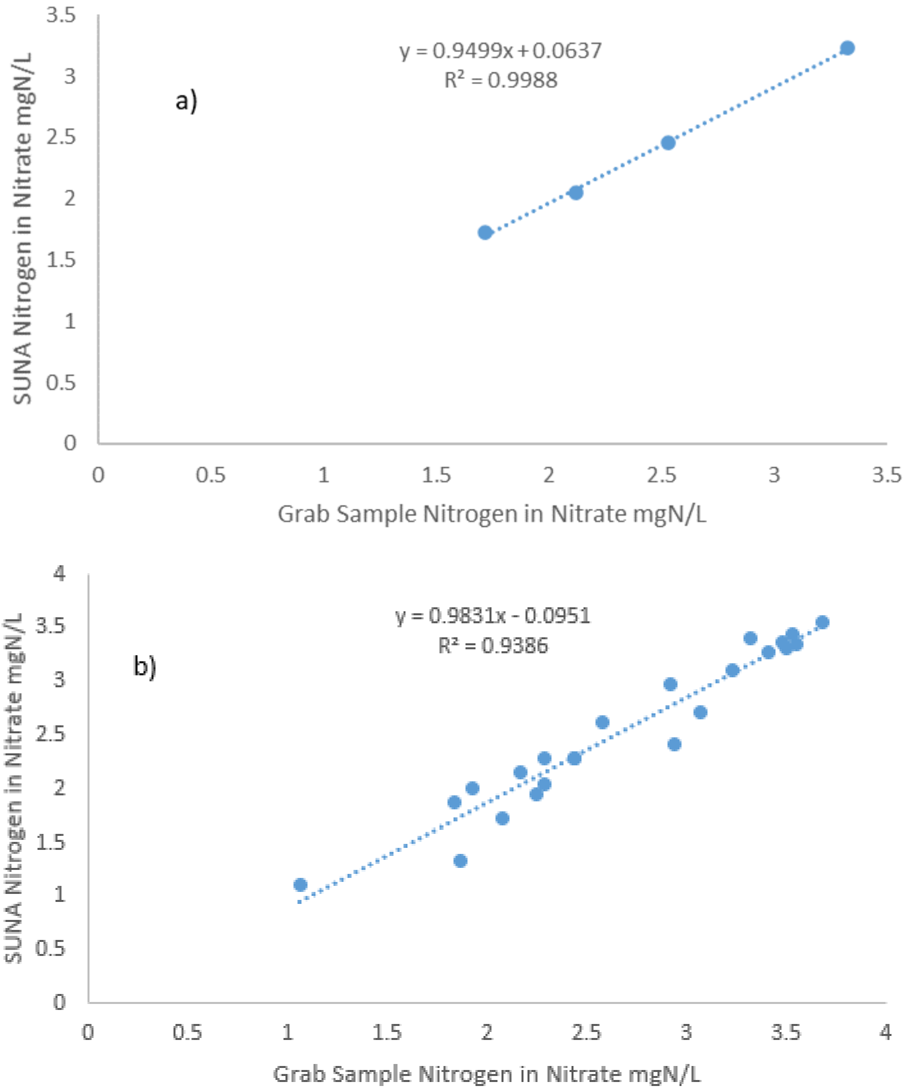

Figure 5.17 Comparison of grab samples and sensor measurements at (a) South Elkhorn Ramsey site and (b) South Elkhorn Gage site.

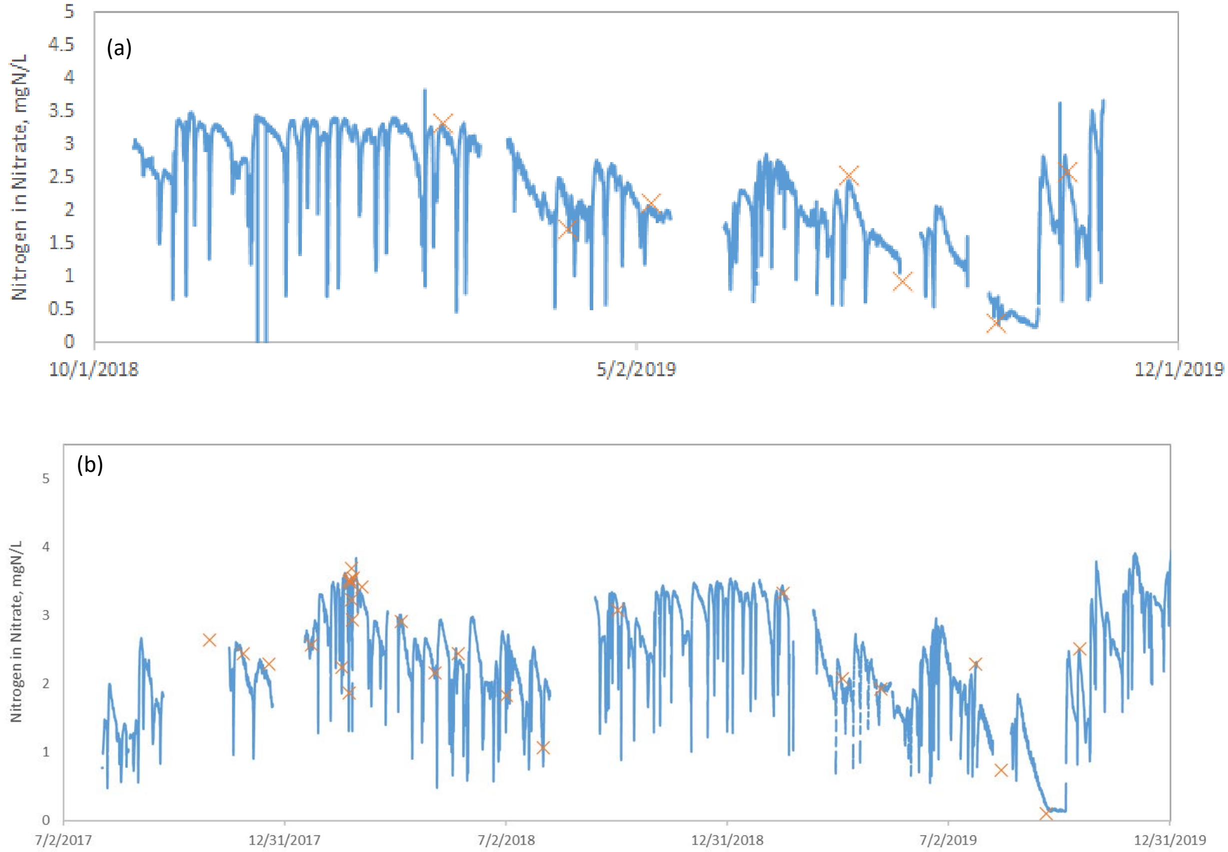

Figure 5.18 Nitrate chemograph, hydrograph and hysteresis for an event at Royal Spring, Kentucky.

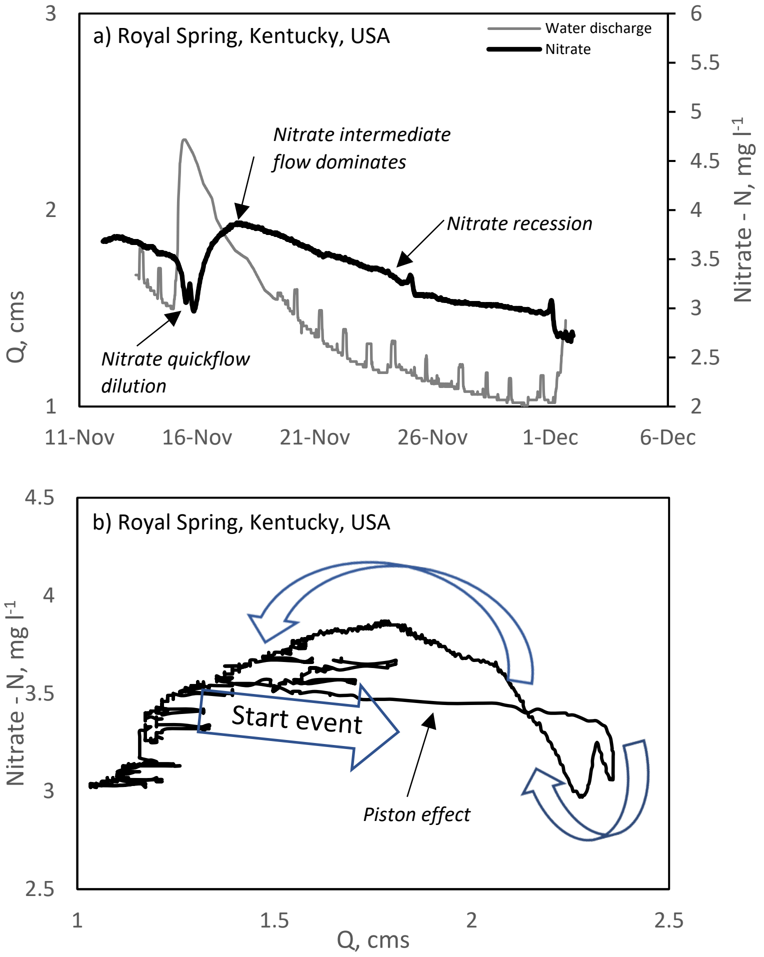

Figure 5.19 Nitrate chemograph, hydrograph and hysteresis for an event at South Elkhorn Ramsey, Kentucky.

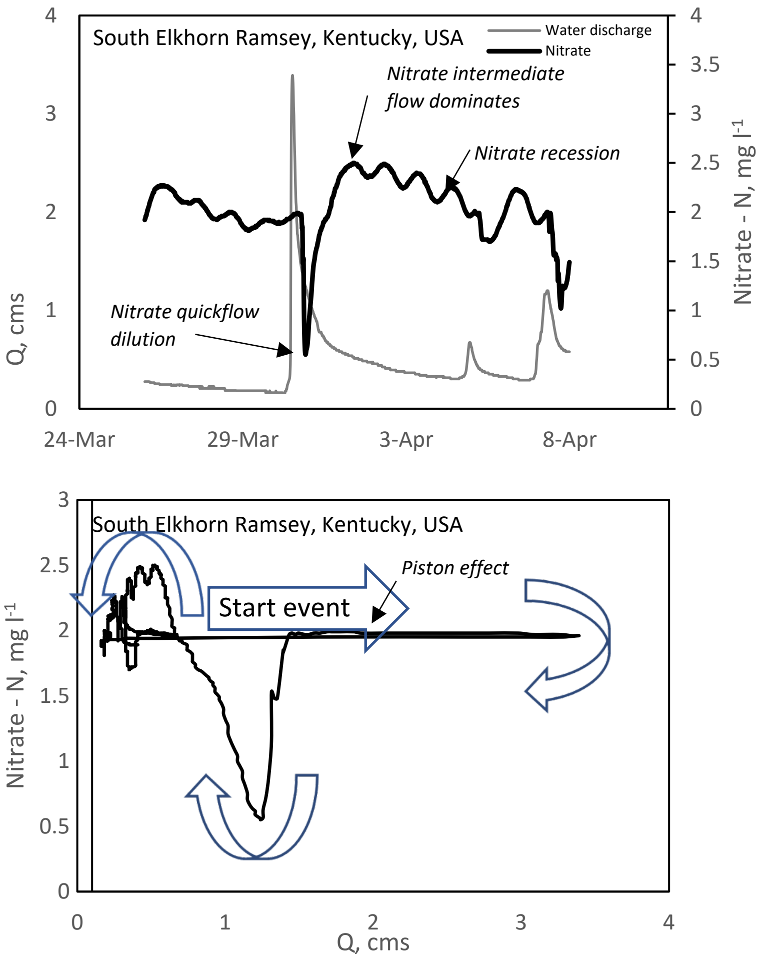

Figure 5.20 Nitrate chemograph, hydrograph and hysteresis for an event at South Elkhorn Gage, Kentucky.

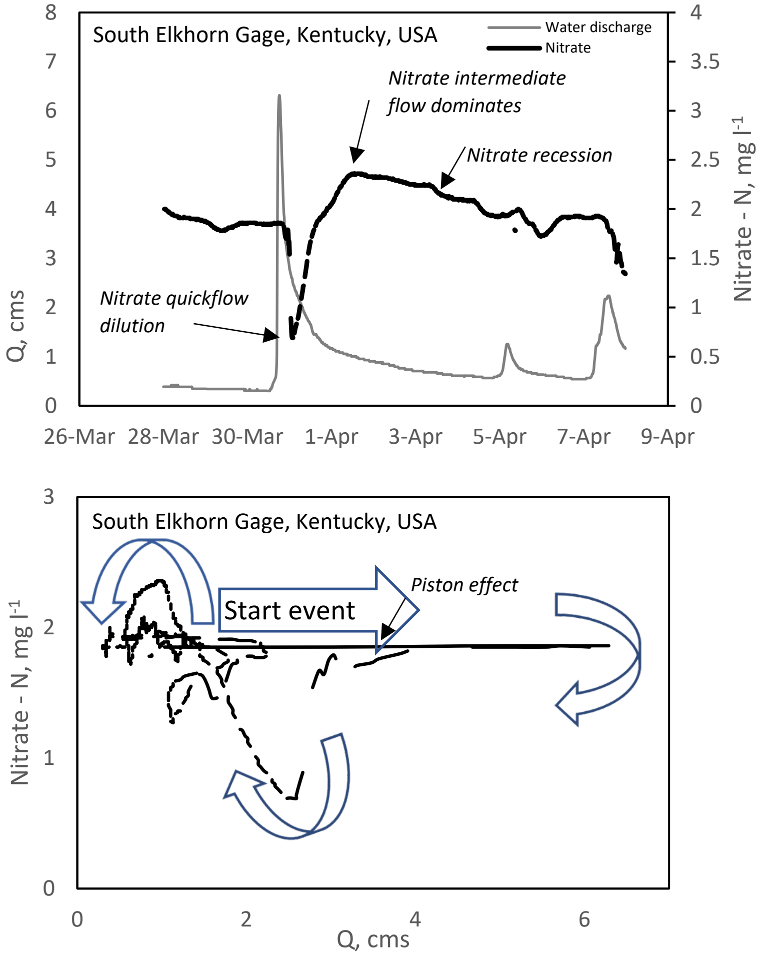

Figure 5.21 Nitrate chemograph, hydrograph and hysteresis for an event at Smith Creek, Virginia.

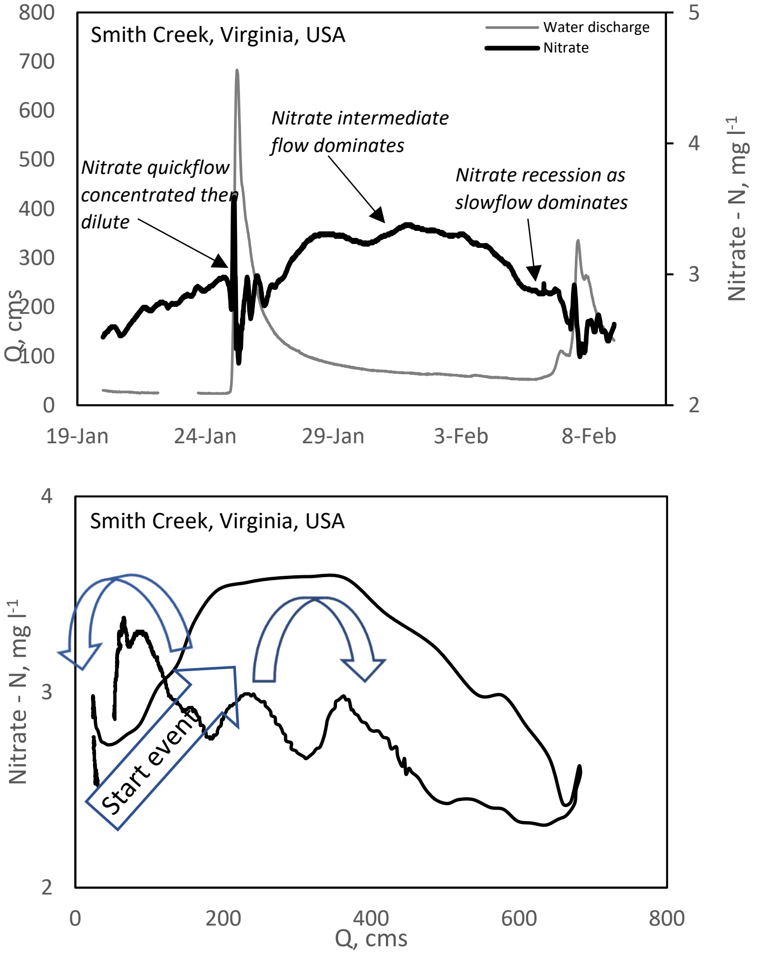

Figure 5.22 Nitrate chemograph, hydrograph and hysteresis for an event at Difficult Run, Maryland.

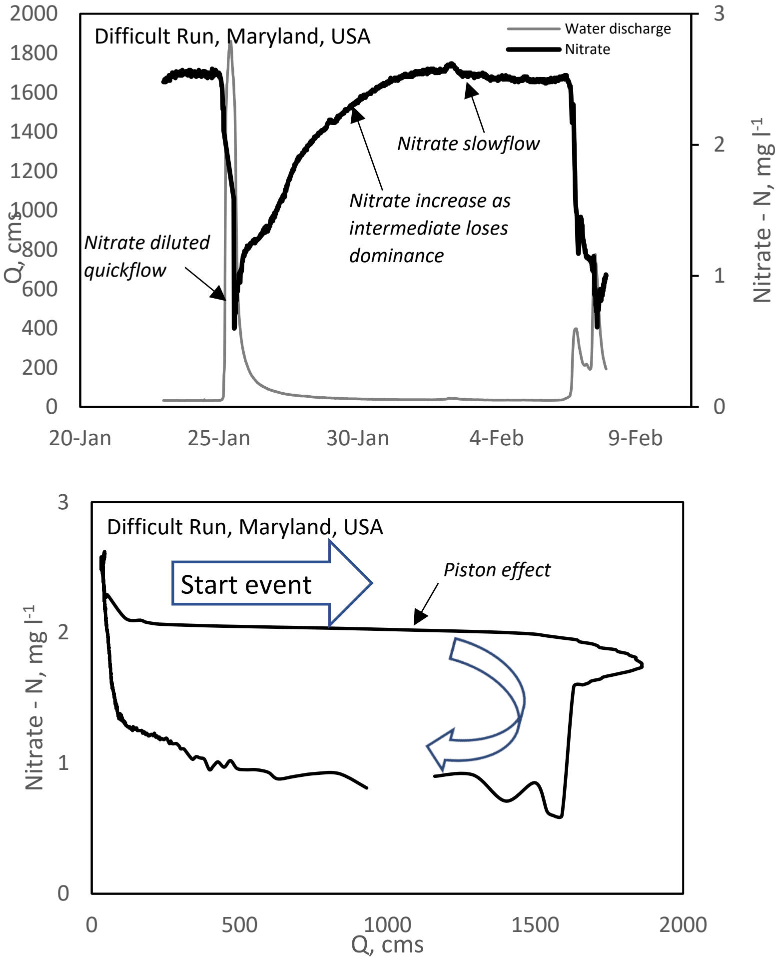

Figure 5.23 Nitrate chemograph, hydrograph and hysteresis for an event at Big Creek, Arkansas, USA.

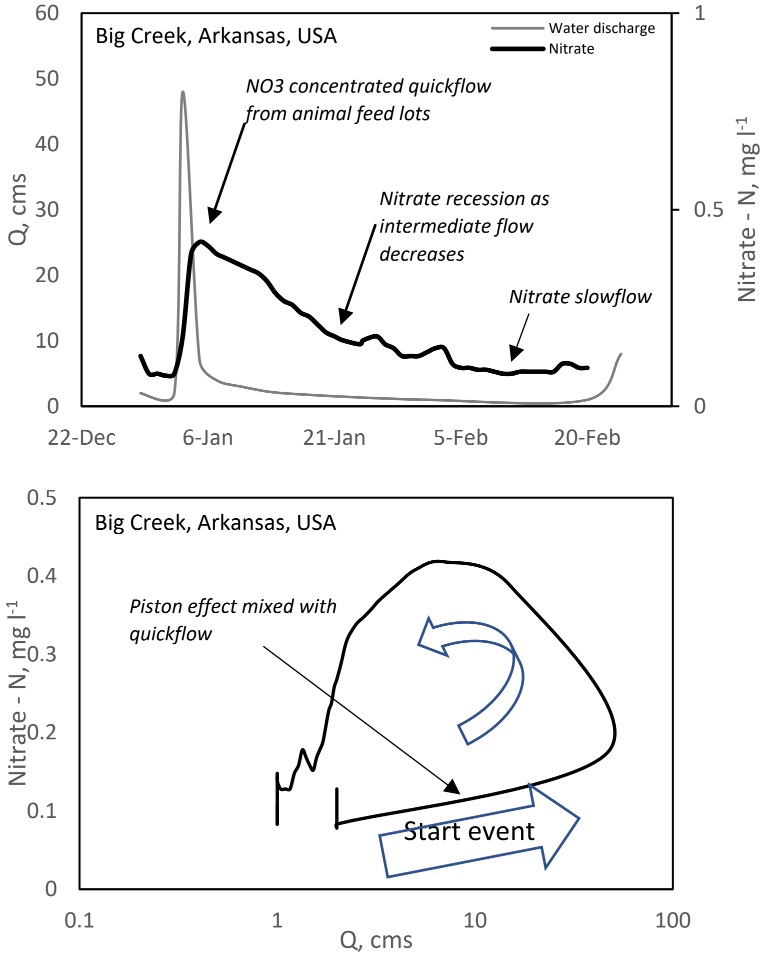

Figure 5.24 Figure of 2019 Time Series for Ramsey a), and South Elkhorn b), With Locations of the Four Focused Events

a)

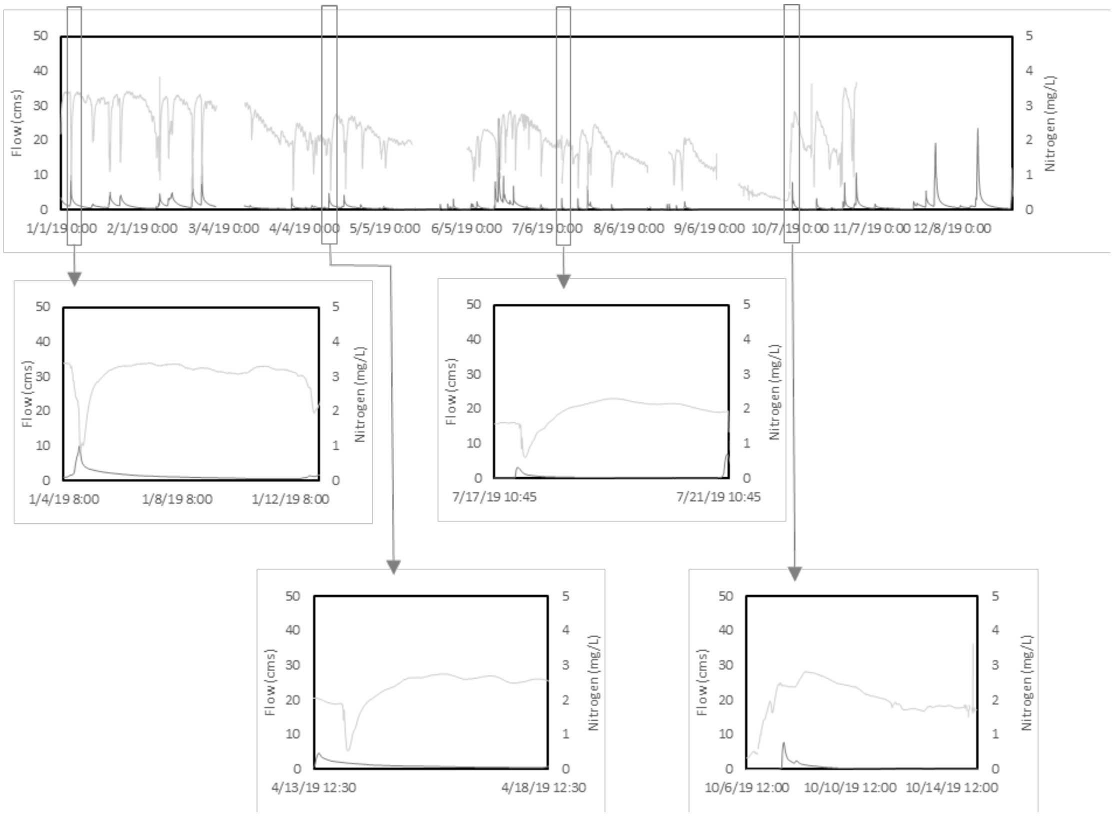

b)

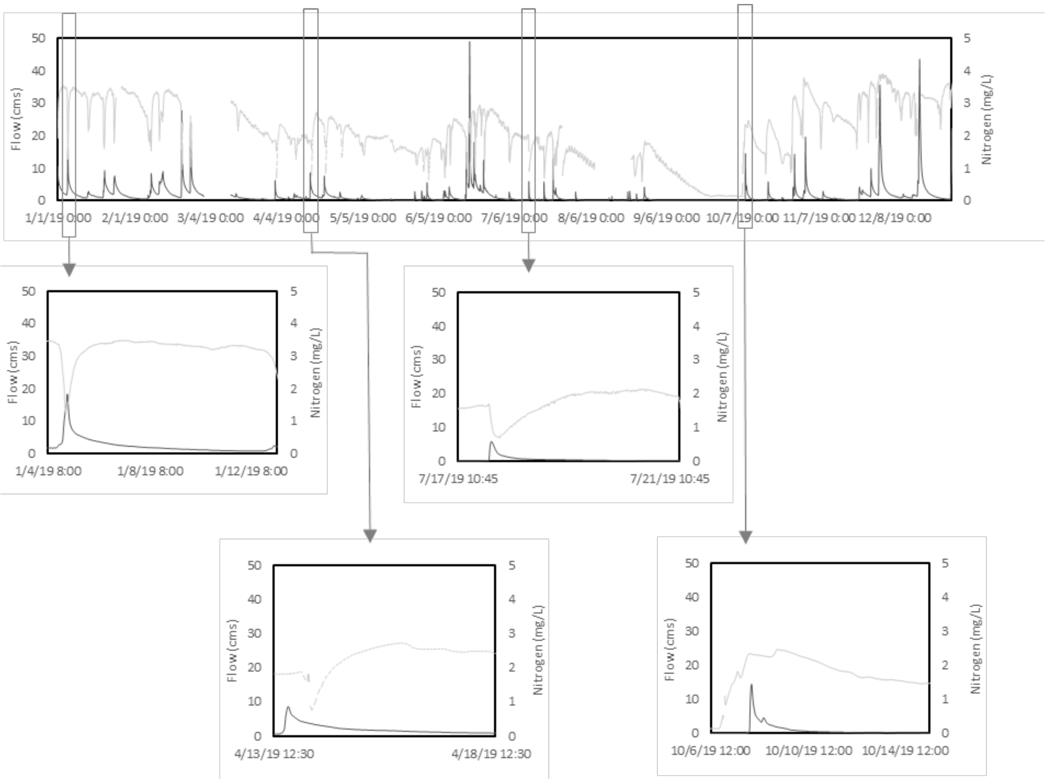

Flow (cms)
Nitrogen (mg/L)
50
40
30
20
10
0
5
4
3
2
1
0
1/1/19 0:00
2/1/19 0:00
3/4/19 0:00
4/4/19 0:00
5/5/19 0:00
6/5/19 0:00
7/6/19 0:00
8/6/19 0:00
9/6/19 0:00
10/7/19 0:00
11/7/19 0:00
12/8/19 0:00
1/4/19 8:00
1/8/19 8:00
1/12/19 8:00
7/17/19 10:45
7/21/19 10:45
4/13/19 12:30
4/18/19 12:30
10/6/19 12:00
10/10/19 12:00
10/14/19 12:00

Figure 5.25 January Event Flow and Nitrate Unmixing where the left column shows Ramsey site and the right column shows South Elkhorn Gage Site. a) and b) show flow in L, c) and d) show nitrate in mg, e) and f) show cumulative flow in Liters, g) and h) show cumulative nitrogen in mg

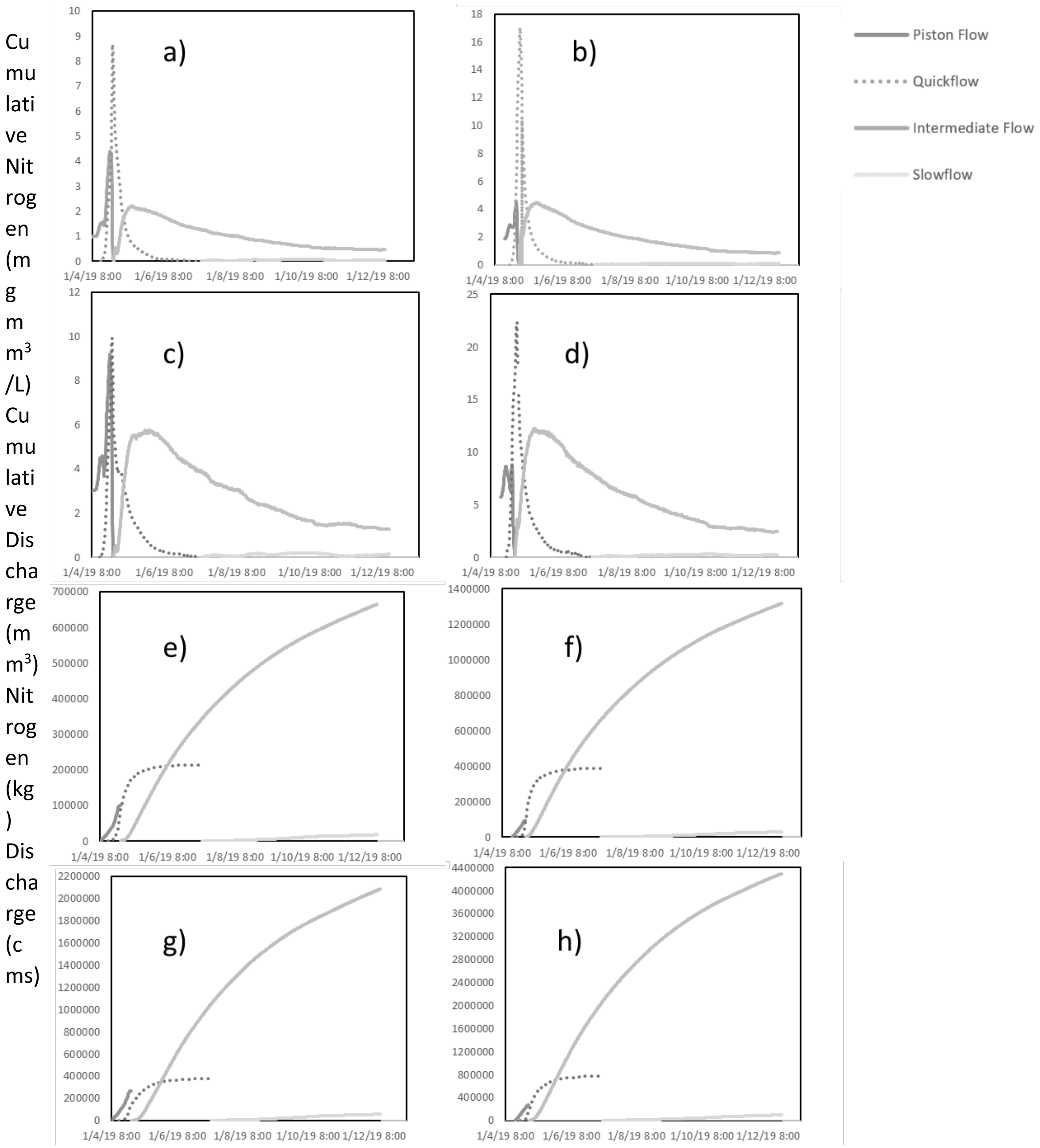

Figure 5.26 April Event Flow and Nitrate Unmixing where the left column shows Ramsey site and the right column shows South Elkhorn Gage Site. a) and b) show flow in L, c) and d) show nitrate in mg, e) and f) show cumulative flow in Liters, g) and h) show cumulative nitrogen in mg

Cumulative Nitrogen (mg m m^3/L) Cumulative Discharge (m m^3) Nitrogen (kg) Discharge (cms)

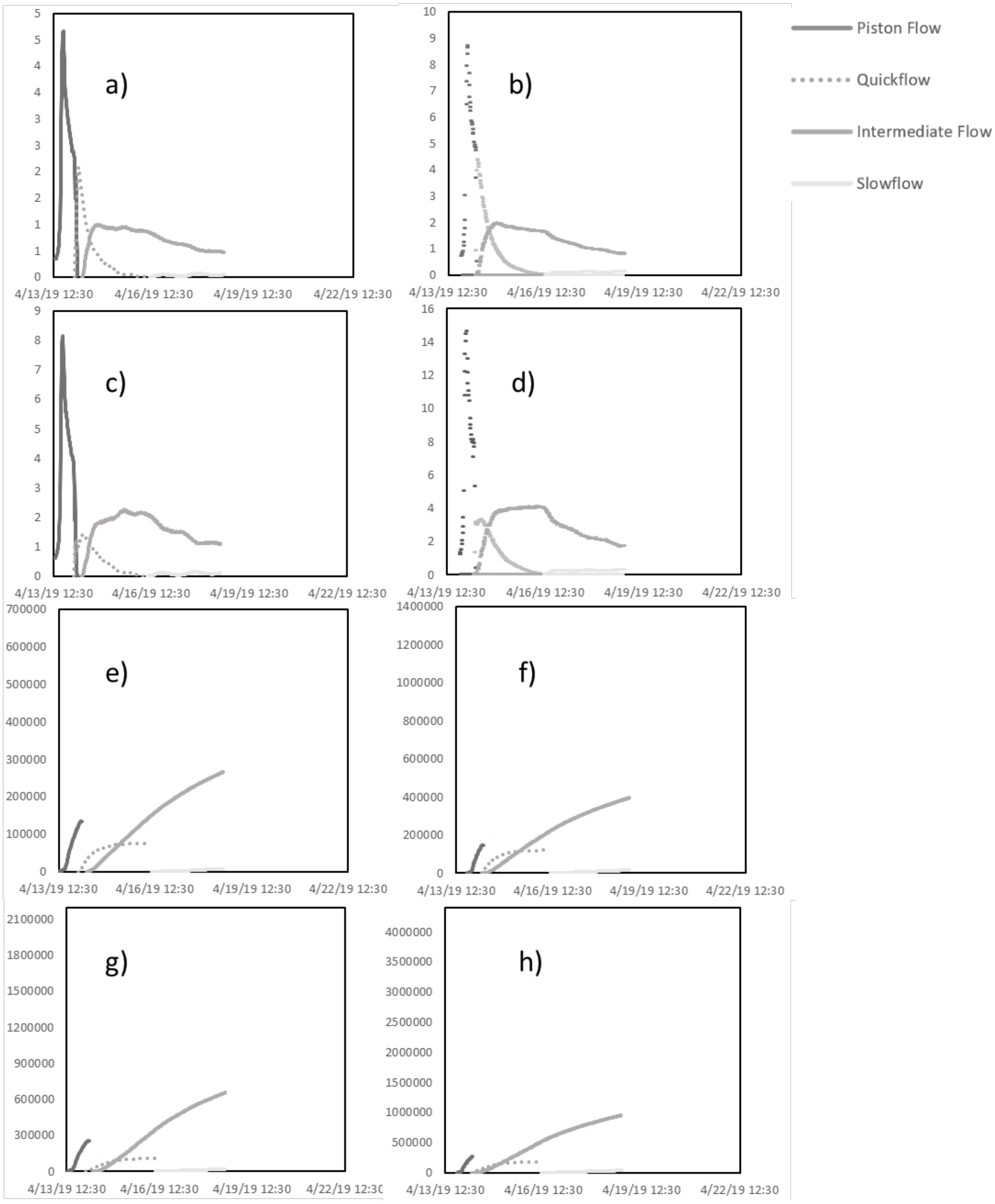

Figure 5.27 July Event Flow and Nitrate Unmixing where the left column shows Ramsey site and the right column shows South Elkhorn Gage Site. a) and b) show flow in L, c) and d) show nitrate in mg e) and f) show cumulative flow in Liters, g) and h) show cumulative n

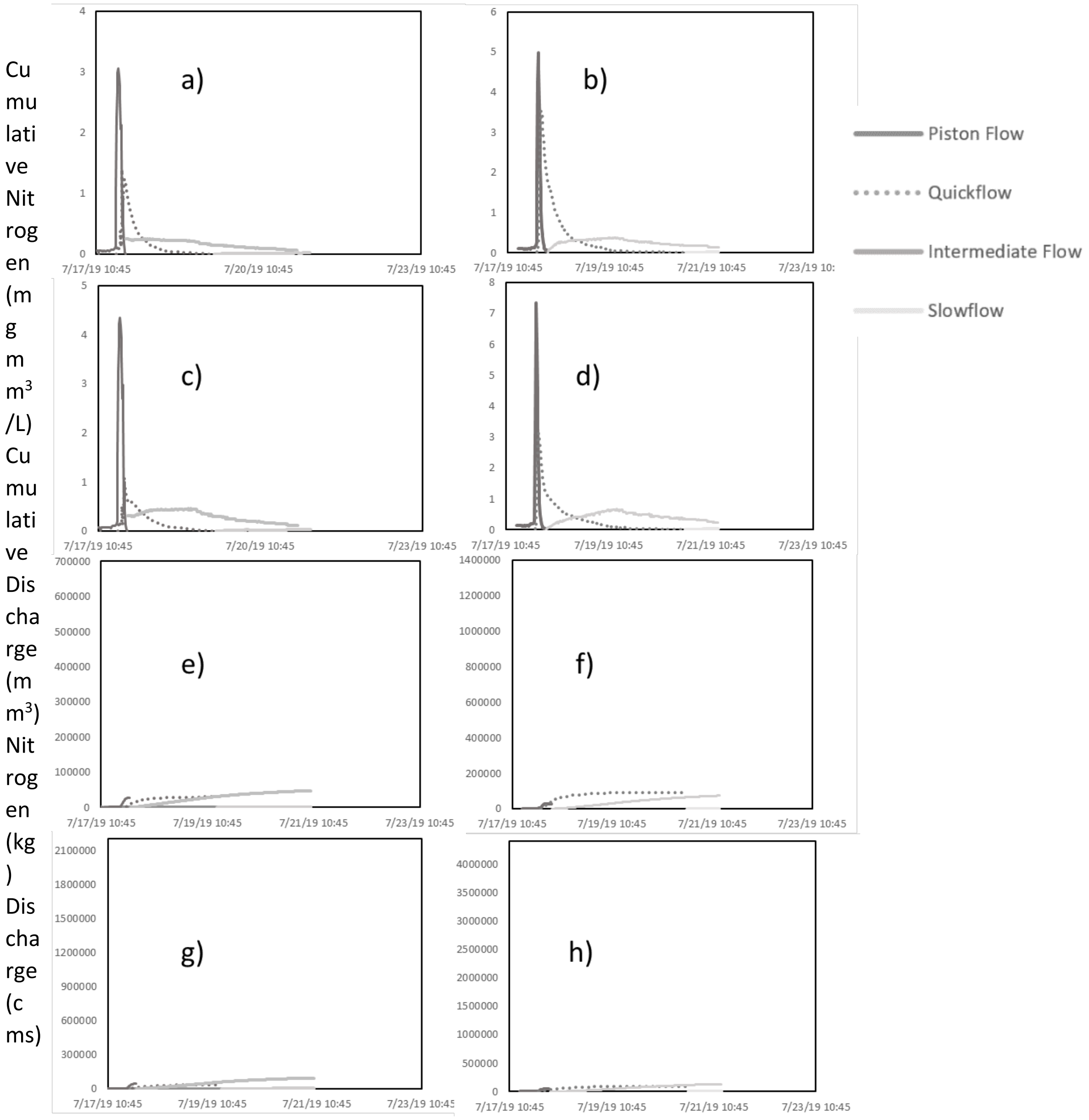

Figure 5.28 October Event Flow and Nitrate Unmixing where the left column shows Ramsey site and the right column shows South Elkhorn Gage Site. a) and b) show flow in L, c) and d) show nitrate in mg, e) and f) show cumulative flow in Liters, g) and h) show cumulative nitrogen in mg

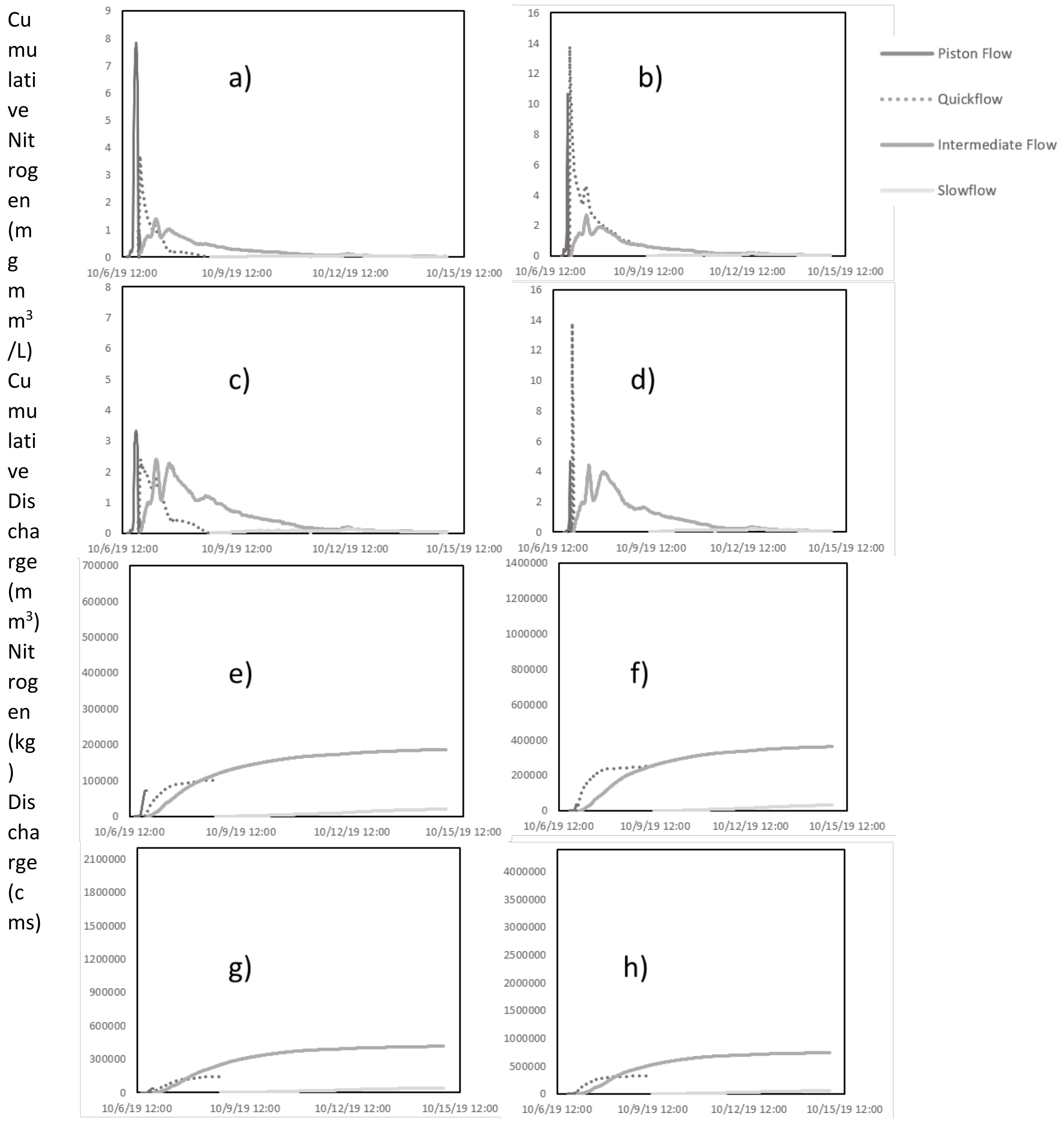

Figure 5.29 Volume of Water and Mass of Nitrogen Event Totals

January 4 2019 SE Event Totals	Q1 (Piston Flow)	Q2 & Q3 (Quickflow)	Q4 (Intermediate Flow)	Q5 (Slow Flow
Flow (m^3)	92598.347	388539.768	1319430.346	30142.856
Nitrogen (mg)	265777437.069	776175556.368	4298485106.074	100055673.663
Ramsey Event Totals				
Flow (m^3)	99465.215	214414.140	665285.626	18212.354
Nitrogen (mg)	264519389.518	377001519.118	2086459562.795	58107418.144
April 13 2019 SE Event Totals	Q1 (Piston Flow)	Q2 & Q3 (Quickflow)	Q4 (Intermediate Flow)	Q5 (Slow Flow
Flow (m^3)	148132.615	119956.308	395088.272	15966.701
Nitrogen (mg)	267621039.779	183044720.201	953137523.305	39749859.566
Ramsey Event Totals				
Flow (m^3)	134219.731	76149.762	271571.339	7172.401
Nitrogen (mg)	254396122.951	108654052.432	669746277.571	18551800.256
July 17 2019 SE Event Totals	Q1 (Piston Flow)	Q2 & Q3 (Quickflow)	Q4 (Intermediate Flow)	Q5 (Slow Flow
Flow (m^3)	30230.981	92768.139	74265.709	650.391
Nitrogen (mg)	42629351.746	96710762.703	133783724.287	1294793.512
Ramsey Event Totals				
Flow (m^3)	27451.730	29597.891	47518.145	1677.569
Nitrogen (mg)	41700632.273	33217838.051	94176726.201	3505792.971
October 6 2019 SE Event Totals	Q1 (Piston Flow)	Q2 & Q3 (Quickflow)	Q4 (Intermediate Flow)	Q5 (Slow Flow
Flow (m^3)	33510.016	249621.536	362120.426	32323.452
Nitrogen (mg)	16445981.178	326350486.767	740164414.612	57949139.261
Ramsey Event Totals				
Flow (m^3)	71968.128	100397.779	416228.802	19924.480
Nitrogen (mg)	34968723.474	145668884.955	186466930.667	40471451.115

Figure 5.30 Percent contribution of nitrate from the different hydrologic pathways

Event	Site	Piston N	Quickflow N	Intermediate flow N	Slow flow N
January	Gage	5	14	79	2
January	Ramsey	9	14	75	2
April	Gage	19	13	66	3
April	Ramsey	24	10	64	2
July	Gage	16	35	49	0
July	Ramsey	24	19	55	2
October	Gage	1	29	65	5
October	Ramsey	9	36	46	10
	Mean	13	21	62	3
	StDev	9	10	12	3

Discharge (cms)

Figure 5.31 January 2019 Ramsey Model Results for total flow a), total nitrogen b), piston effect flow c), quick flow d), intermediate flow e), and slow flow f)

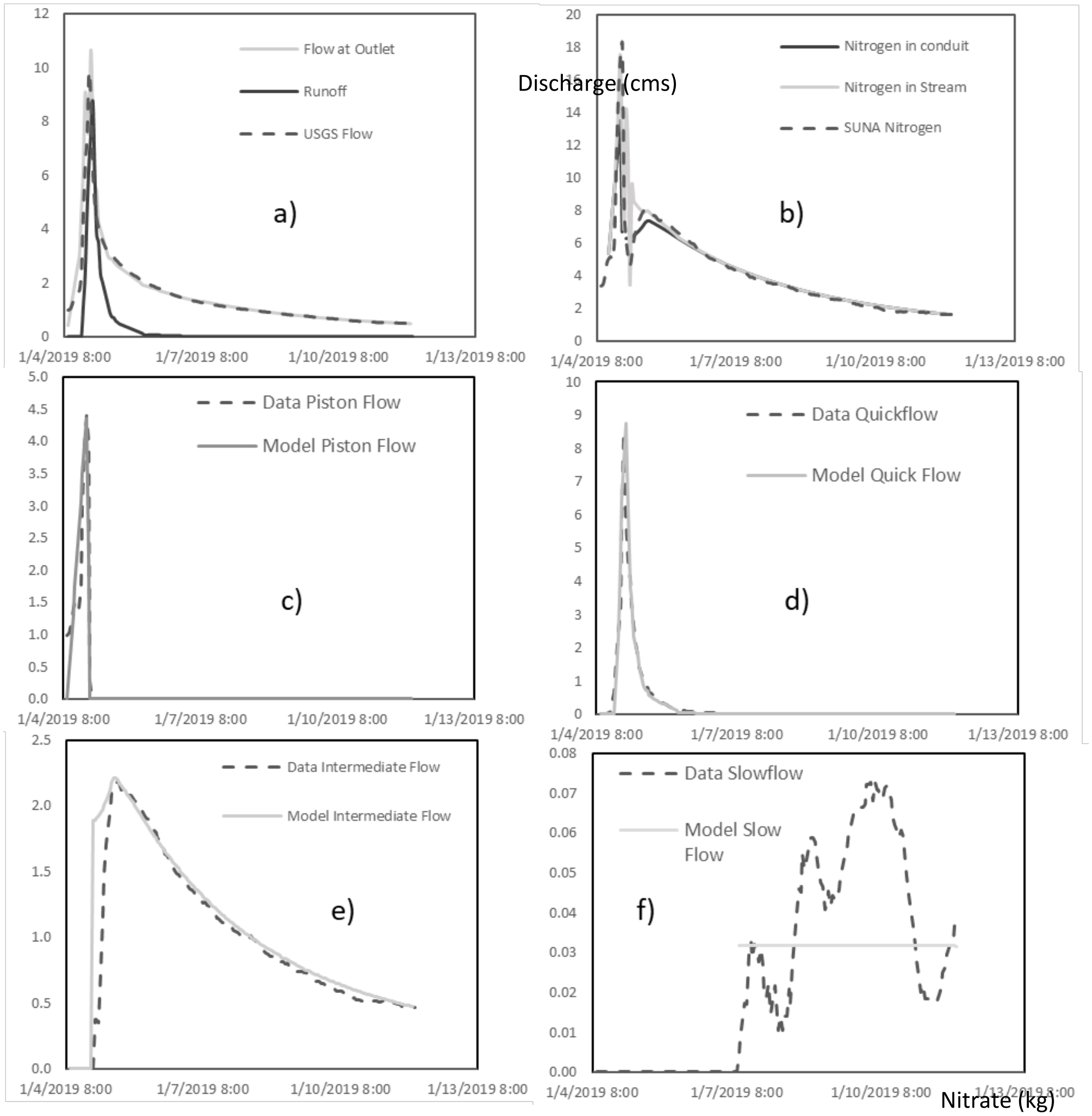

Figure 5.32 January 2019 Ramsey model results for piston flow nitrogen a), quick flow nitrogen b), intermediate flow nitrogen c), and slow flow nitrogen d) all units are in Kg/s

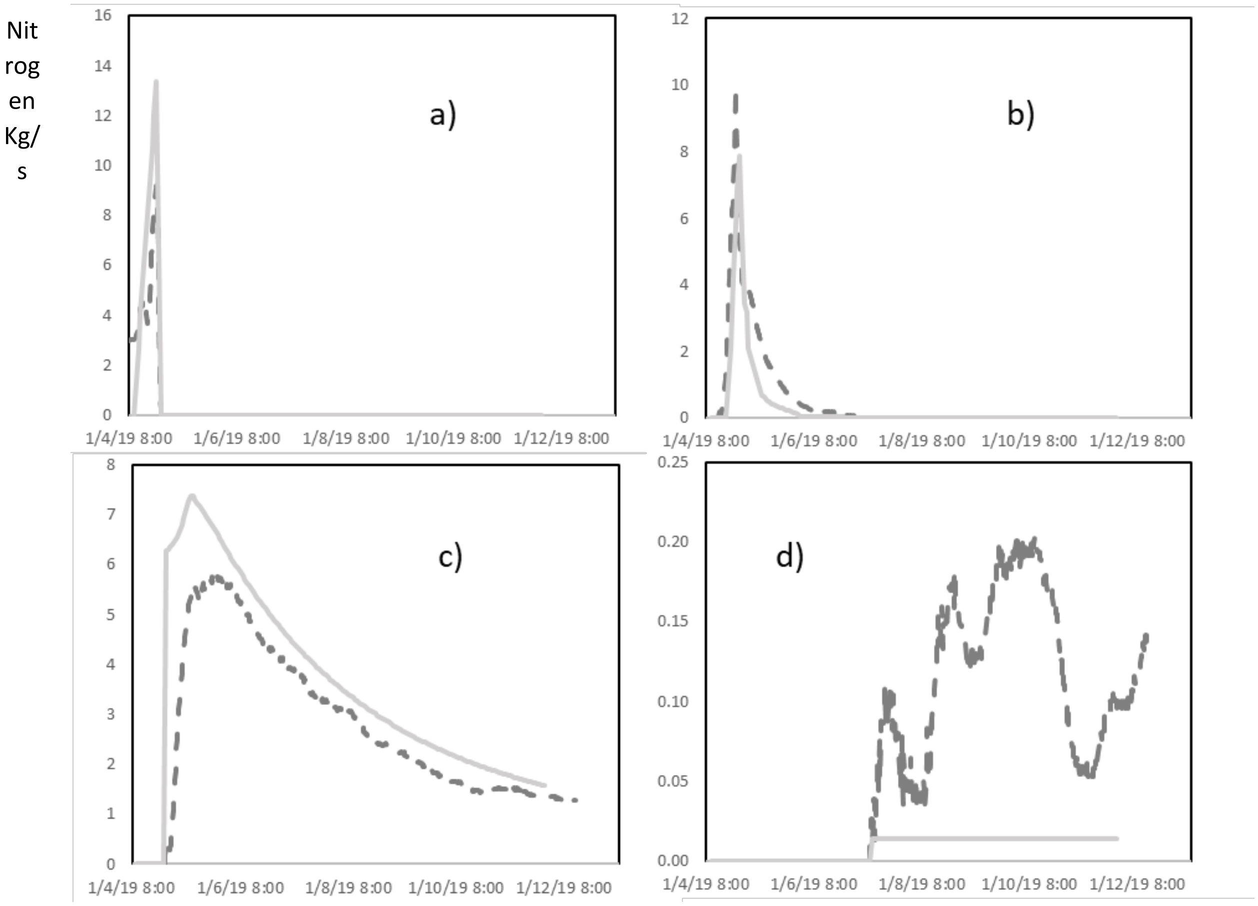

Figure 5.33 January 2019 SE Gage model results for total flow a), total nitrogen b), piston effect flow c), quick flow d), intermediate flow e), and slow flow f)

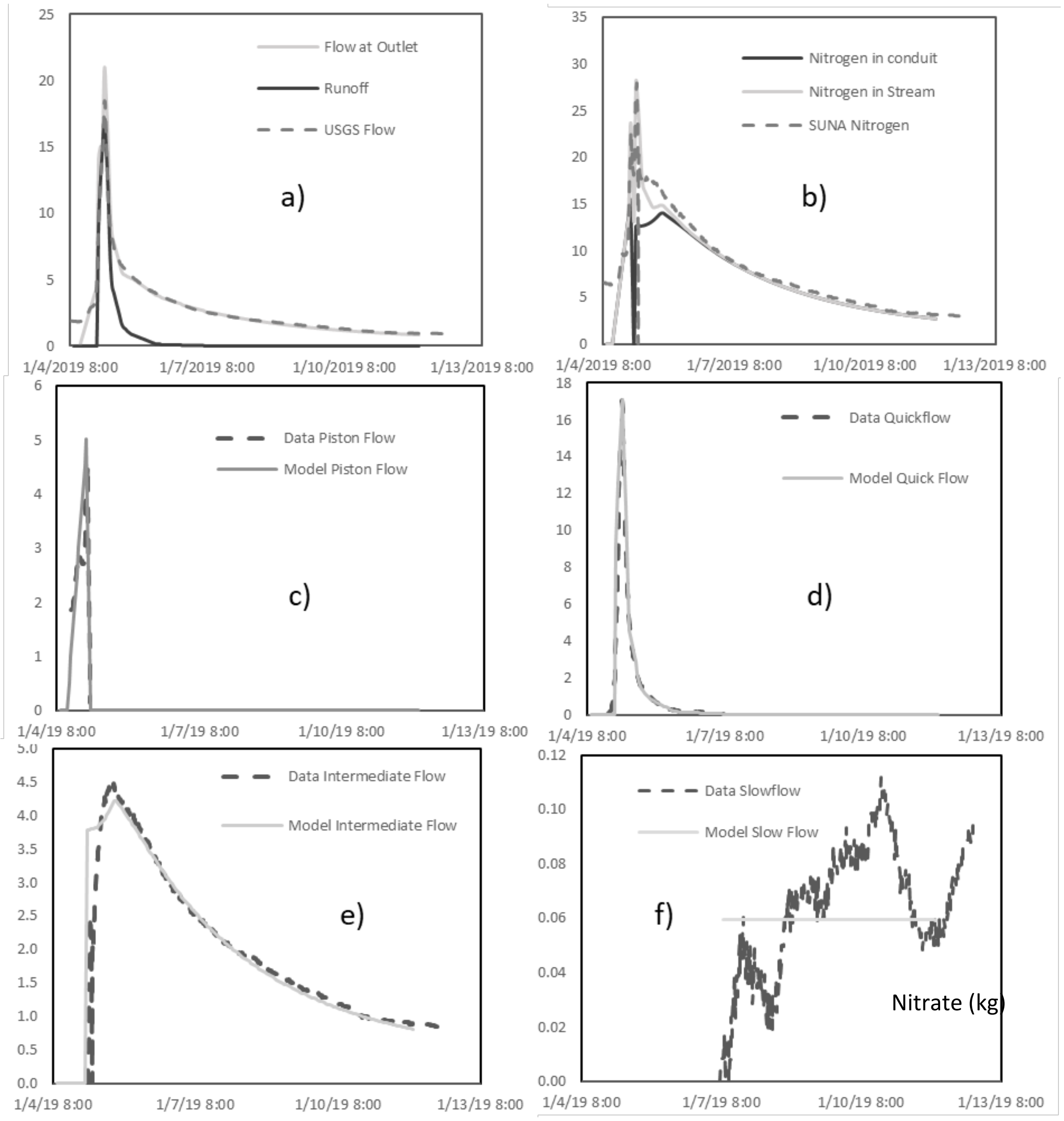

Figure 5.34 January 2019 SE Gage model results for piston flow nitrogen a), quick flow nitrogen b), intermediate flow nitrogen c), and slow flow nitrogen d) all units are in Kg/s

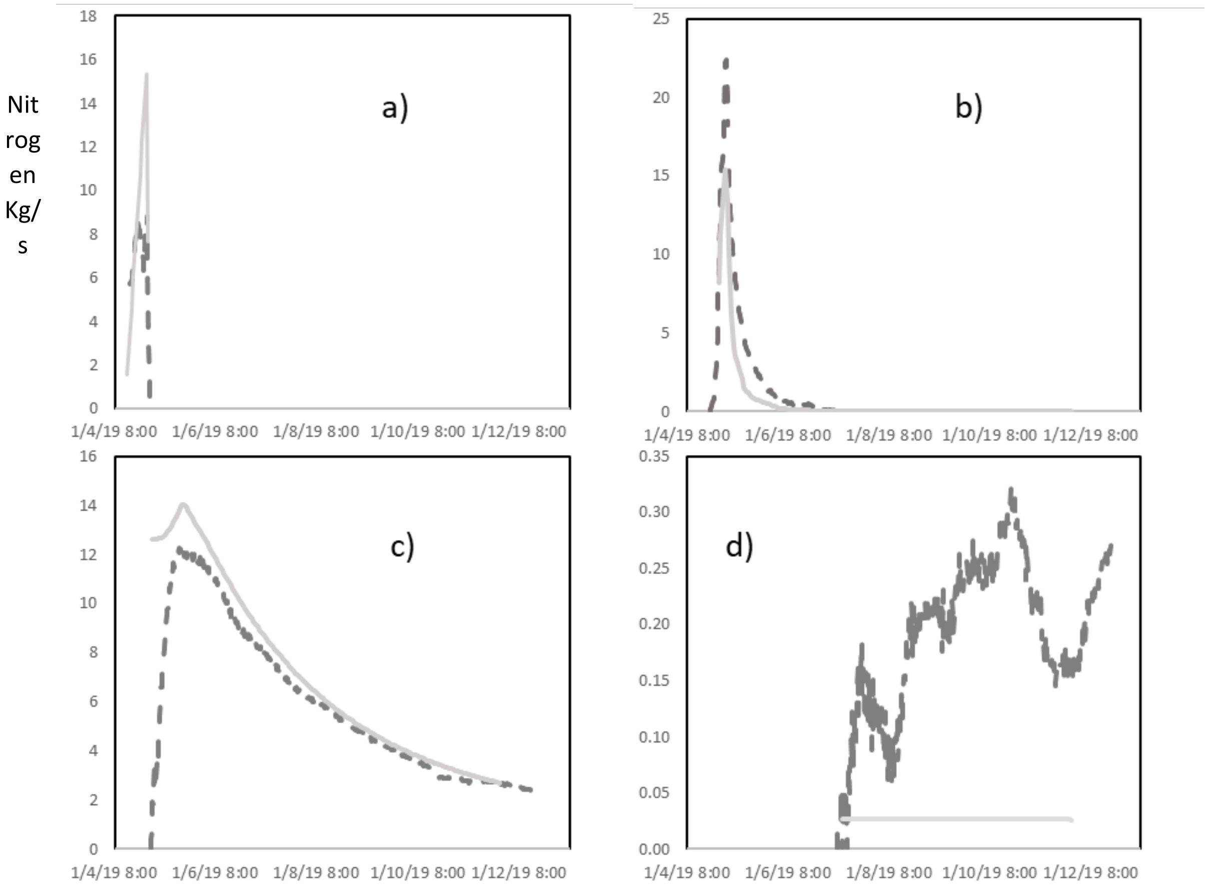

Figure 5.35 April 2019 Ramsey model results for total flow a), total nitrogen b), piston effect flow c), quick flow d), intermediate flow e), and slow flow f)

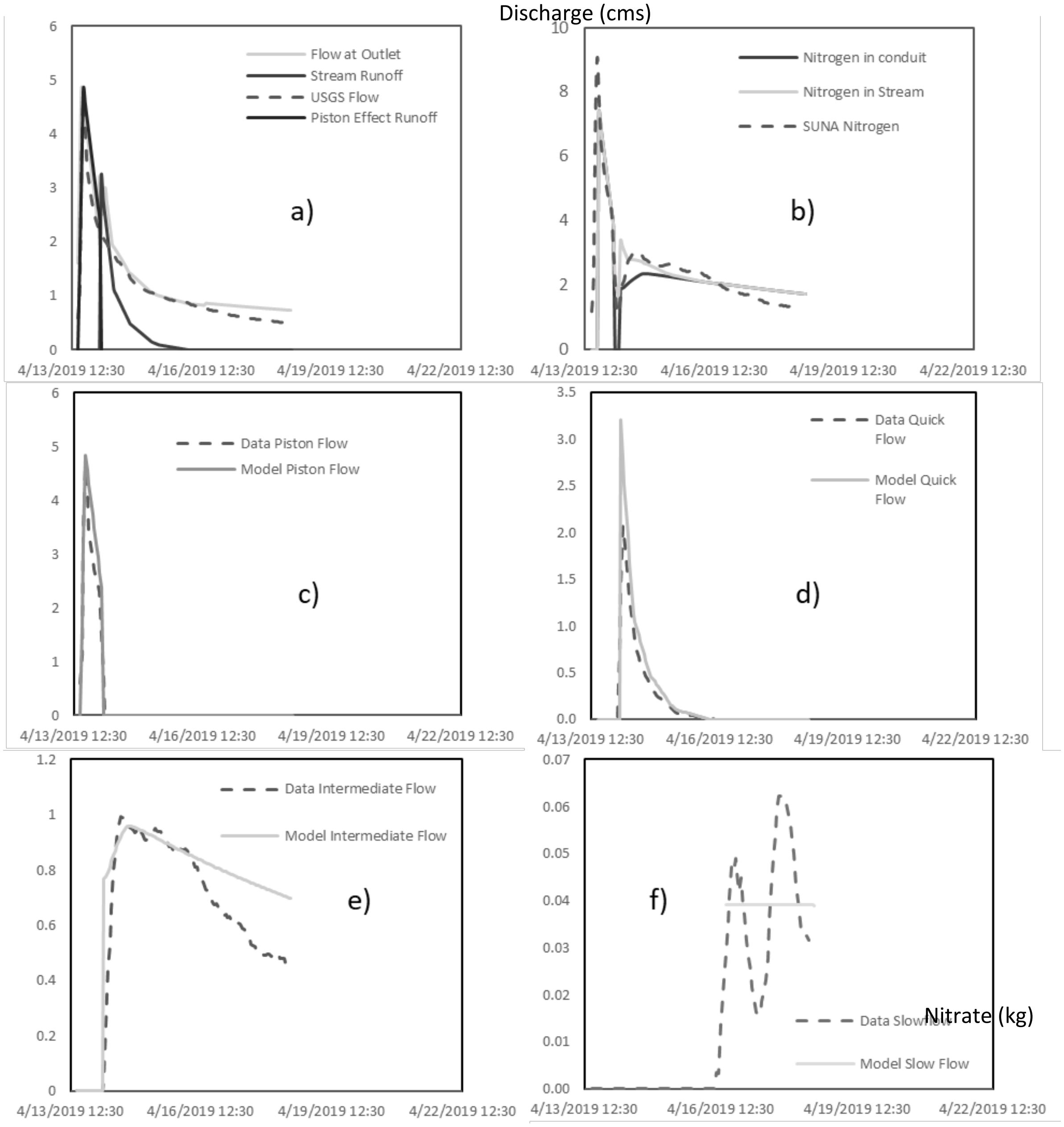

Figure 5.36 April 2019 Ramsey model results for piston flow nitrogen a), quick flow nitrogen b), intermediate flow nitrogen c), and slow flow nitrogen d) all units are in Kg/s

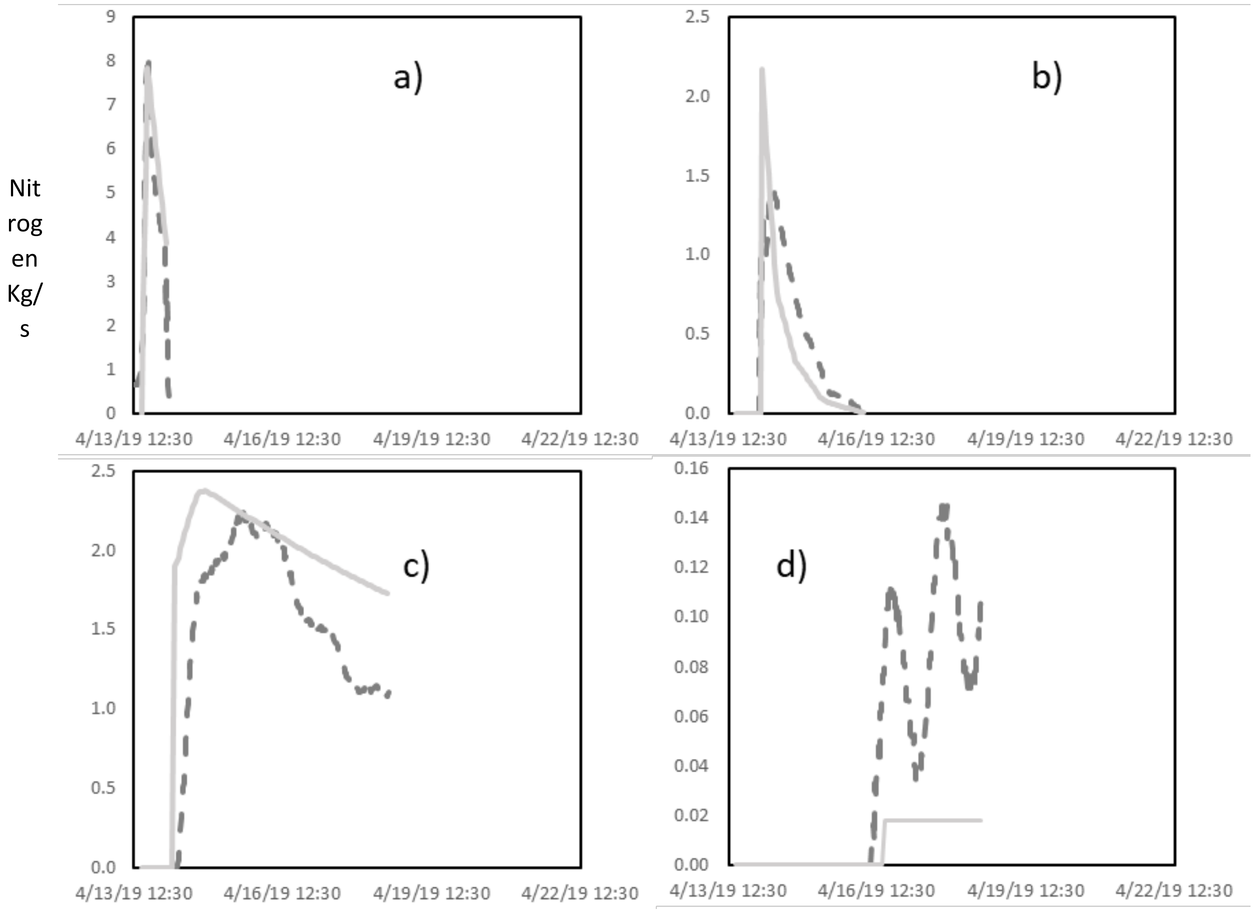

Figure 5.37 April 2019 SE Gage model results for total flow a), total nitrogen b), piston effect flow c), quick flow d), intermediate flow e), and slow flow f)

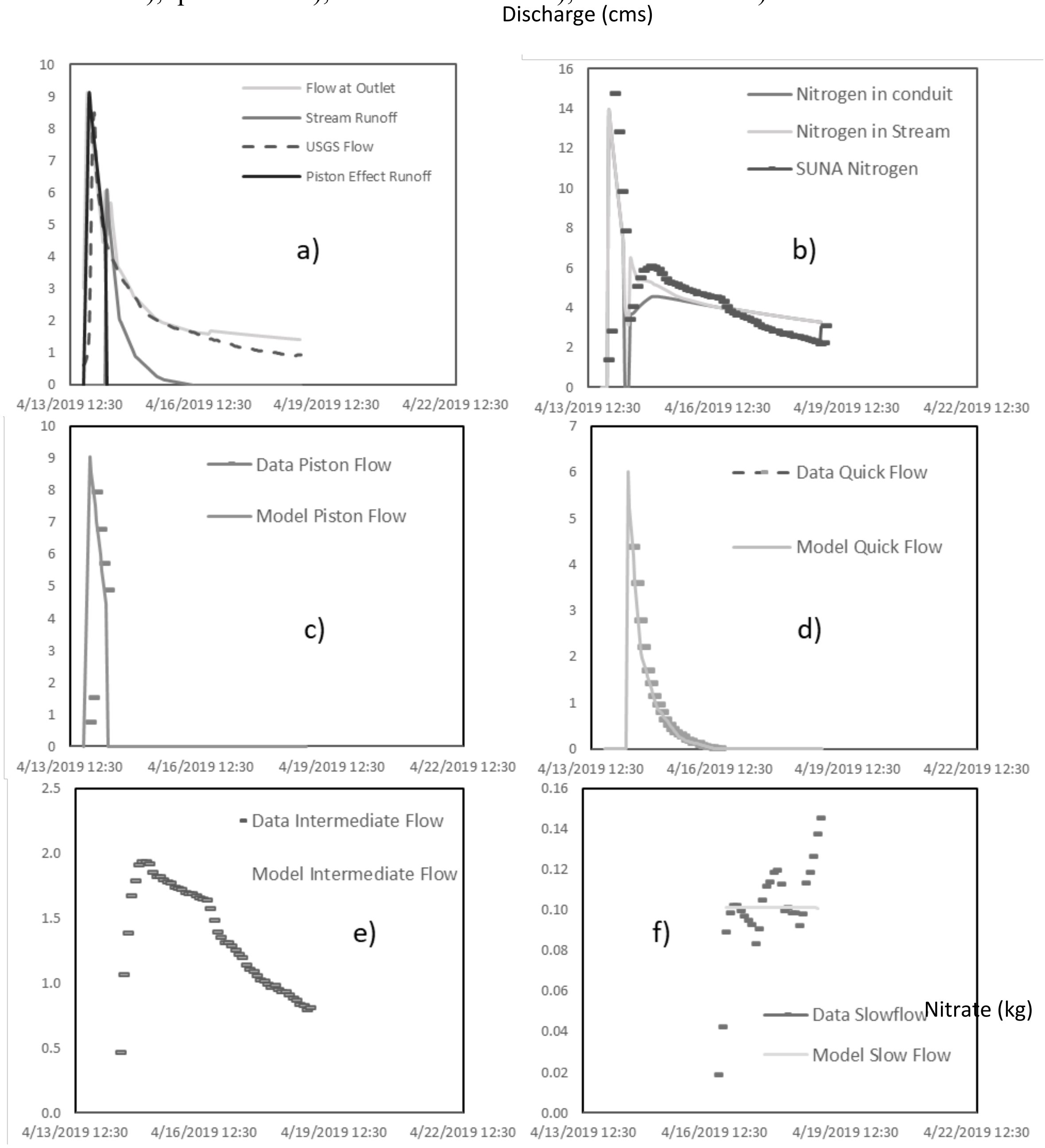

Figure 5.38 April 2019 SE Gage model results for piston flow nitrogen a), quick flow nitrogen b), intermediate flow nitrogen c), and slow flow nitrogen d) all units are in Kg/s

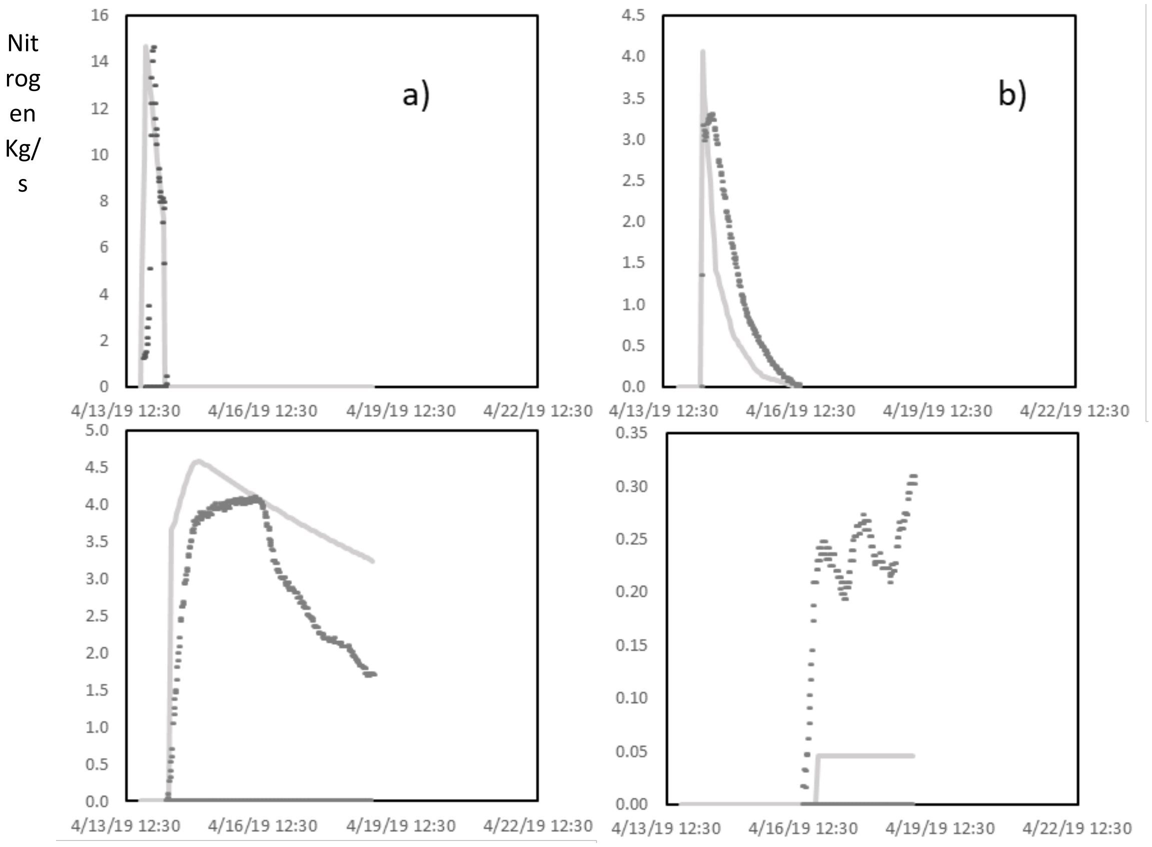

Figure 5.39 July 2019 Ramsey model results for total flow a), total nitrogen b), piston effect flow c), quick flow d), intermediate flow e), and slow flow f)

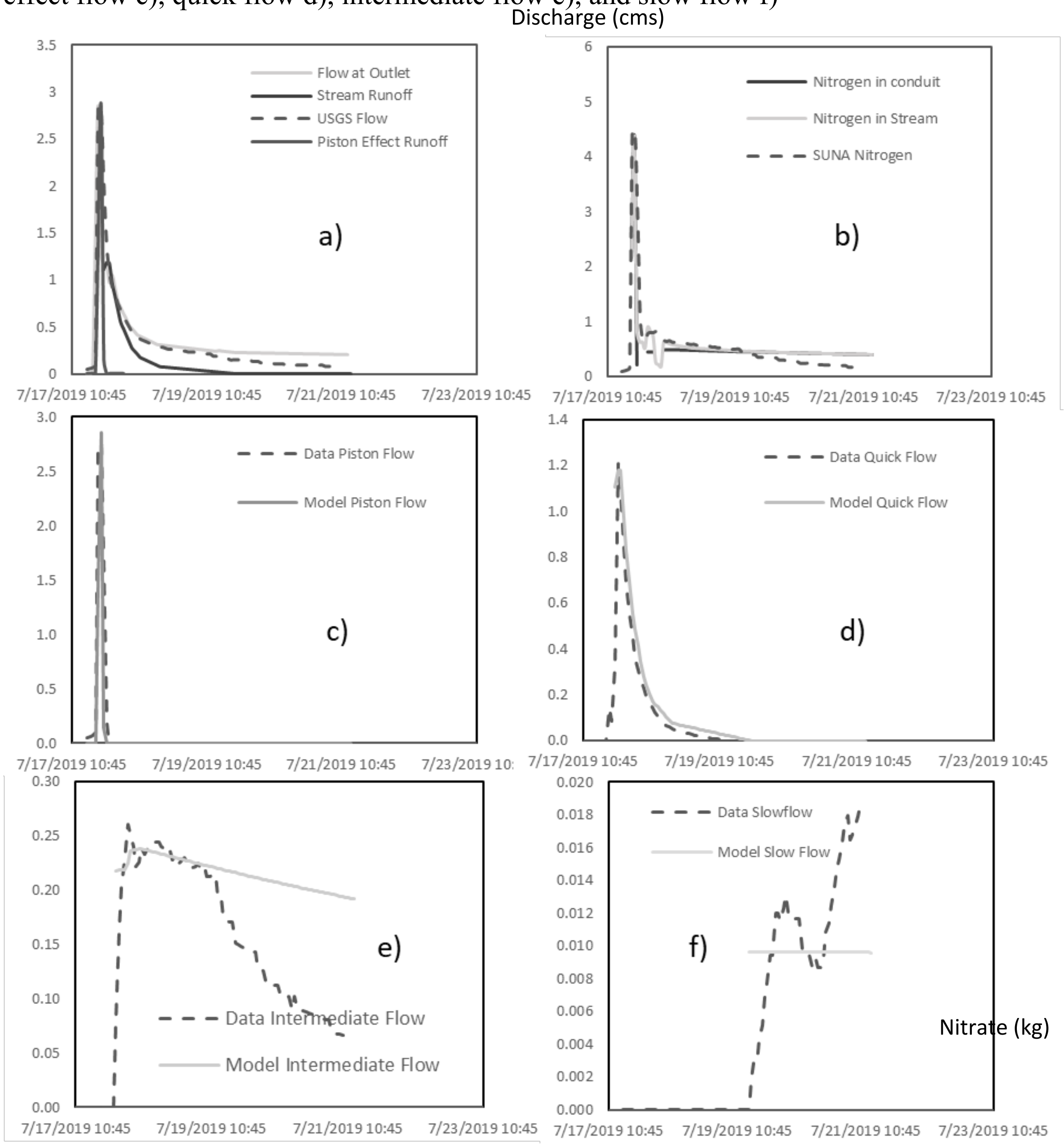

Figure 5.40 July 2019 Ramsey model results for piston flow nitrogen a), quick flow nitrogen b), intermediate flow nitrogen c), and slow flow nitrogen d) all units are in Kg/s

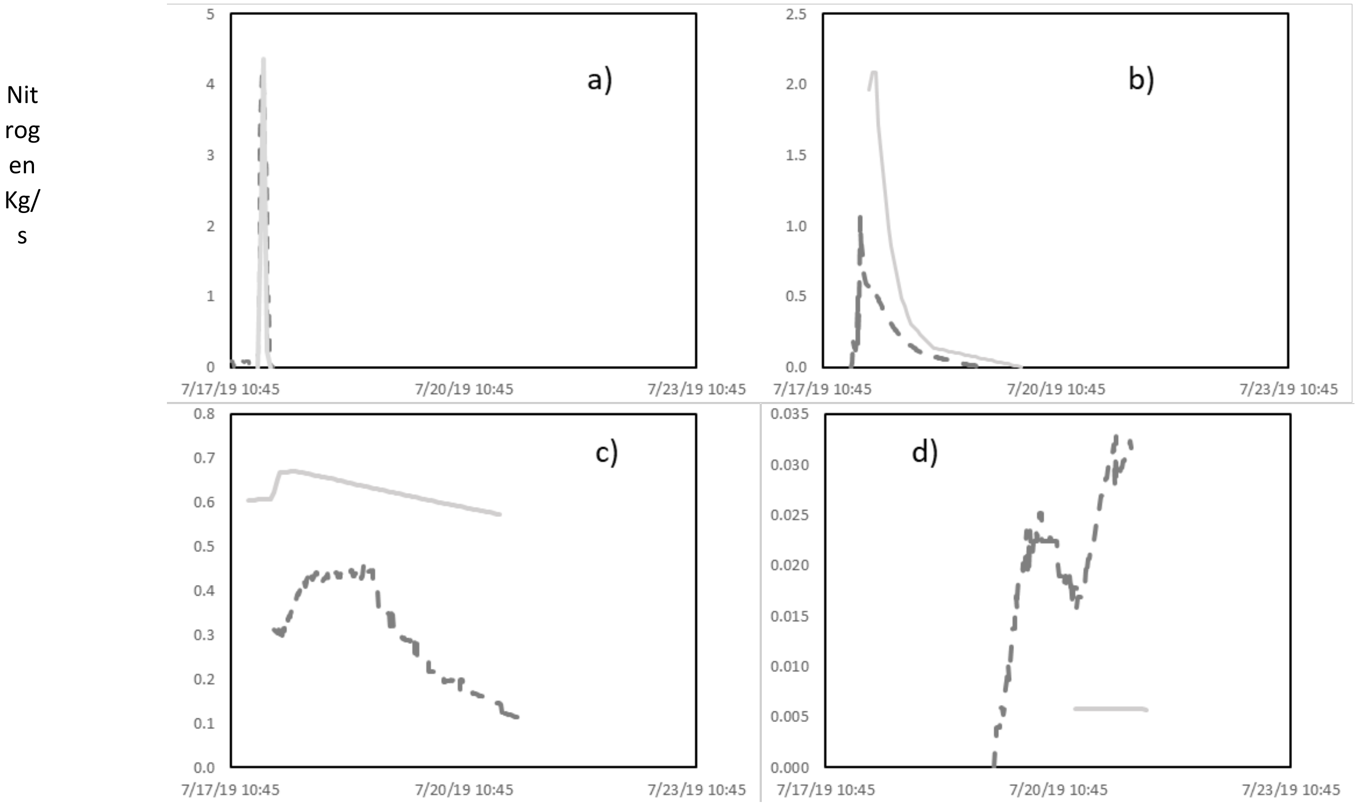

Figure 5.41 July 2019 SE Gage model results for total flow a), total nitrogen b), piston effect flow c), quick flow d), intermediate flow e), and slow flow f)

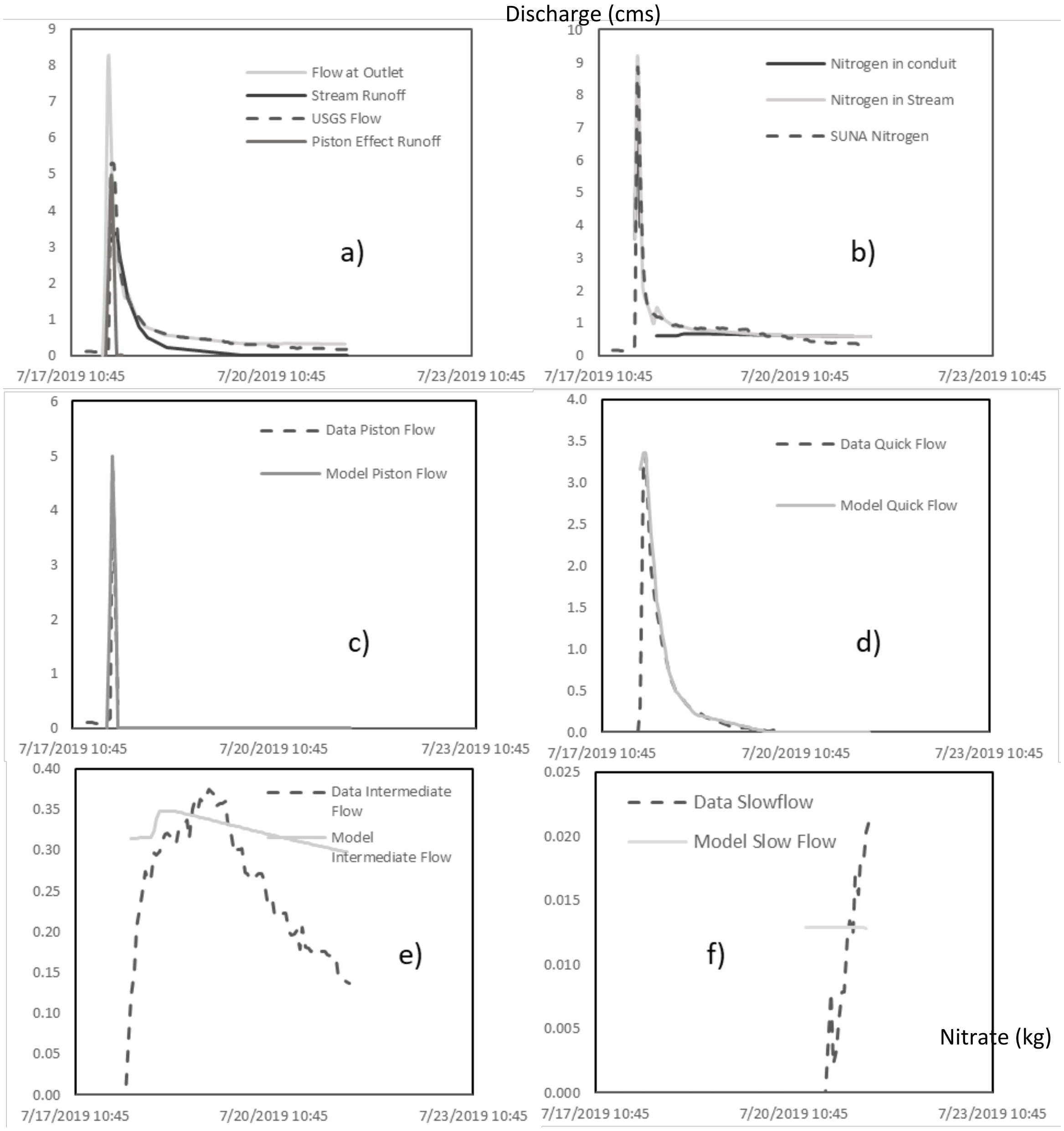

Figure 5.42 July 2019 SE Gage model results for piston flow nitrogen a), quick flow nitrogen b), intermediate flow nitrogen c), and slow flow nitrogen d) all units are in Kg/s

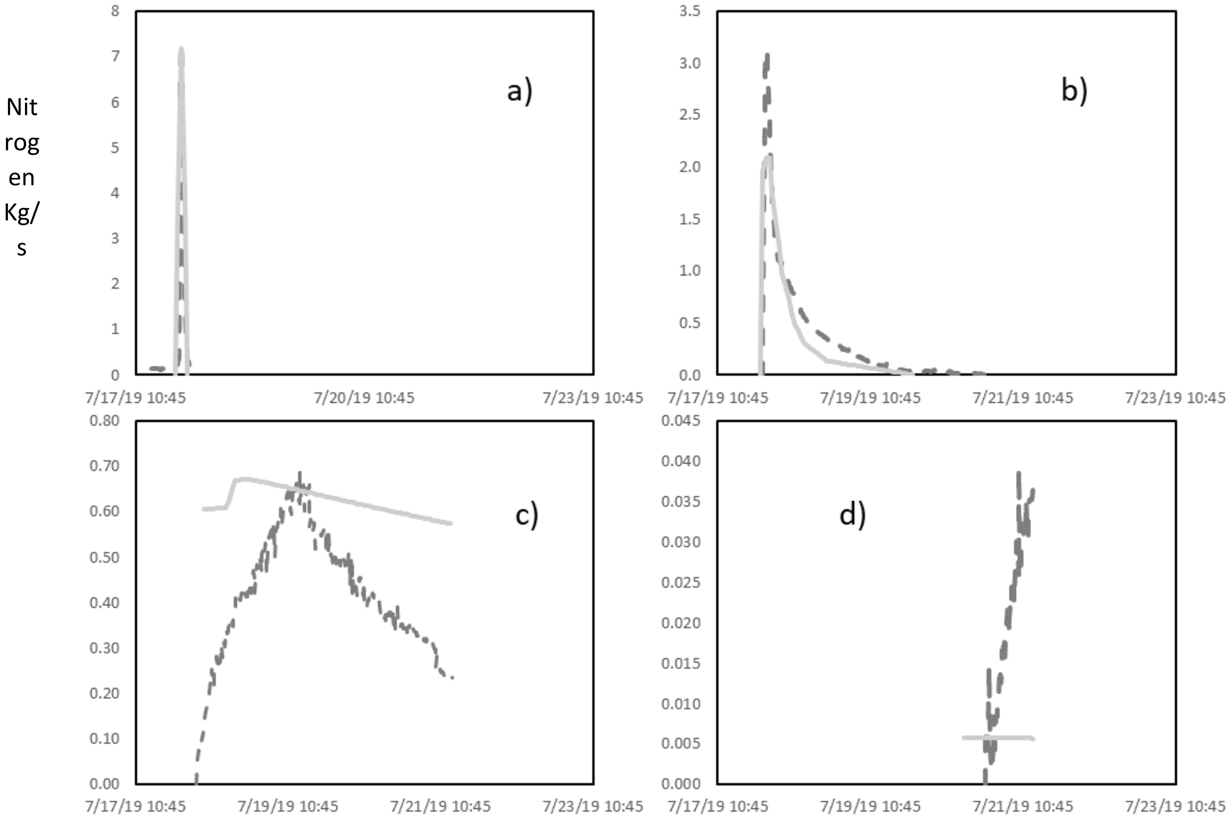

Figure 5.43 October 2019 Ramsey model results for total flow a), total nitrogen b), piston effect flow c), quick flow d), intermediate flow e), and slow flow f)

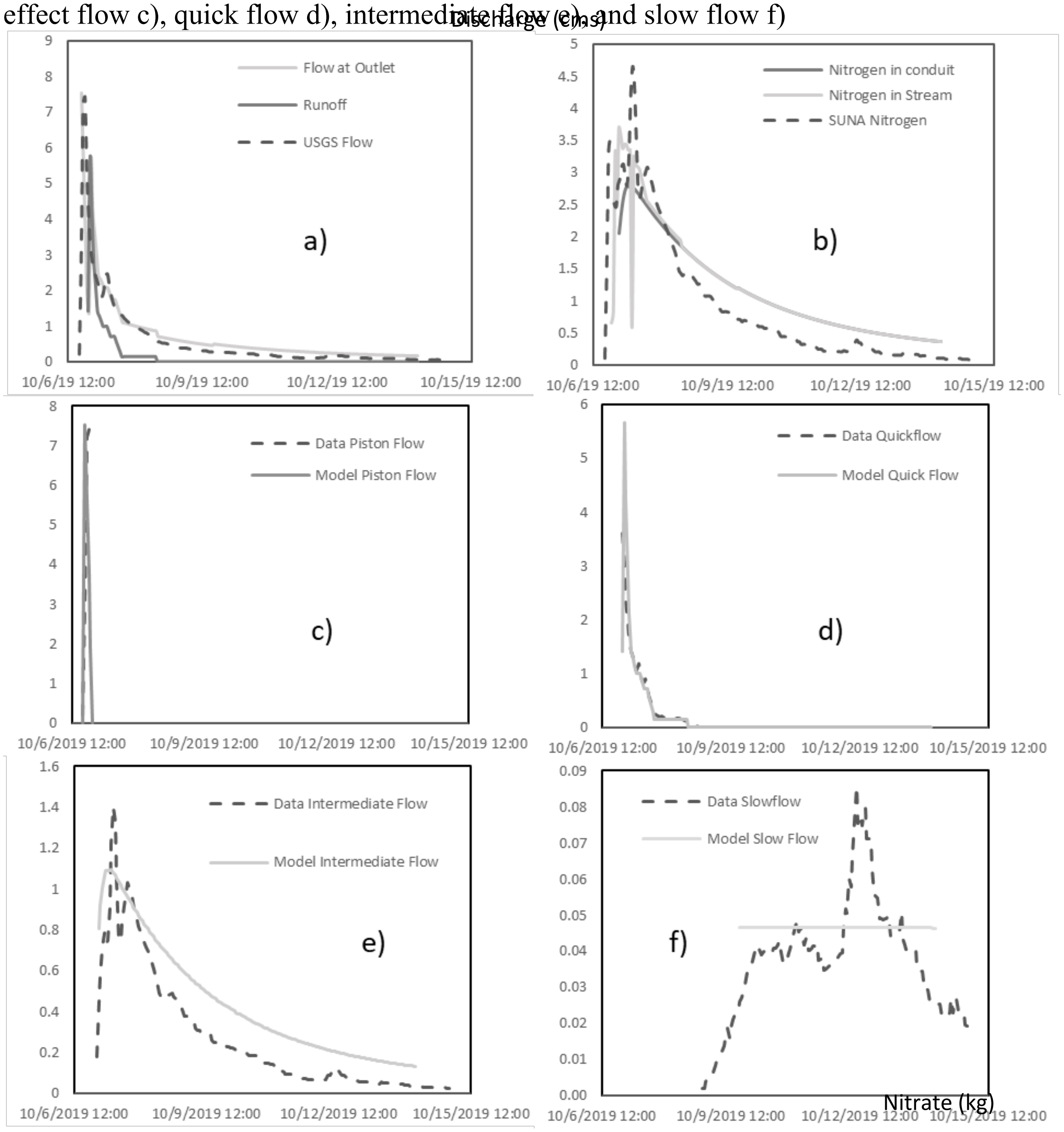

Figure 5.44 October 2019 Ramsey model results for piston flow nitrogen a), quick flow nitrogen b), intermediate flow nitrogen c), and slow flow nitrogen d) all units are in Kg/s

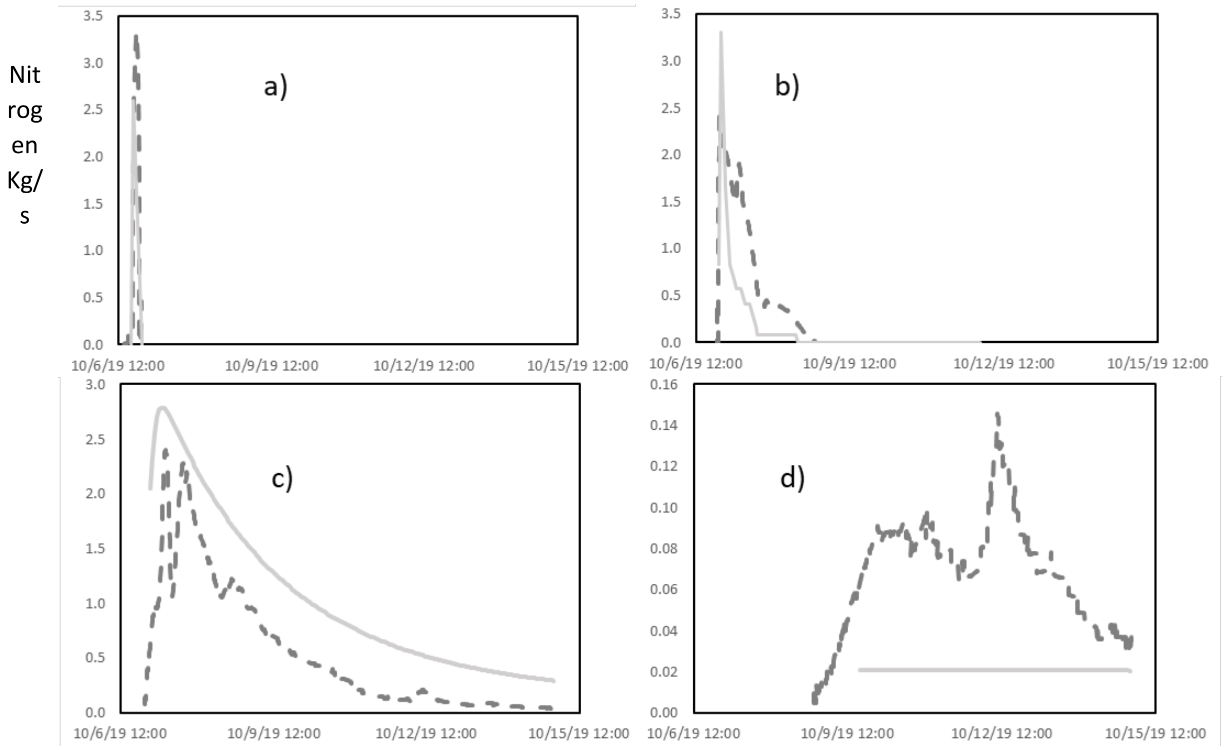

Figure 5.45 October 2019 SE Gage model results for total flow a), total nitrogen b), piston effect flow c), quick flow d), intermediate flow e), and slow flow f)

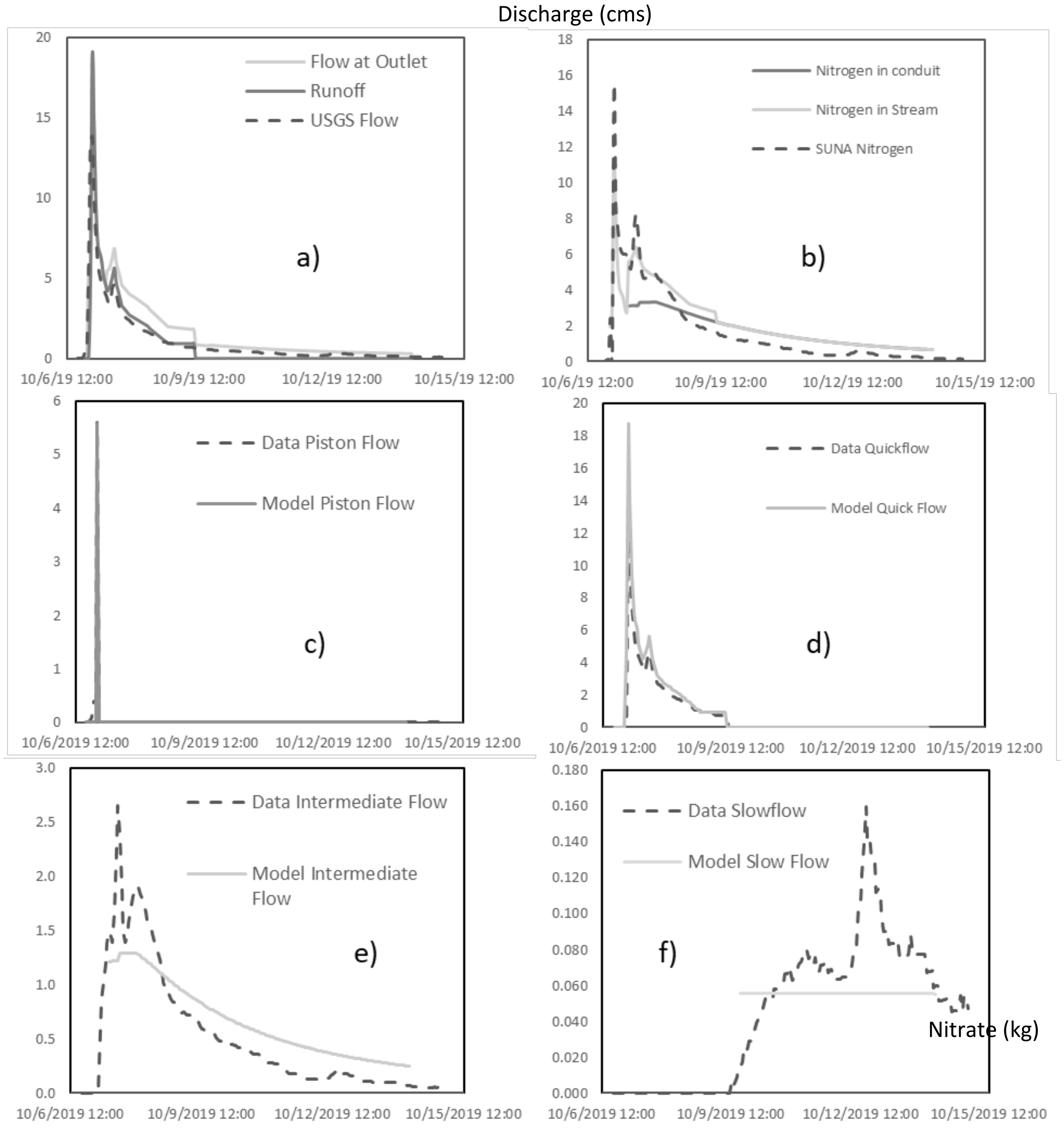

Figure 5.46 October 2019 SE Gage model results for piston flow nitrogen a), quick flow nitrogen b), intermediate flow nitrogen c), and slow flow nitrogen d) all units are in Kg/s

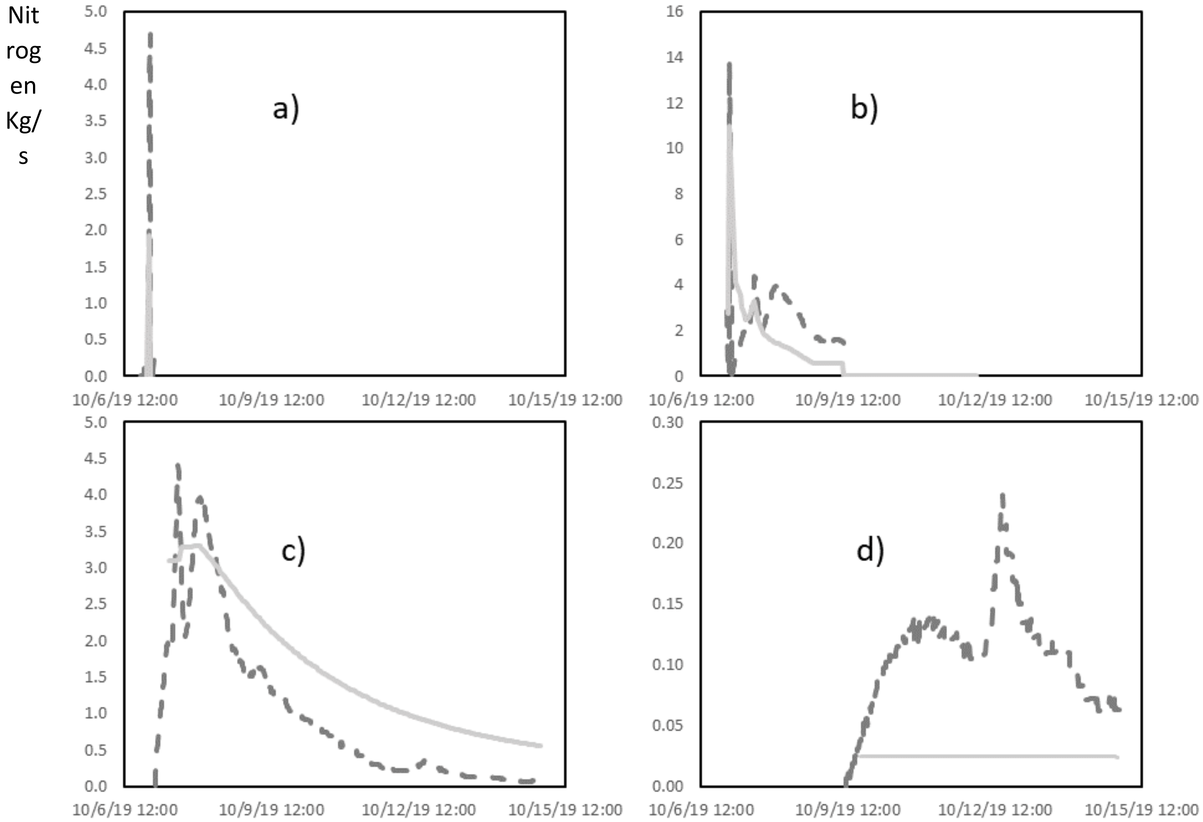

Figure 5.47 All Model Calibration Statistics (R2 Value)

	Piston Flow	Quickflow	Intermediate Flow	Slow Flow	Flow Totals	Nitrogen Totals
Jan SE Gage	0.95	0.97	0.95	0.74	0.97	0.94
Jan Ramsey	0.67	0.95	0.87	0.64	0.91	0.81
April SE Gage	0.12	1.00	0.66	0.42	0.69	0.89
April Ramsey	0.98	0.93	0.87	0.79	0.95	0.32
July SE Gage	0.90	0.80	0.83	0.92	0.91	0.88
July Ramsey	0.78	0.89	0.56	0.79	0.87	0.73
Oct SE Gage	0.99	0.97	0.68	0.74	0.83	0.90
Oct Ramsey	0.79	0.72	0.93	0.33	0.68	0.83

Figure 5.48 Graphs of sensitivity analysis of the January event at SE Gage with varied α (a and b) and varied β (c and d) for intermediate (a and c) and slowflow (b and d) pathways

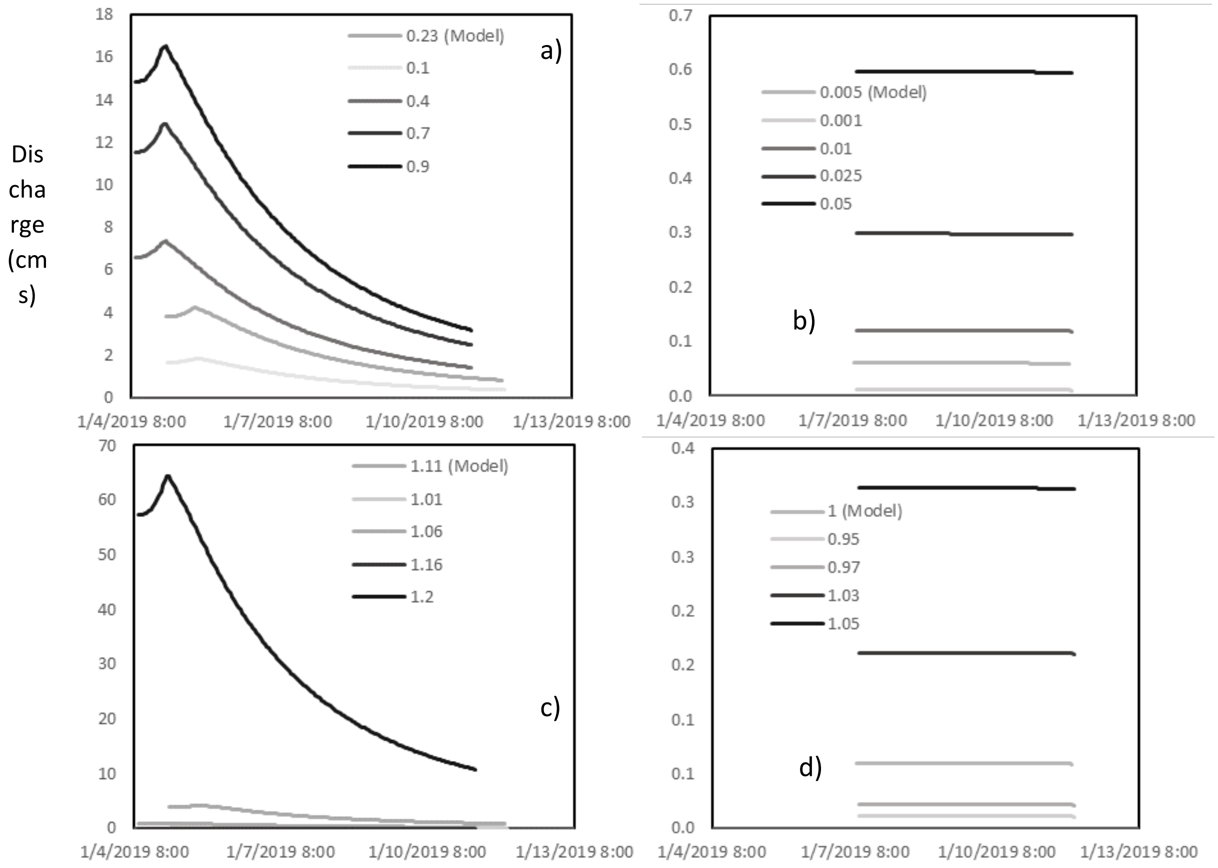

Figure 5.49 Modeled soil reservoir volumes for each event at both sites

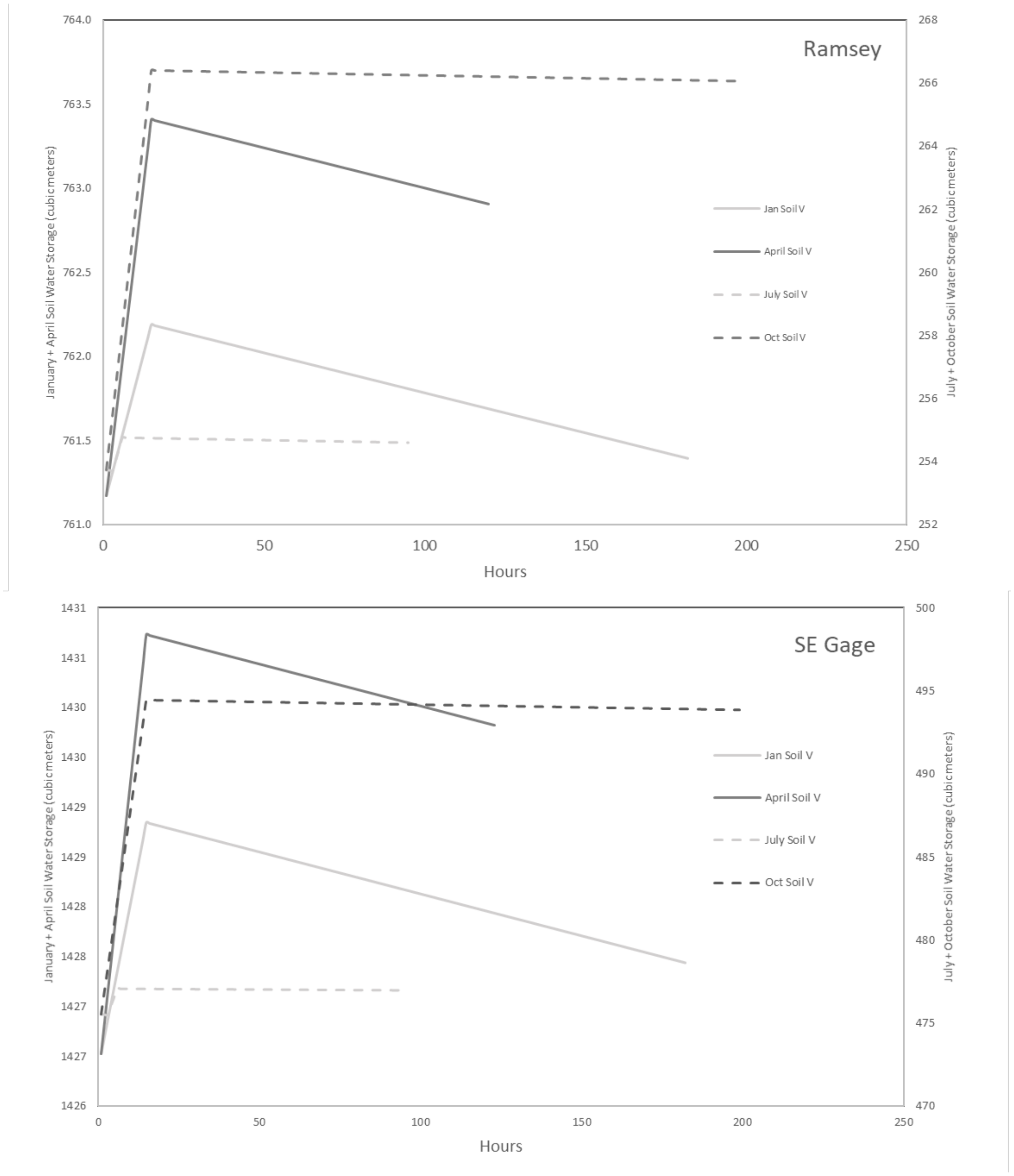

Figure 5.50 Modeled fracture network reservoir volumes for each event at both sites

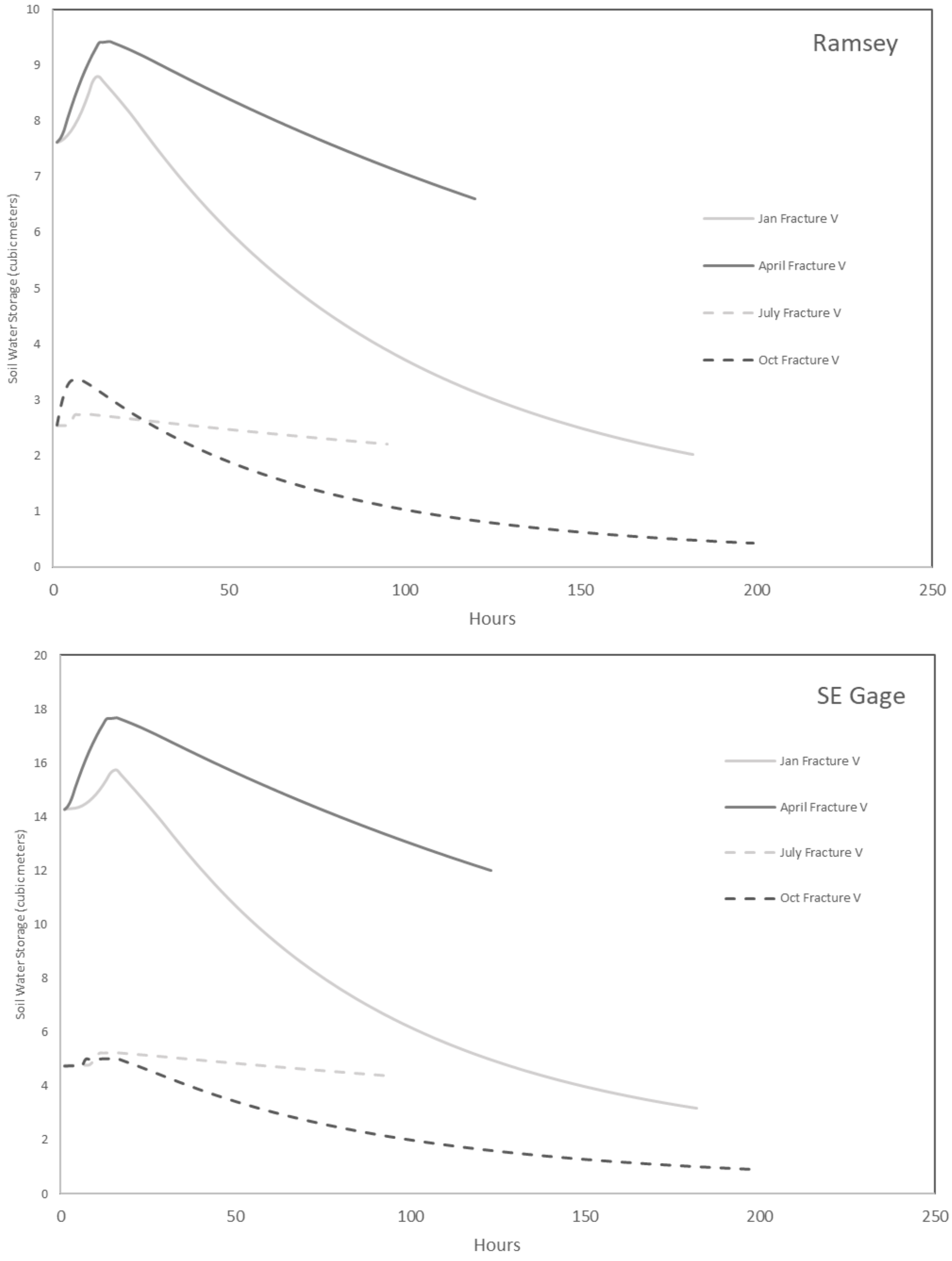

Figure 5.51 Modeled rock matrix reservoir volumes for each event at both sites

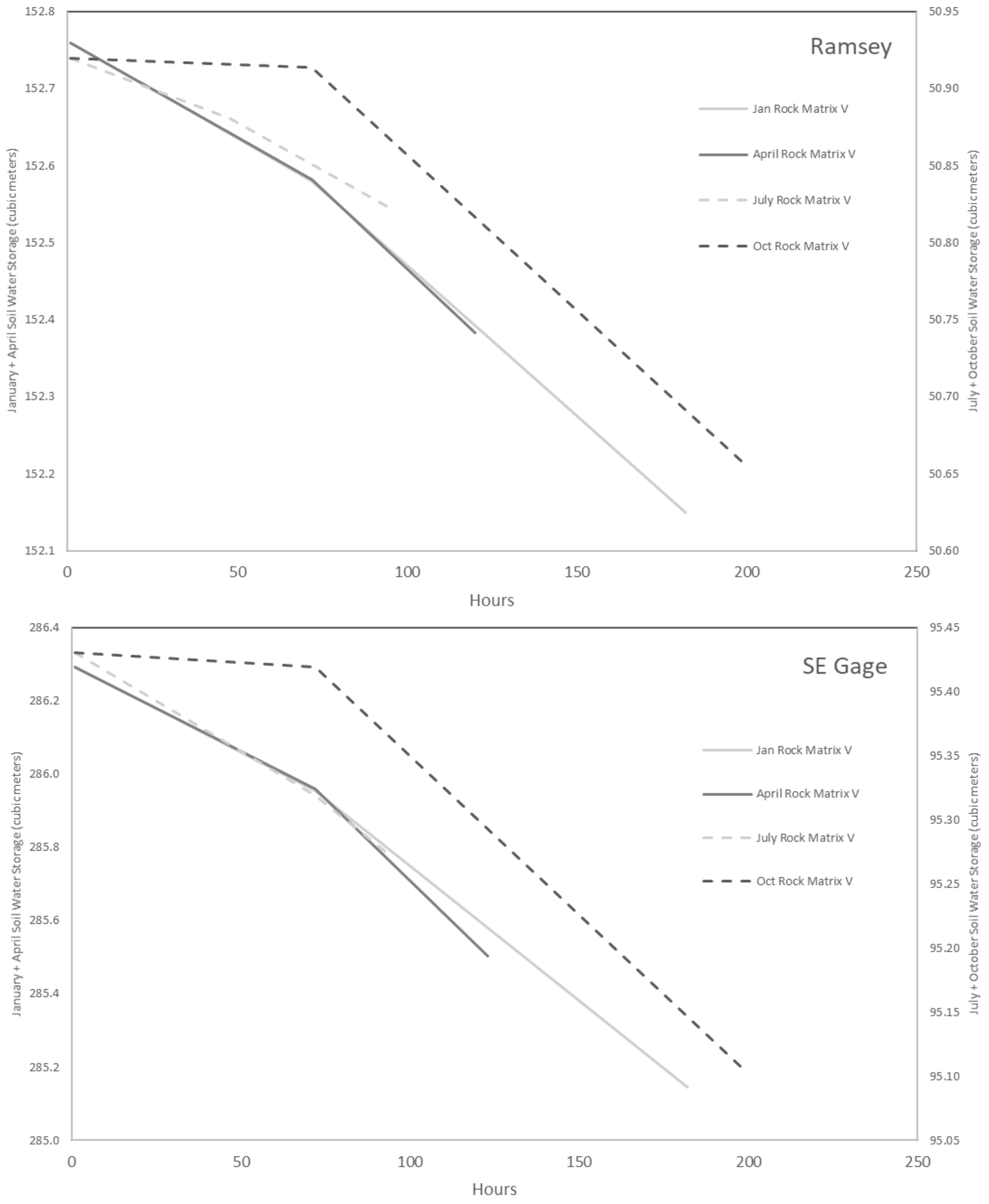

Figure 5.52 Soil Moisture Conditions at 5 inch depth from USGS gage at Bluegrass Airport.

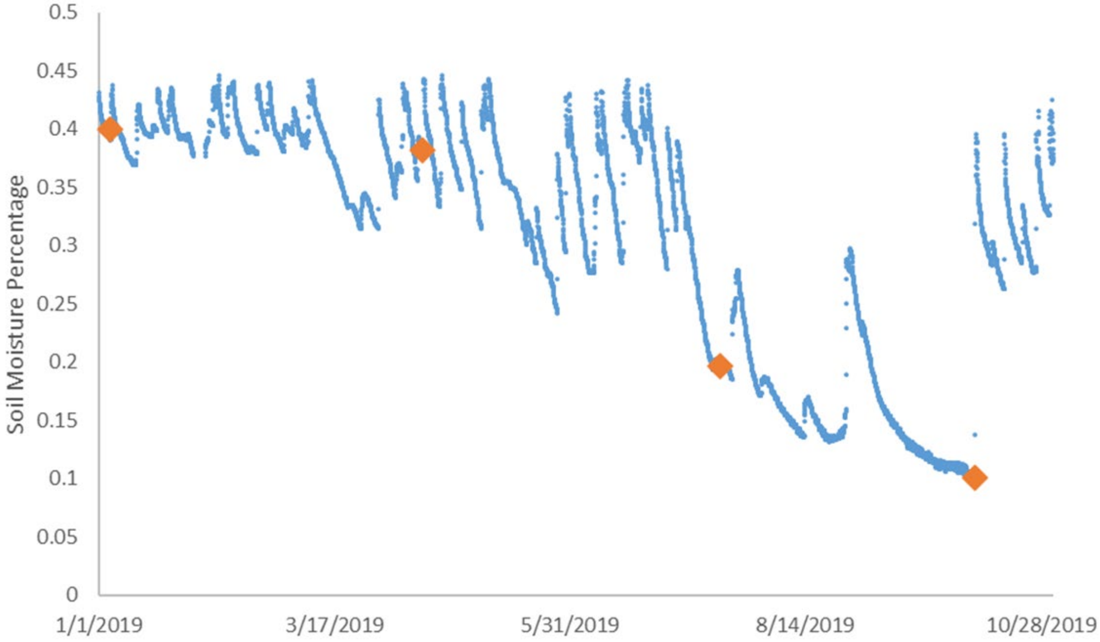

Figure 5.53 Alpha and Beta value range and proposed values

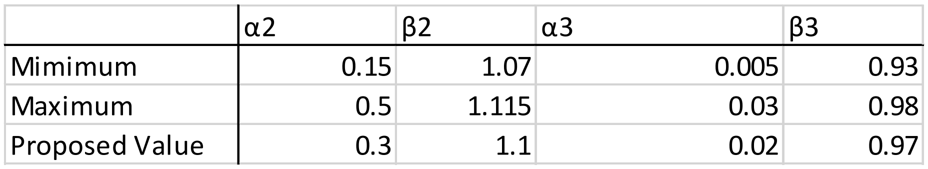

	α2	β2	α3	β3
Mimimum	0.15	1.07	0.005	0.93
Maximum	0.5	1.115	0.03	0.98
Proposed Value	0.3	1.1	0.02	0.97

Figure 5.54 Prediction of December (a,b), April (c,d), July (e,f), and October (g,f) events at the Ramsey and South Elkhorn Sites

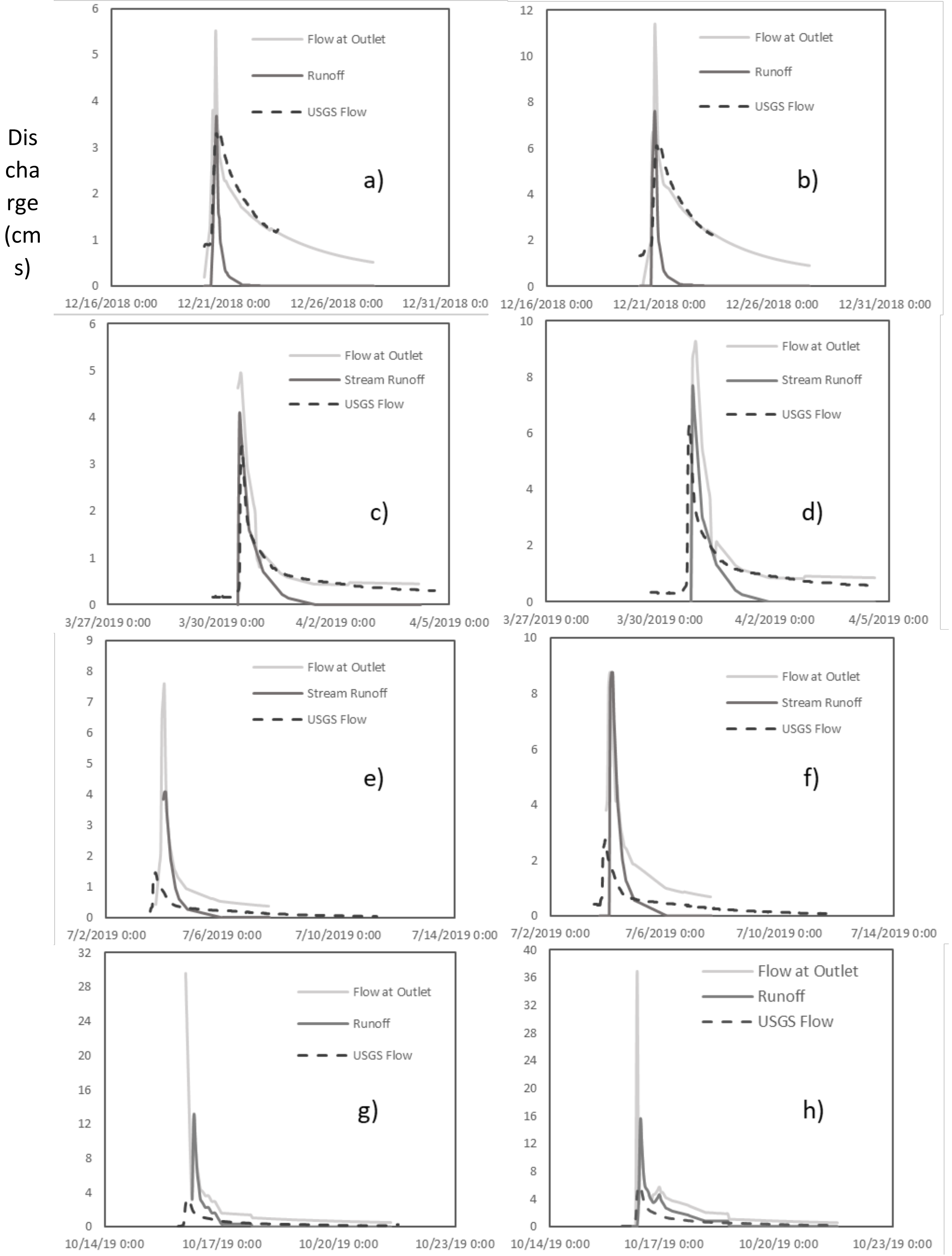

Figure 5.55 Table of Model Prediction R^2 Values

	Flow Total R^2 Value
Dec (2018) Ramsey	0.20
Dec (2018) SE Gage	0.60
April Ramsey	0.79
April SE Gage	0.89
July Ramsey	0.34
July SE Gage	0.82
Oct Ramsey	0.74
Oct SE Gage	0.88

Chapter 6 Discussion

This research hypothesized that the hydrograph and chemograph concept model presented in Husic et al. (2021, in review) will be applicable to karst terrain. The concept model reflects transport of water and nitrate via the multi-porosity of karst aquifers and considers a piston effect when water is pushed out of tertiary porosity conduits at the beginning of events from underground runoff, quickflow from overland runoff, intermediate flow draining from the secondary porosity fracture networks of karst, and slowflow draining from the primary porosity rock matrix of karst. Our results support the hypothesized model as follows. The concept model is supported quantitatively for the Upper South Elkhorn Watershed in the inner bluegrass region of Kentucky using nitrate sensor data and USGS flowrate monitoring, hydrograph separation, and reservoir modelling. The concept model is supported qualitatively through comparison with other karst basin data and hysteresis analyses in Arkansas, Maryland and Virginia. We suggest this concept model might be considered and tested by other researchers working in karst terrain, and the evidence of support for this work justifies such consideration. It is hopeful the concept model here helps with predicting the delivery of nitrate to waterways, so that nitrate can then be better controlled at the source to avert pollution of our water supply. More specific discussion of our results are as follows in the next sub-sections.

6.1 Nitrate and water flowrate data collection and quality assurance quality control

Generally speaking, the nitrate sensor data collected in this thesis is considered high quality. Of all nitrate data collected, only a small percentage was needed to be removed due to poor data quality concerns. The 15-minute nitrate sensor appears to produce high quality data, which is corroborated by other researchers using the SUNA V2 technology. Based on our discussions with water scientists at the Kentucky-Ohio-Indiana USGS Regional office, as well as presentations of those scientists at the KWRRI annual symposium, SUNA V2 sensors collect high quality data and generally require a fairly low amount of maintenance considering the 15 minute resolution data this continuously collected. Comparison with the peer reviewed literature also shows high quality nitrate data from the SUNA V2's. With the earlier model of the SUNA, Burns et al. (2016) carried out similar quality assurance procedures as our study for data collected in the Potomac River and needed to remove ~2% of their nitrate data. Comparison with grab samples analyzed for nitrate reinforced our confidence in the SUNA V2, and Miller et al. (2016) showed similar excellent agreement between SUNA measurements and grab samples measurements.

The GCE (Georgia Costal Ecosystems) Data Toolbox was particularly helpful in streamlining the quality control and assurance procedures. Once flagging parameters were developed, it was easy to learn and implement a procedure to identify questionable data from a large dataset. I would recommend use of this program in the Matlab interface to aid in quality control for any large dataset.

To our knowledge, this thesis is the first time such a multi-year nitrate dataset with 15-minute nitrate sensor resolution was reported for surface streams of the inner bluegrass region of Lexington, Kentucky and adjacent counties. We are hopeful the datasets published in this thesis will be useful to other researchers and watershed managers who are trying to understand nitrate timing in our waterways, so that toxic algae bloom impact on water supply can be averted.

6.2 Meta-analyses of karst hydrographs, nitrate chemographs and hysteresis:

The meta-analysis results provided further evidence that our hypothesized concept model for the hydrograph and nitrate chemograph for karst terrains (Figure 2.2) should be considered by researchers in other karst basins. Results showed that five out of six studies showed a near constant or slightly changing nitrate concentration throughout the initial stages of the hydrograph, which reflects the potential for the piston effect. Five out of six study sites showed at least some pronounced decrease in nitrate concentration during the initial stages of the hydrograph, suggesting dilution by rainfall and a quickflow source. Five out of six studies show a nitrate concentration maximum occurring after the hydrograph peak, followed by the nitrate chemograph recession towards a nitrate minimum.

Taken together, the nitrate chemograph, hydrograph and hysteresis results from the six locations provide some discussion. The nitrate dilution shown by most events has been shown for many basins without karst bedrock, and nitrate dilution due to rainwater is a common chemograph result reported in the literature (e.g., see review in Clare, 2019). A typical nitrate response in watersheds with non-karst geology show two-part hydrographs and two-part nitrate chemographs reflective of runoff and baseflow. For example, a common observation in data is a nitrate chemograph signal that mirrors the water hydrograph signal (Figure 6.2.1). Storm events and increasing water discharge is mirrored by a decrease in nitrate concentration as the nitrate of rainwater dilutes river water. As runoff recedes and baseflow takes over, water discharge decreases while nitrate concentration increases as groundwater nitrate levels in water are often more concentrated due to soil nitrate leaching.

However, watersheds underlain by karst bedrock are shown to contrast this two-part behavior and consistent of more complex behavior of the nitrate chemograph due to the triple porosity of karst aquifers. The occurrence of the piston effect and nitrate recession long after the hydrograph peak are less well discussed in the scientific literature for nitrate chemographs, to our knowledge. These results support nitrate behavior in karst basins to follow a behavior reflecting numerous aquifer porosities (see Figures in Chapter 5.2). The piston effect suggests a tertiary porosity of the karst aquifer can play a role in transporting nitrate because pre-event stored nitrate and water in conduits is forced out of underground conduits, caves, and large fractures early on an event. This pre-event water and nitrate can arrive to the basin outlet prior to or along with quickflow. The nitrate recession prevalence suggests the importance of secondary and primary porosity for the delivery of nitrate after the storm event occurs. Intermediate flow associated with water and nitrate originating from the soil layer drains from the karst basin's fracture network long after the storm event has occurred. Storage in this secondary porosity can keep nitrated elevate above a level associated with slowflow draining the rock matrix and bedrock micropores.

6.3 Mass balance un-mixing modelling to quantify sources of water and nitrate:

The results of the mass balance un-mixing simulations using the nitrate and hydrograph data allow discussion of contributions of nitrate from the different hydrologic sources via the piston effect, quickflow, intermediate flow and slowflow pathways in the context of karst basins.

Nitrate associated with subsurface pathways in the karst bedrock account for the overwhelming majority of nitrate (79% of nitrate, on average, Figure 5.3.6), and specifically the intermediate flow pathway provides most of this nitrate (62% of nitrate, on average, follows the intermediate flow pathway, Figure 5.3.6). The intermediate flow is nitrate stored in the soil column that is transported from the soil to the bedrock to the stream. The majority of the nitrate following the intermediate pathways is noteworthy because this occurs on the falling limb of the hydrograph when based on our view of a hydrograph and its peak, we might expect flow and nitrogen contributions to the river to be somewhat lower.

However, the importance of the intermediate flow to deliver nitrate from soils to the river show corroboration with recent findings and discussions regarding soil nitrate leaching (e.g., Di and Cameron, 2003; Husic et al., 2020). As plant and soil organic matter turnover in the soil column, nitrogen mineralization occurs and can increase in mass in the soil. This biogeochemistry is coupled with evapotranspiration and the lowering of water being held in the soil during non-rain periods. This build-up of nitrate gets flushed out of the soil column during rain events when the soil water storage increases, and soil water percolation occurs. The nitrate concentration of intermediate flow is high relative to rainwater, at times approaching an order of magnitude difference between their nitrate concentrations. Therefore, the soil N leaching and in turn intermediate N pathway produces the highest nitrate loading to the river, even though flow is receding on the falling limb of the hydrograph.

The importance of soil N leaching via the intermediate pathway adds to discussion of the importance of soil N delivery more generally for moderately wet, temperate climates, especially when considering the Ohio River Basin. Recent work showed that the majority of nitrate delivered to the river network of the Ohio River Basin occur during winter months (December to March) and this was attributed to nitrate sourced primarily from soil nitrate leaching (Gerlitz et al., in review). The present study adds to this discussion and shows that at the watershed scale in the ORB, regardless of the season, soil nitrate leaching via intermediate flow is the majority source-pathway combination for the pasture and urban lands considered herein. Further, while storm events and their peaks are initially associated with low nitrate levels, the post-peak period should be considered as the highest concentrated nitrate waters traveling through the river network.

Another noteworthy result is the overall importance of the piston effect to transport previously stored water and nitrate from the karst aquifer at the beginning of an event.

Nitrate from the piston effect accounted for 13% of the nitrate load, on average, and should be considered in future work as an important pathway in system similar to the South Elkhorn.

6.4 Reservoir modelling for nitrate transfer in the karst basins:

The reservoir model successfully formulated and carried out simulation of the basin to represent the nitrate transfer processes for prediction. The reservoir model provided additional insight on the impact of sinkhole concentration on the magnitude of the piston effect as well as provides the volume of water and nitrated stored in the different features of the karst aquifer.

The reservoir modelling approach shows efficacy for capturing the fairly complex event dynamics including the piston effect, quickflow, intermediate flow, and slowflow; and in addition, shows several important features. The modelling method can be calibrated with data from one site, then validated with data from a second site. This shows usefulness of the approach for applications, so long as calibration occurs first. The results of the Green Ampt model used to estimate runoff percentage during calibration was consistent with previous theory and showed the overall expected variation of runoff, as might be expected. This result and its comparison with the literature provides additional confidence in data and modelling methods herein. The temporal soil moisture data from Versailles was shown to be useful for parameterizing both the volume of water in the soil, as expected, and the volume of water stored in the karst aquifer. This result might show usefulness in other karst aquifers in other regions because groundwater residence time is small, so the ratio of the volume of water stored in the soil to the volume of water stored in the karst aquifer remains fairly constant. If you have soil moisture, then you can calibrate your karst hydrology reservoir model. The reservoirs enabled us to track the volume of water stored in the reservoirs, and this was one important added result of the study. The volume of water stored in the fracture network during an event is also an interesting result that might be useful to practitioners.

The prediction ability of the reservoir model approach is noteworthy and requires more discussion. Between the upstream and downstream locations (Ramsey and SE Gage), if the model is calibrated for one location, the other can be predicted. The Ramsey drainage area is half that of the South Elkhorn drainage area, this follows that the model can be used at half and double the drainage area for which it was calibrated. When extrapolating the model for use in larger or smaller catchments, it is important to be aware of the geologic conditions such as the differences in sinkhole concentration. The differences in initial soil moisture conditions for each site must also be considered.

The model is also able to predict between seasons. Model parameters for January give moderately strong results for all seasons. To improve precision of the model between seasons you must consider the change in soil moisture conditions which reflect the state of vegetative cover, frozen ground, and the ability for soil at that time of year to take in water. We were able to capture unique drought conditions in October. The model sheds light on how the reservoirs will respond to drought conditions.

I believe the model can be implemented in other watersheds with similar karst conditions. Initial geologic conditions such as height of bedrock and drainage area will always be different in different watersheds. Karst conditions such as rock matrix porosity, size of fractures, and spacing between fractures will change with the age of karst. As karst ages, the fractures will continue be weathered, expanding their diameter and more fractures will form. Cracks within the bedrock will also expand to increase the porosity. With much older karst, more complex features will form such as caves and additional conduits. With the additions of these new features it will likely be necessary to implement new reservoirs into the model.

The model also sheds light on how the total volume in each reservoir responds to an event. The soil reservoir will often slowly return to pre-event conditions. The fracture network will rise slightly before undergoing a large recession slope where water drains to a fraction of pre event levels. The rock matrix will always be decreasing but the total volume is mostly unchanged. Understanding the volume response in October will help to prepare for water storage in future drought conditions. Volume responses in all seasons will help to understand what may lead to future flood events. The differences in seasonal reservoir changes will help to better understand how sources of nitrate delivery change in each season. Finally, timing of reservoir volume changes will help to understand when to predict the timing of highest nitrate concentration coming from the fracture network reservoir.

Figure 6.1 Nitrate response to discharge in watersheds with two-part chemographs consisting of runoff and baseflow. Nitrate is shown to mirror the water discharge because rainfall dilutes the nitrate concentration of river water. (a) Results from Baker and Showers (2019) in North Carolina, USA and (b) results from Sackman (2011) in Washington, USA.

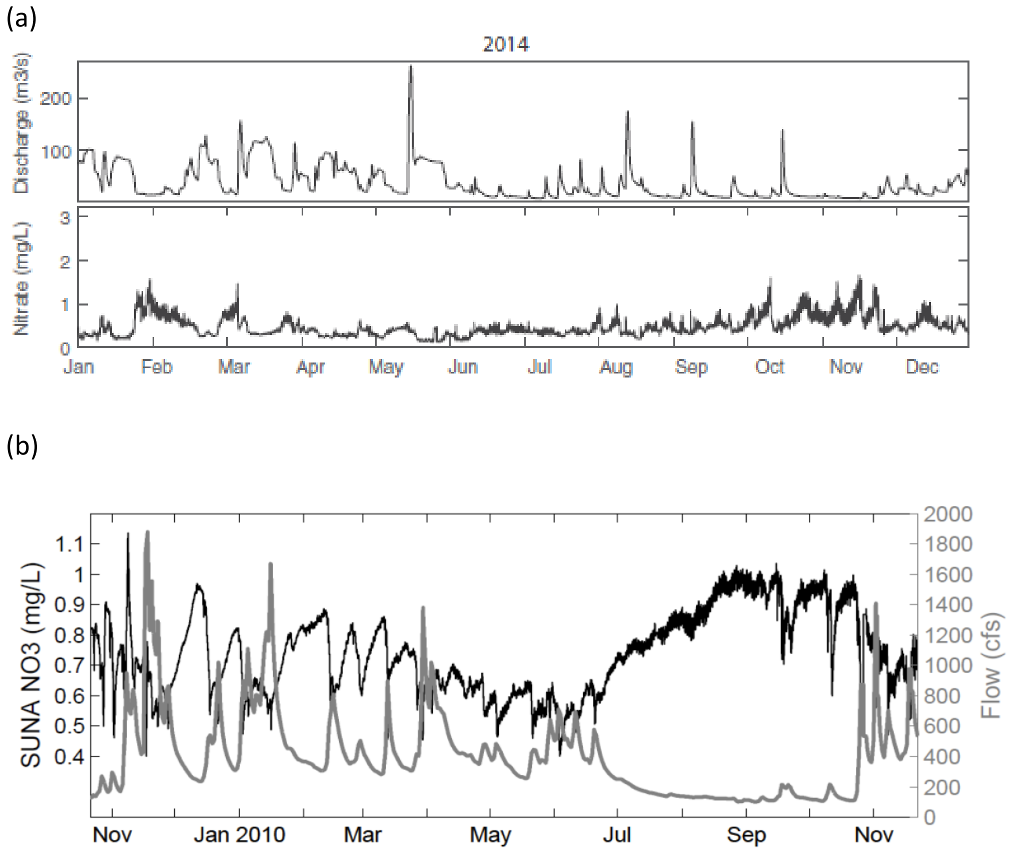

Chapter 7 Conclusion

The conclusions of this thesis are as detailed in the following four points.

1. The high-resolution water quality sensors Seabird SUNA V2 and YSI exo3 have been used to develop multi-year spatial and temporal mapping of the South Elkhorn watershed. Implemented quality control and quality procedures, as well as collaboration with other users of this technology help reassure the strength of these devices in providing consistent and accurate data. In the case that data does need to be corrected or a hardware/software malfunction occurs, this paper details procedures which can be used to mediate these problems.

2. Study of literature has helped us to claim that elements of the concept model developed for Lexington, Kentucky are applicable in similar karst watersheds. A majority reference studies show evidence for the piston effect, nitrogen dilution by quickflow, nitrate concentration maximum from intermediate flow followed by a nitrate recession slope. While the dilution effect is a common nitrate response in watersheds, the piston effect and extended nitrate recession are less well developed in the scientific literature.

3. Mass-balance and un-mixing simulations have been carried out at the upstream Ramsey and downstream SE Gage site in the South Elkhorn watershed. This process revealed an outstanding contribution of nitrate mass from the intermediate flow/ fracture network pathway. This is due in part by our assumption that the intermediate flow path carries the highest contribution of nitrate as reflected by the nitrate peak. This reinforces

recent findings on soil nitrate leaching, the process of organic matter decomposition in soil column which is flushed into the fracture network. This process also revealed the important of the piston effect in transporting water and nitrate stored in the karst conduit during at the start of an event.

4. A reservoir model was developed to recreate the transport processes of storm event rainwater as it runs off towards the stream, pushes out stored conduit water in the piston effect, or recharges the soil reservoir to funnel down to the fracture network and rock matrix. This model was calibrated to yield strong results of flow and nitrogen concentrations for every event at both sites. Once calibrated for an event the model can be used to predict responses for sites at 0.5 to 2 times the drainage area. The model helped pinpoint seasonal differences in response caused by pre-event soil moisture and vegetation conditions. The concepts of this model can be used in similar karst watersheds once differences in the karst geology are accounted for. The model also sheds light on concepts on event response in total volumes of the soil, fracture network, and rock matrix reservoirs.

Appendix

A.1 SUNA Calibration Steps from SUNA v2 User Manual

Update reference spectrum

The user needs to update the reference spectrum of the SUNA at regular intervals so that the data that the sensor collects is accurate. It may also be necessary to update the firmware, although that is not required very frequently.

A calibration file contains the data required to convert a spectral measurement into a nitrate concentration. The calibration data are the wavelengths of the spectrum, the extinction coefficients of chemical species and a reference spectrum relative to which the measurement is interpreted. The sensor can store many calibration files, but only the active file has a green background. Push Transfer Files > File Manager, then select the Calibration Files tab to see the list of calibration files stored in the sensor.

Make sure to clean the sensor and the sensor windows at regular intervals and before and after every deployment. Monitor the spectral intensity of the lamp. Although the intensity will decrease over time, make sure there are no sudden changes.

Necessary supplies:

- Power supply
- PC with software
- Connector cable for sensor–PC–power supply
- Clean de-ionized (DI) water
- Lint-free tissues
- Cotton swabs
- Isopropyl alcohol (IPA)
- Parafilm® wrap Notes
- Use only lint-free tissues, OPTO-WIPES™, or cotton swabs to clean the optical windows.
- Use the software to update the reference spectrum.
- Use only clean DI water that has been stored in clean glassware.
- Use Parafilm® wrap to capture DI water in the optical area of the sensor. Do not use cups, a bucket, or a tank to collect a reference sample.

1. Clean the sensor:

a. Flush the sensor and the optical area with clean water to remove debris and saltwater.

b. Clean the metal parts external to the optical area so that the Parafilm® will seal.

c. Std. SUNA only: If the sensor is equipped with a wiper, carefully move it away from the optical area.

2. Cut and stretch a length of approximately 40 cm (16 in.) of Parafilm®.

3. Wind several layers of the Parafilm® around the metal near the optical area.

4. Break a small hole in the top of the Parafilm® and fill the optical area with DI water.

5. Supply power to the sensor and start the software if necessary.

6. Make sure that the sensor operates in Continuous mode: push Settings, then in the

General tab, select "Continuous" for the "Operational Mode."

7. Push Start. Push Start Logging to File to save approximately one minute of data to the PC.

8. Push Stop.and the sensor stops data collection.

9. Open the data file on the PC and calculate the average measurement value. This is a "dirty" measurement to record the value when there are biofouling and blockages in the optical area.

10. Remove the Parafilm® and drain the water from the optical area.

11. Clean the optical area:

a. Use DI water or IPA and cotton swabs and lint-free tissues to clean the windows.

b. Use vinegar to clean debris such as barnacles. Be careful that the windows do not get scratches.

12. Flush the optical area with DI water to remove any remaining IPA or vinegar.

13. Wind Parafilm® around the metal near the optical area.

14. Break a small hole in the top of the Parafilm® and fill the optical area with fresh DI water.

15. Supply power to the sensor and start the software if necessary.

16. Push Reference Update.

The "Reference Update Wizard" shows.

17. Fill the sample volume with distilled water. Refer to the hardware user manual for details.

18. Make sure the "Operational Mode" is set to "Continuous," then push Next.

19. The sensor starts to collect data. This will take approximately 30 seconds.
20. Push Next.
21. Look at the graph to see the change between reference spectra.
22. Push Next.
23. Push Browse to select a directory in which to save the Calibration Report.
24. Optional: write a comment.
25. Put a check in the "View" box to automatically open the new report.
26. Put a check in the "View" box to automatically open the new calibration file.
27. Push Finish.

The software makes a report and a calibration file.

5.4 Compare reference spectrum files

Compare the change between two reference spectrum files. The amount of change is related to the time interval between the updates and the amount of lamp use during that time.

Note that this procedure is done automatically by the software when the user updates the reference spectrum for the sensor. Refer to Update reference for more information.

1. From the Data menu, select SUNA, then Compare Calibration.
2. Push Browse to find the first calibration, or reference file, to compare.
3. Push Browse to find the second file to compare. Note that the files must be from the same sensor.
4. Push Compare.

A typical update interval of 3–6 months with no more than 100 hours of lamp use should cause a change of no more than 10% in the 215–240 nm interval.

Below 215 nm, larger relative changes are normal.

Above 240 nm, the change is smaller than at the 215–240 nm range.

If there is a large change, do several reference updates 12–24 hours apart to monitor the stability of the reference spectrum.

A.2 EXO 3 Sensor Calibration Steps from the EXO User Manual

Calibration set-up

For accurate results, thoroughly rinse the EXO calibration cup with water, and then rinse with a small amount of the calibration standard for the sensor you are going to calibrate. Two to three rinses are recommended. Discard the rinse standard, then

refill the calibration cup with fresh calibration standard. Fill the cup to approximately the first line with a full sensor payload or the second line with small sensor payload. Recommended volumes will vary, just make certain that the sensor is submerged. Be careful to avoid cross-contamination with other standards.

Begin with clean, dry probes installed on the EXO sonde. Install the clean calibration guard over the probe(s), and then immerse the probe(s) in the standard and tighten the calibration cup onto the EXO sonde. We recommend using one sonde guard for calibration procedures only, and another sonde guard for field deployments. This ensures a greater degree of cleanliness and accuracy for the calibration procedure.

Conductivity Calibration

Clean the conductivity cell with the supplied soft brush before calibrating (see Section 5.7).

This procedure calibrates conductivity, non-linear function (nLF) conductivity, specific conductance, salinity, and total dissolved solids

A variety of standards are available based on the salinity of your environment. Select the appropriate calibration standard for your deployment environment; we recommend using standards greater than 1 mS/cm (1000 µS/cm) for greatest stability.

Pour conductivity standard into a clean and dry or pre-rinsed EXO calibration cup. YSI recommends filling the calibration cup up to the second marked line to ensure the standard is above the vent holes on the conductivity sensor. Immerse the probe end of the sonde into the solution, gently rotate and/or move the sonde up and down to remove any bubbles from the conductivity cell.

Allow at least one minute for temperature equilibration before proceeding.

In the Calibrate menu, select the Conductivity sensor and then select the parameter you wish to calibrate. These parameters may include conductivity, nLF conductivity, specific conductance, or salinity. Calibrating any one option automatically calibrates the other parameters. After selecting the option of choice (specific conductance is normally recommended), enter the value of the standard used during calibration. Be certain that the units are correct (microsiemens, not millisiemens).

Observe the Pre Calibration Value readings and the Data Stability, and when they are Stable, click Apply to accept this calibration point.

NOTE: If the data do not stabilize after 40 seconds, gently rotate the sonde or remove/reinstall the cal cup to make sure there are no air bubbles in the conductivity cell.

Click Complete. View the Calibration Summary screen and QC Score. Click Exit to return to the sensor calibration menu. Rinse the sonde and sensor(s) in tap or purified water and dry.

Dissolved Oxygen Calibration

ODO % sat and ODO % local – 1-point

Place the sonde with sensor into either water-saturated air or air-saturated water:

Water-saturated air: Ensure there are no water droplets on the DO sensor or the thermistor. Place into a calibration cup containing about 1/8 inch of water that is vented by loosening the threads. (Do not seal the cup to the sonde.) Wait 10-15 minutes before proceeding to allow the temperature and oxygen pressure to equilibrate. Keep out of direct sunlight.

Air-saturated water: Place into a container of water which has been continuously sparged with an aquarium pump and air stone for one hour. Wait approximately 5 minutes before proceeding to allow the temperature and oxygen pressure to equilibrate.

In the Calibrate menu, select ODO, then select ODO % sat or ODO % local. Calibrating in ODO % sat automatically calibrates ODO mg/L and ODO % local and vice versa.

Enter the current barometric pressure in mm of Hg (Inches of Hg x 25.4 = mm Hg).

NOTE: Laboratory barometer readings are usually “true” (uncorrected) values of air pressure and can be used “as is” for oxygen calibration. Weather service readings are usually not “true”, i.e., they are corrected to sea level, and therefore cannot be used until they are “uncorrected”. An approximate formula for this “uncorrection” (where the BP readings MUST be in mm Hg) is: True BP = [Corrected BP] – [2.5 * (Local Altitude in ft above sea level/100)]

Observe the Pre Calibration Value readings and the Data Stability, and when they are Stable, click Apply to accept this calibration point.

Click Complete. View the Calibration Summary screen and QC Score. Click Exit to return to the sensor calibration menu.

mg/L – 1-point

Place the sonde with sensor in a container which contains a known concentration of dissolved oxygen in mg/L and that is within

±10% of air saturation as determined by one of the following methods:

Winkler titration

Aerating the solution and assuming that it is saturated

Measurement with another instrument

NOTE: Carrying out DO mg/L calibrations at values outside the range of ±10 % of air saturation is likely to compromise the accuracy specification of the EXO sensor. For highest accuracy, calibrate in % saturation.

In the Calibrate menu, select ODO, then select ODO mg/L. Calibrating in ODO mg/L automatically calibrates ODO % sat and vice versa.

Enter the known mg/L concentration for the standard value. Observe the Pre Calibration Value readings and the Data Stability, and when they are Stable, click Apply to accept this calibration point. Click Complete.

Rinse the sonde and sensor(s) in tap or purified water and dry.

pH Calibration

2-point

Select the 2-point option to calibrate the pH probe using two calibration standards. In this procedure, the pH sensor is calibrated with a pH 7 buffer and a pH 10 or pH 4 buffer depending upon your environmental water. A 2-point calibration can save time (versus a 3-point calibration) if the pH of the media to be monitored is known to be either basic or acidic.

Pour the correct amount of pH buffer in a clean and dry or pre-rinsed calibration cup. Carefully immerse the probe end of the sonde into the solution, making sure the sensor's glass bulb is in solution by at least 1 cm. Allow at least 1 minute for temperature equilibration before proceeding.

In the Calibrate menu, select pH or pH/ORP, then select Calibrate.

NOTE: Observe the temperature reading. The actual pH value of all buffers varies with temperature. Enter the correct value from the bottle label for your calibration temperature for maximum accuracy. For example, the pH of one manufacturer's pH 7 Buffer is

7.00 at 25˚C, but 7.02 at 20˚C.

If no temperature sensor is installed, user can manually update temperature by entering a value.

Observe the Pre Calibration Value readings and the Data Stability, and when they are Stable, click Apply to accept this calibration point. Click Add Another Cal Point in the software.

Rinse the sensor in deionized water. Pour the correct amount of the next pH buffer standard into a clean, dry or pre-rinsed calibration cup, and carefully immerse the probe end of the sonde into the solution. Allow at least 1 minute for temperature equilibration before proceeding.

Repeat the calibration procedure and click Apply when the data are stable. Rinse the sensor and pour the next pH buffer, if necessary. Repeat calibration procedure for the third point and click Apply when data are stable.

Click Complete. View the Calibration Summary screen and QC Score. Click Exit to return to the sensor calibration menu. Rinse the sonde and sensors in tap or purified water and dry.

Turbidity Calibration

Tools and Practices

Standards should be selected based upon the range in which one is expected to work. For low-turbidity waters, one might use 0 and 12.4 for a two-point calibration. If turbidities might exceed the lower ranges 0 and 124 should be used for a two-point calibration (not 0 and 1010 for reasons described below), and 0, 124 and 1010 for a three-point calibration. There is not a calibration standard beyond 1010 FNU at this time.

The FNU of each bottle can change with production batches, and as such the label of the bottle should always be checked for the FNU that should be entered into the software or handheld during calibration.

In some cases it may be acceptable to use deionized or distilled water rather than YSI's 0 FNU standard. Beware, however, that distilled water from some sources has been shown to not be 0 FNU. Calibration with a non-zero standard can cause negative readings when the sensor is used in waters that actually are clear. Non-zero readings also can occur if the calibration equipment (e.g. sonde guard, calibration cup) is not sufficiently clean.

Some users will have a preference, if not a requirement, for use of formazin standards. Examples may be formazin prepared according to Standard Methods for the Treatment of Water and Wastewater (Section 2130 B), or Hach StablCal™ of various NTUs. These standards are acceptable for a two-point calibration. However, users who anticipate working in higher turbidities and who choose to use a formazin standard for the third point may see yellow SmartQC Scores during that calibration. The sensor can still be used, but since the algorithms for calibration were developed with YSI's polymer beads there may be less perfect alignment of the gain factors when using formazin.

Note also that if doing a three-point calibration, one should not use formazin for the second point, and polymer for the third point. Rather, one should only use the polymer for all points of a three point calibration (or water for 0 FNU and polymer for the second and third points), or formazin for all three points.

In all cases, due to the non-linear response of turbidity sensors and YSI's proprietary algorithms for post-processing of the data, the points of a two or three point calibration must be within the limits outlined here:

First Point	> 0 and ≤1 FNU
Second Point	>5 and ≤200 FNU
Third Point	>400 and ≤4200 FNU

The second calibration point, whether one is using formazin or YSI's polymer, should not be out of the 5-200 FNU range. If one tries to use a standard that is in the 400-4200 FNU range for the second calibration point, accuracy cannot be assured and often a yellow QC Score will result.

Performing a 2-point calibration

Pour the 0 FNU standard (or deionized or distilled water) into the clean calibration cup and immerse the probe end of the sonde into the standard. The sonde should have the sonde guard on, and if one will deploy with the copper antifouling guard that is likewise the guard that should be used during calibration. Pay careful attention while submersing the sensors to not trap bubbles on the face of the turbidity sensor(s).

In either KorEXO Software or the handheld's Calibration menu, select Turbidity to calibrate.

Enter 0.0 (or some offset value between 0.0 and 1.0) as the first calibration value. While the sensor is still stabilizing one may wipe the sensors (using the button in the software or menu option on the handheld) to remove any bubbles. When the data are Stable, select the option to "Apply calibration" for this point.

It is advised at this point that the sensors, sonde guard, and calibration cup be rinsed with a small amount of the standard that will be used for the second calibration point. Discard this rinse, and then fill the cup with the second calibration standard. Click Add Another Cal Point in the software.

Place the sensors into the second calibration standard, and follow the same steps to wipe and obtain a stable reading. Use the value on the label of the YSI standard bottle for the FNU of the second calibration point.

When the data are Stable, select the option to "Apply calibration" for this point. Select the option to complete the calibration and observe the SmartQC Score in the calibration worksheet. In KorEXO Software, color indicators will also make the QC Score apparent.

Rinse the sonde with water and discard all used turbidity standards.

References

Al Aamery, N., Adams, E., Fox, J., Husic, A., Zhu, J., Gerlitz, M., . . . Bettel, L. (2021). Numerical model development for investigating hydrologic pathways in shallow fluviokarst. *Journal of Hydrology, 593*, 125844. doi:10.1016/j.jhydrol.2020.125844

CDC. (2017, December 14). Harmfull Algae Bloom Associated Illness - Freshwater Environments. Retrieved April 13, 2021, from https://www.cdc.gov/habs/illness-symptoms-freshwater.html

Claire, E. C. (2019). *Decomposing a Watershed's Nitrate Signal Using Spatial Sampling and Continuous Sensor Data* (Unpublished master's thesis). University of Kentucky.

Clean Water Action. (2019, July 12). Harmful algal outbreaks and drinking water. Retrieved April 13, 2021, from https://www.cleanwateraction.org/features/harmful-algal-outbreaks-and-drinking-water

Cross, A. (2019, September 30). University of Kentucky Health News - Algal Bloom Warning Issued For Ohio River Above Louisville. Retrieved April 13, 2021, from https://ci.uky.edu/kentuckyhealthnews/2019/09/30/algal-bloom-warning-issued-for-ohio-river-above-louisville/

Currens, J. C. (1998). Mapped Karst Ground-Water Basins in the Beaver Dam 30 x 60 Minute Quadrangle. *Geology Commons*. doi:10.3133/i1512

Denchak, M., & Sturm, M. (2020, September 24). NRDC - Freshwater Harmful Algal Blooms. Retrieved April 13, 2021, from https://www.nrdc.org/stories/freshwater-harmful-algal-blooms-101#preventing

Di HJ, Cameron KC (2002) Nitrate leaching in temperate agroecosystems: Sources, factors and mitigating strategies. Nutr Cycl Agroecosystems 64:237–256. doi: 10.1023/A:1021471531188

EPA. (2019, December 19). Nutrient Pollution - Harmful Algal Blooms. Retrieved April 13, 2021, from https://www.epa.gov/nutrientpollution/harmful-algal-blooms#cause

Fournier, M., Massei, N., Bakalowicz, M., Dussart-Baptista, L., Rodet, J., & Dupont, J. P. (2006). Using turbidity dynamics and geochemical variability as a tool for understanding the behavior and vulnerability of a karst aquifer. *Hydrogeology Journal, 15*(4), 689-704. doi:10.1007/s10040-006-0116-2

Heber Green, W., & Ampt, G. A. (1911). Studies on Soil Phyics. *The Journal of Agricultural Science*, *4*(1), 1–24. https://doi.org/10.1017/s0021859600001441

H20 Engineering. (2021, April 06). UV Spectroscopy Technology. Retrieved April 29, 2021, from https://h2o-engineering.com/uv-spectroscopy-technology/

Hartmann, A., Goldscheider, N., Wagener, T., Lange, J., & Weiler, M. (2014). Karst water resources in a changing world: Review of hydrological modeling approaches. *Reviews of Geophysics, 52*(3), 218-242. doi:10.1002/2013rg000443

Husic, A., Fox, J., Adams, E., Ford, W., Agouridis, C., Currens, J., & Backus, J. (2019). Nitrate pathways, processes, and timing in an Agricultural Karst System: Development and application of a numerical model. *Water Resources Research, 55*(3), 2079-2103. doi:10.1029/2018wr023703

Jarvie, H. P., Sharpley, A. N., Kresse, T., Hays, P. D., Williams, R. J., King, S. M., & Berry, L. G. (2018). Coupling high-frequency stream metabolism and nutrient monitoring to explore biogeochemical controls on downstream nitrate delivery. *Environmental Science & Technology, 52*(23), 13708-13717. doi:10.1021/acs.est.8b03074

Kentucky Geological Survey, UKY. (2021). Where Is Karst Located In Kentucky? Retrieved May 10, 2021, from https://www.uky.edu/KGS/karst/karst_location.php

MacQuown, William C. Jr.; Barr, Jimmie L.; Hine, George T.; Sumartojo, Jojok; Peck, Edward V.; and Thomas, Franklin D., "FactorsControlling Porosity and Permeability in the Curdsville Member of the Lexington Limestone" (1967).KWRRI Research Reports. 186.https://uknowledge.uky.edu/kwrri_reports/186

Mahoney, D. T., Fox, J. F., & Al Aamery, N. (2018). Watershed erosion modeling using the probability of sediment connectivity in a gently rolling system. *Journal of Hydrology, 561*, 862-883. doi:10.1016/j.jhydrol.2018.04.034

McCuen, R. H. (2017). *Hydrologic analysis and design* (Fourth ed.). Upper Saddle River, NJ: Pearson Education.

Morgan Gerlitz, Jimmy Fox, William Ford, Admin Husic, Tyler Mahoney, Mindy Armstead, Susan Hendricks, Angela Crain, Jason Backus, Erik Pollock, Wei Ren, Bo Tao, Brenden Riddle, David White. 2021. Nitrate sensor results suggest soil-plant processes produce three distinct seasonal patterns of nitrate concentrations in the Ohio River Basin. Environmental Science and Technology, in review.

Miller, M. P., Tesoriero, A. J., Capel, P. D., Pellerin, B. A., Hyer, K. E., & Burns, D. A. (2016). Quantifying watershed-scale groundwater loading and in-stream fate of nitrate using high-frequency water quality data. *Water Resources Research, 52*(1), 330-347. doi:10.1002/2015wr017753

NOAA. (2019). Index of public data U.S. climate reference network. Retrieved April 14, 2021, from https://www1.ncdc.noaa.gov/pub/data/uscrn/products/

NOAA. (2019). National centers for environmental information. Retrieved April 14, 2021, from https://www.ncdc.noaa.gov/

Pellerin, B. A., Stauffer, B. A., Young, D. A., Sullivan, D. J., Bricker, S. B., Walbridge, M. R., . . . Shaw, D. M. (2016). Emerging tools for continuous nutrient monitoring networks: Sensors advancing science and water resources protection. *JAWRA Journal of the American Water Resources Association, 52*(4), 993-1008. doi:10.1111/1752-1688.12386

Pfaff, J. D. (1993, August). *Method 300.0 Determination Of Inorganic Anions By Ion Chromatography* [PDF]. Cincinatti, Ohio: U.S. Environmental Protection Agency.

Pinault, J., Plagnes, V., Aquilina, L., & Bakalowicz, M. (2001). Inverse modeling of the hydrological and the hydrochemical behavior of hydrosystems: Characterization of karst system functioning. *Water Resources Research, 37*(8), 2191-2204. doi:10.1029/2001wr900018

Satlantic Incorporated, 2011, SUNA user manual, SUNACom 2.2.0, Document SAT-DN-00498, accessed
April 20201 at https://www.whoi.edu/fileserver.do?id=199144&pt=2&p=207009

Terrio, P.J., Straub, T.D., Domanski, M.M., and Siudyla, N.A., 2015, Continuous monitoring of sediment and nutrients in the Illinois River at Florence, Illinois, 2012–13: U.S. Geological Survey Scientific Investigations Report 2015–5040, 61 p., http://dx.doi.org/10.3133/sir20155040.

USGS. StreamStats. Retrieved April 14, 2021, from https://streamstats.usgs.gov/ss/

USGS. Topographic Maps of the US. Retrieved April 14, 2021, from https://apps.nationalmap.gov/

White WB (2002) Karst hydrology: Recent developments and open questions. Eng Geol 65:85105. doi: 10.1016/S0013-7952(01)00116-8

Worthington, S. R., & Gunn, J. (2009). Hydrogeology of carbonate aquifers: A short history.*Ground Water, 47*(3), 462-467. doi:10.1111/j.1745-6584.2008.00548.x

VITA

John Robert Pike, B. S. C. E.

Lexington, KY

EDUCATION

Bachelor of Science in Civil Engineering	University of Kentucky
Cumulative GPA: 3.4	Graduation: December, 2019

EXPERIENCE

UK Water Quality Research	August 2019 - May 2021
KTC Structures CatStrong Bridge Repair, Lexington, KY	March-August 2018
EWB International Building Design and Construction, Malawi, Africa	August 2018

ACTIVITIES

Engineers Without Borders, President	2018

AWARDS and RECOGNITIONS

1. Recipient of the Lauderdale Fellowship (2019-2021)
2. Recipient of GSP Presidential Scholarship (2016-2019)
3. Recipient of Downey Scholarship (2018-2019)
4. Recipient of Deatrick Scholarships (2019-2020)